

國 立 中 央 大 學

資 訊 工 程 學 系
博 士 論 文

創新色彩空間的研究與應用

The Researches and Applications on
Innovative Color Spaces

研 究 生：錢均亮

指 導 教 授：曾 定 章 教 授

中 華 民 國 一 ○ ○ 年 六 月



國立中央大學圖書館 碩博士論文電子檔授權書

(98年4月最新修正版)

本授權書所授權之論文全文電子檔(不包含紙本、詳備註1說明)，為本人於國立中央大學，撰寫之碩/博士學位論文。(以下請擇一勾選)

- ()同意 (立即開放)
- ()同意 (一年後開放)，原因是：_____
- ()同意 (二年後開放)，原因是：_____
- ()同意 (三年後開放)，原因是：_____
- ()不同意，原因是：_____

以非專屬、無償授權國立中央大學圖書館與國家圖書館，基於推動「資源共享、互惠合作」之理念，於回饋社會與學術研究之目的，得不限地域、時間與次數，以紙本、微縮、光碟及其它各種方法將上列論文收錄、重製、公開陳列、與發行，或再授權他人以各種方法重製與利用，並得將數位化之上列論文與論文電子檔以上載網路方式，提供讀者基於個人非營利性質之線上檢索、閱覽、下載或列印。

研究生簽名: 錢均亮 學號: 93542014

論文名稱: 創新色彩空間的研究與應用

指導教授姓名: 曾定章教授

系所 : 資訊工程學系 所 博士班 碩士班

日期: 民國 100 年 06 月 20 日

備註:

-
1. 本授權書之授權範圍僅限電子檔，紙本論文部分依著作權法第 15 條第 3 款之規定，採推定原則即預設同意圖書館得公開上架閱覽，如您有申請專利或投稿等考量，不同意紙本上架陳列，須另行加填聲明書，詳細說明與紙本聲明書請至 <http://thesis.lib.ncu.edu.tw/> 下載。
 2. 本授權書請填寫並親筆簽名後，裝訂於各紙本論文封面後之次頁（全文電子檔內之授權書簽名，可用電腦打字代替）。
 3. 請加印一份單張之授權書，填寫並親筆簽名後，於辦理離校時交圖書館（以統一代轉寄給國家圖書館）。
 4. 讀者基於個人非營利性質之線上檢索、閱覽、下載或列印上列論文，應依著作權法相關規定辦理。

論文名稱：創新色彩空間的研究與應用

中文摘要

在高品質的彩色影像強化中，強化亮度或飽和度的同時，保持色調不變是很重要的，因此符合感官的色彩模型，像是 HSI , HSL 以及 HSV 等等，常被拿來使用。 HSI 是一個常用的色彩模型，有許多色彩的應用都是以這個模型為基礎，無論如何，在 HSI 色彩空間修改亮度與飽和度之後，再從 HSI 色彩模型轉換回到 RGB 色彩模型時，常常造成跑出色域 (out-of-gamut) 的問題，除此之外，不論色域中最大的飽和度範圍為何，像素的飽和度總是根據亮度的增加而遞增，亮度的減少或遞減。

HSV (Hue-Saturation-Value) 色彩模型在彩色影像強化與影像分割很常用到，但是在 HSV 色彩空間，同一亮度值所組成的平面，是平行於 RGB 方塊屋頂，環繞白色的三個平面，該平面的面積會隨著亮度值的遞增而擴增，因此影像的亮度直方統計圖會偏向集中在高亮度值的區域，因為亮度越高統計面積越大，這樣會導致色調和亮度很接近但是飽和度有明顯差異的兩個像素，在亮度強化之後，像是 histogram equalization 或是 histogram stretching，會被大大的分開。

在這篇論文，我提出了一個從 RGB 到 HSI 色彩轉換的修正公式，稱為 $eHSI$ 色彩模型，用來解決彩色影像強化中 out-of-gamut 的問題，並且讓像素的飽和度，可以根據最大飽和度的範圍自動適應性的調整，也就是像素的飽和度可以根據最大可擴充的範圍，自動增強或減少。在實驗部分，我還示範了基於所提出的 $eHSI$ 色彩模型，如何犧牲一些對比度來增強影像的飽和度，另一方面，我也提出了一個改進的 HSV 色彩模型： $iHSV$ ，它保留了一般在 RGB 色彩空間，亮度直方統計圖有高斯分布的特性，那是因為在 RGB 色彩空間的兩端有較小的飽和度延伸範圍，在中央有較大的飽和度延伸範圍，我也再度示範了如何犧牲一些對比度來增進影像的飽和度，實際上，我們可以根據影像的特性，在亮度和飽和度的強化之間做一些取捨，來獲得一個最佳品質的影像。

最後在遙測影像裡，雲層遮蔽是一個嚴重的問題，這個問題大部分可以用不同時段的影像中，沒有雲區域的拼貼來消除，在這篇論文，我們提出一個多重技巧的方法，藉由不同時段衛星影像的拼貼，在三個步驟內拼貼出無雲的衛星影像。首先，原始影像用我們提出的 *eHSI* 色彩模型來強化，其次，一個簡單的亮度閾值，加上幾個不同的比較方法，可以用來擷取出所有雲層覆蓋的區域，然後我們選擇較少雲層覆蓋的影像當作基底影像，並且將其分割成許多方格區域，我們利用偵測到有雲方格區域周邊八個相鄰的方格區域，來涵蓋破碎雲以及由太陽斜照所形成雲的陰影，最後，這些厚雲以及雲的陰影存在的區域，會被另一時段影像相同位置且無雲的區域所替換，然後我們用一個金字塔型的多重解析度融合方法來產生一張無雲的衛星影像。基於我們所提出的完整解決方案，融合後的影像除了可以還原雲層覆蓋的部分，還可以有較佳的亮度和飽和度。

Abstract

While enhancing the intensity or saturation component for high-quality color image enhancement, keeping the hue component unchanged is important; thus, perceptual color models such as *HSI*, *HSL*, and *HSV* were used. Hue-Saturation-Intensity (*HSI*) is a public color model, many color applications are commonly based on this model; however, the transformation from *HSI* model to *RGB* model usually generates the out-of-gamut problem after modifying intensity and saturation in the *HSI* model. Moreover, the saturation component is always increased or decreased following the change of intensity component no matter what the attainable saturation range is.

The *HSV* (Hue-Saturation-Value) color model is popular for color image enhancement and segmentation; but the identical-value plane of the *HSV* color space is parallel to one of the three ceiling planes of the *RGB* cube, the area of the plane will be extended as the value is increased. Hence the value histogram is concentrated in the high value portion; the low saturation pixels are highly separated from the high saturation ones after enhancement on the value components, such as histogram equalization and histogram stretching, although their hue and intensity are approximate.

In this paper, we propose accurate formulas for the color transformation between *RGB* and the proposed *HSI* color model, called the exact *HSI* (*eHSI*) color model, to resolve the out-of-gamut problem directly as well as to automatically adapt the saturation range; that is, the saturation component can be enhanced or reduced according to the attainable maximum saturation range. In experiments, we demonstrate how to sacrifice a little contrast to improve the image saturation based on the proposed *eHSI* color model. On the other hand, we propose an improved *HSV* color model *iHSV*, which preserves the Gaussian distribution characteristic of the intensity histogram in *RGB* cube; that is, the

maximum saturation range is smaller on both ends and larger in the central area of the value axis in the corresponding *HSV* model. We also demonstrate how the saturation of an image can be improved by sacrificing a little contrast in the improved *HSV* color model. In practice, we can take a counterbalance between intensity enhancement and saturation enhancement to obtain a better quality image based on the characteristics of images.

Furthermore, partial cloud cover is a serious problem in optical remote sensing images. The problem can be mostly resolved by mosaicking the cloud-free areas of multi-temporal images. We propose multidisciplinary methods to generate cloud-free mosaic images from multi-temporal satellite images in three steps. At first, all original images are enhanced in intensity based on the proposed exact *HSI* (*eHSI*) color model. Secondly, an intensity thresholding accompanied with a difference comparison method is used to extract all cloud-cover regions. Then we choose the image with the least thin cloud cover as the base image and divide the image into grid zones. We find the thin-cloud and cloud-shadow zones in the eight neighbors of the thick cloud zones based on the relative locations and elevation angle of the sun. Finally, the cloud and cloud-shadow zones of the base image are replaced by the same-location cloud-free zones on other temporal images; then a pyramid multi-scale fusion method is used to generate cloud-free satellite images. Based on the proposed complete approach, fused images with proper brightness and saturation are produced from source images that may have variant brightness.

誌謝

七年是一段不算短的時間，我終於畢業了！儘管取得博士學位所獲得的回報，並不如當初所想像的，但是這段歷程是值得回味的。

在這段期間，有許多人伸出溫暖的雙手幫助我，也有一些人無情的阻擾我，我都要對他們表達感謝之意，因為他們，讓我得以學習與成長。

我要感謝我的指導教授曾定章教授，讓我學會獨立思考與研究的能力。

我還要感謝我的母親與妻子，在我艱困與迷惘的時候，無條件的給予我支持與鼓勵。

還有我的兩個可愛的寶貝女兒，雖然妳們的出生，讓我倍加艱辛，但是也是驅策我勇往直前的動力來源，只要能看到妳們可愛的笑容，一切辛苦都是那麼的值得。

最後，我要感謝我的父親，在我們幼小家境貧困時，您總是不辭辛勞的給予我們最好的生活環境，但是在您人生的最後幾年，遭受癌症病魔折磨的同時，我由於忙著學業與工作，而未能給予您最好的照顧與治療，以至於讓您痛苦的離開，我至今仍感到遺憾且難以釋懷！

謹以此論文獻給我敬愛的父親，希望您在天之靈，能夠以我為榮，也能夠因此得到安慰。

Contents

中文摘要	i
Abstract	iii
誌謝	v
Contents	vi
List of Figures	viii
List of Tables	xii
Chapter 1 Introduction	1
1.1 Motivation	1
1.2 Related work.....	2
1.3 The perceptive color model.....	5
1.4 Color image enhancement	8
1.5 Cloud removal in satellite images	11
1.6 The dissertation organization	14
Chapter 2 The Exact <i>HSI</i> Perceptive Color Model	15
2.1 The color patch analysis of traditional <i>HSI</i> color model.....	16
2.2 <i>RGB</i> to <i>eHSI</i> transformation	19
2.3 <i>eHSI</i> to <i>RGB</i> transformation	24
2.4 The influence of intensity on saturation	28
2.5 Quantitative evaluation	30
Chapter 3 The Improved <i>HSV</i> Perceptive Color Model	33
3.1 The color patch analysis of traditional <i>HSV</i> color model	34
3.2 <i>RGB</i> and <i>iHSV</i> conversion	35
3.3 The mutual influence between intensity and saturation	39
Chapter 4 Color Image Enhancement	42
4.1 The color image enhancement with <i>eHSI</i> color model	42

4.2 The color image enhancement with <i>iHSV</i> color model.....	44
Chapter 5 Cloud Removal Approaches for Aerial Image Visualization	47
5.1 Multi-spectral image enhancement	47
5.2 Cloud detection.....	52
5.2.1 <i>The gradient-based method</i>	52
5.2.2 <i>The spatial-frequency analysis method</i>	54
5.2.3 <i>Linear spectral unmixing (LSU) method</i>	57
5.2.4 <i>The color-based method</i>	59
5.3 Image fusion	61
5.3.1 <i>Determining the augmented zone</i>	61
5.3.2 <i>Color uniformity</i>	62
5.3.3 <i>Multi-scale fusion</i>	64
Chapter 6 Experiments and Discussions	68
6.1 Color image enhancement with <i>eHSI</i> color model	68
6.2 Color image enhancement with <i>iHSV</i> color model.....	73
6.3 Cloud removal	79
Chapter 7 Conclusions	83
References	87

List of Figures

Fig. 1.	The attainable maximum saturation at different intensity values for a fixed hue region from 0° to 6°	7
Fig. 2.	The procedure of the proposed color image enhancement scheme based on the <i>eHSI</i> or <i>iHSV</i> color model.	10
Fig. 3.	The color patch analysis. (a) The color patches of the <i>RGB</i> cube. (b) The color patches of the <i>HSI</i> color model. (c) The top-viewed <i>HSI</i> color model.	18
Fig. 4.	Details of the <i>eHSI</i> triangle for acquiring an accurate saturation component. (a) The top view of the $C'M'Y'$ triangle. (b) Oblique top view for deriving <i>RGB</i> to <i>eHSI</i> conversion formulas. (c) Side view for deriving <i>eHSI</i> to <i>RGB</i> conversion formulas.....	22
Fig. 5.	The boundary for determining to use the traditional saturation formula or the exact saturation formula. If a pixel is located under the boundary, the pixel's saturation is calculated by the traditional <i>HSI</i> formulas; otherwise, the pixel's saturation is calculated by the proposed <i>eHSI</i> formulas.....	23
Fig. 6.	The color patches of the <i>eHSI</i> color model. (a) The oblique top view. (b) The side view.	23
Fig. 7.	The saturation variation coincides with the intensity change. (a) Saturation change in the <i>HSI</i> color space. (b) Saturation change in the <i>eHSI</i> color space.....	29
Fig. 8.	The influence of intensity on saturation. There are two real numbers in each square; the upper number is the intensity, and the lower number is the saturation. (a) A low-intensity artificial image. (b) The intensity is increased $1/3$ in the <i>HSI</i> color space. (c) The intensity is increased $1/3$ in the <i>eHSI</i> color space. (d) A high-intensity artificial image. (e) The intensity is decreased $1/6$ in the <i>HSI</i> color space. (f) The intensity is decreased $1/6$ in the <i>eHSI</i> color space.....	32
Fig. 9.	The calculation of Intensity and saturation is based on the geometric distance of the <i>RGB</i> cube.....	32
Fig. 10.	The color patches analysis. (a) The color patches of the traditional <i>HSV</i> color model. (b) The intensity restored <i>HSV</i> color space. We	

observed that the value component of the outer circle of <i>RGBCYM</i> is lowered to 0.5. This is more conformable to the original intensity in <i>RGB</i> cube. (c) The color patches of <i>iHSV</i> color model. We observed that not only the value components were restored but also the saturation components were normalized. Hence the out-of-gamut problem was avoided.	38
Fig. 11. The mutual influence between intensity and saturation. (a) The intensity and saturation changes in <i>HSV</i> color space. (b) The intensity and saturation changes in <i>iHSV</i> color space.	41
Fig. 12. The value level of 0.5 in <i>iHSV</i> color space.....	41
Fig. 13. The saturation is enhanced by using an <i>S-type</i> transformation to centralize the intensities to the intensity center area where the attainable maximum saturation range is wider. (a) The side view of the <i>RGB</i> cube. (b) The <i>S-type</i> transformation.....	45
Fig. 14. The saturation enhancement by using the <i>S-type</i> function. (a) The side view of <i>RGB</i> cube. (b) Using the <i>S-type</i> function to centralize the intensity histogram.	45
Fig. 15. The color map of an image. (a) The original image. (b) The value components of all pixels being changed to 0.5 in <i>iHSV</i> color space. (c) The value component of all pixels being changed to 1 in <i>HSV</i> color space.....	46
Fig. 16. The diagram of the proposed system for cloud removal.	48
Fig. 17. The enhancement result of a color image. (a) and (b) The original image. (c) and (d) The intensity histogram of original image is linearly stretched. (e) and (f) The intensity histogram is concentrated by an <i>S-type</i> function.	50
Fig. 18. The saturation variation coincides with the intensity adjustment and the comparison of cloud extraction based on the traditional <i>HSI</i> and the proposed <i>eHSI</i> color models. (a) The cloud areas enhanced in <i>HSI</i> color space, we observed that the cloud areas are not pure white. (b) The cloud areas enhanced in <i>eHSI</i> color space, we observed that the cloud areas are pure white. (c) The cloud areas are extracted from the <i>HSI</i> -enhanced image. (d) The cloud areas are extracted from the <i>eHSI</i> -enhanced image. In all cases, the cloud threshold value is (0.97, 0.97, 0.97).....	51

Fig. 19. The gradient-based cloud segmentation. (a) The low-gradient regions after thresholding. (b) Excluding low-difference area from (a) and then eliminating small fragments. (c) Superimpose on one source image. (d) Another segmentation result in which some small broken clouds cannot be detected.	54
Fig. 20. The frequency-based cloud detection. (a) The low spatial frequency regions. (b) Excluding low difference area from (a) and then eliminating small fragments. (c) Superimpose on one source image. (d) Another case.	56
Fig. 21. Examples of mixed pixels.....	58
Fig. 22. The cloud segmentation result based on the <i>LSU</i> method. (a) The cloud areas detected by <i>LSU</i> method. (b) The cloud areas in (a) are processed by opening operator.....	58
Fig. 23. The intensity thresholding-based cloud detection. (a) The high intensity areas. (b) Eliminating the low difference areas from (a) and then eliminating the small fragments. (c) Superimposing on the source image. (d) Another case.....	60
Fig. 24. The cloud zones and augmentative zones. (a) Original base image and the cloud detected zones and the augmentative zones are clipped. (b) The clipped zones are patched with the same areas in another replacing image. (c) Replacement with the color corrected image. (d) The multi-scale image fusion result.	63
Fig. 25. The decomposition and re-combination procedure of Gaussian pyramid and Laplacian pyramid.	65
Fig. 26. Multiscale image fusion. (a) The Gaussian pyramid of mask image (b) The fusion process at different level of resolution.....	67
Fig. 27. The enhanced results of Tiffany image. (a) The original image. (b) (c) (d) Intensity histogram is equalized in <i>HSI</i> , <i>CIELAB</i> , and <i>eHSI</i> spaces, respectively. (e) (f) (g) Intensity histogram is centralized by <i>S-type</i> transformation in <i>HSI</i> , <i>CIELAB</i> , and <i>eHSI</i> spaces, respectively.....	70
Fig. 28. The enhanced results of the brightened cosmetic image. (a) The original image. (b) The brightened image. (c) (e) (g) Intensity histogram is equalized in <i>HSI</i> , <i>CIELAB</i> , and <i>eHSI</i> spaces, respectively. (d) (f) (h) Intensity histogram is centralized by <i>S-type</i>	

transformation in <i>HSI</i> , <i>CIELAB</i> , and <i>eHSI</i> spaces, respectively.....	71
Fig. 29. The enhanced results of the darkened cosmetic image. (a) The darkened image. (b) (d) (f) Intensity histogram is equalized in <i>HSI</i> , <i>CIELAB</i> , and <i>eHSI</i> spaces, respectively. (c) (e) (g) Intensity histogram is centralized by <i>S-type</i> transformation in <i>HSI</i> , <i>CIELAB</i> , and <i>eHSI</i> spaces, respectively.	72
Fig. 30. The enhancement result of the Tiffany image. (a) The original image. (b) Contrast enhancement result with histogram equalization in the <i>HSV</i> color space. (c) Contrast enhancement result with histogram equalization in the <i>iHSV</i> color space. (d) Saturation enhancement in <i>HSV</i> color space with the <i>S-type</i> function. (e) Saturation enhancement in <i>iHSV</i> color space with the <i>S-type</i> function.	75
Fig. 31. The histogram variations of the Tiffany image in different color spaces. (a) The intensity histogram of original image. (b) The value histogram of original image in <i>HSV</i> color space. (c) The value histogram of original image in <i>iHSV</i> color space. (d) The value histogram equalized in <i>HSV</i> color space. (e) The value histogram equalized in <i>iHSV</i> color space.....	76
Fig. 32. The enhancement result of the car image. (a) Original image. (b) The enhancement result by using histogram equalization in the <i>HSV</i> color space. (c) The enhancement result by using histogram equalization in the <i>iHSV</i> color space. (d) Saturation enhancement in <i>HSV</i> color space with the <i>S-type</i> function. (e) Saturation enhancement in <i>iHSV</i> color space with the <i>S-type</i> function.	77
Fig. 33. The histogram variations of the car imasge in different color spaces. (a) The intensity histogram of original image. (b) The value histogram of original image in <i>HSV</i> color space. (c) The value histogram of original image in <i>iHSV</i> color space. (d) The value histogram of (b) processed by histogram equalization. (e) The value histogram of (c) processed by histogram equalization.	78
Fig. 34. Another example of cloud removal. (a) and (b) The original cloudy images. (c) and (d) The detected cloud areas by using the intensity thresholding and difference checking method. (e) The cloud detected zones and transition zones. (f) The final fusion result.	82

List of Tables

Table 1. The comparison of cloud detection among the eight methods. 81

Chapter 1

Introduction

Color image enhancement is widely used in many applications such as digital images and video [1, 2]. However, the out-of-gamut problem and the de-correlation problem between the independent intensity and saturation enhancement procedures are still unsolved, or solved with a complicated method. Histogram equalization is a well-known image contrast enhancement method and has been used for various image enhancements [3-6]. The color images enhanced by this method often have unnatural appearances and visually disturbing artifacts. One reason for the unwanted effect is that histogram equalization tends to force the output images to have a uniform color distribution regardless of the original color distribution. Another reason is that the color transformation makes the color histogram distorted. A better solution is to take into account the original color distribution when enhancing a color image to ensure that the output image will not only have enhanced visibility and contrast but also be faithful to the original appearance. Furthermore, the hue components of the pixels should not be changed for color image enhancement. If we change the hue, the appearance of the original color is changed significantly, and then the image color is distorted.

1.1 Motivation

To preserve the appearance of the original image, usually the original *RGB* images are first transformed into perceptual color spaces such as the *HSI* (Hue-Saturation-Intensity), *HSV*, or *HSL* (Hue-Saturation-Luminance), and then the intensity and saturation components are enhanced with the hue component unaltered. Many color models have been proposed for various applications. Each color model has its advantages and disadvantages. Most of the existent color

models are linear conversion. For example, the popular color model *CIELAB* is perceptually uniform but still has the out-of-gamut problem. On the other hand, the *HSI* and *HSV* color models are nonlinear conversion and have human-intuitive advantages in image processing. They are widely adopted for many applications such as color image enhancement, segmentation, fusion, color-based object detection, recognition, traffic signal detection, skin color detection, etc. However, they still have some defects. We tried to improve them so that they can not only solve the out-of-gamut problem but also the de-correlation problem between intensity and saturation in color image enhancement procedure.

Furthermore, in cloud removal application, white color of cloud is an important feature for cloud detection. Hence we expect the improved color models can not only suitable for color aerial image enhancement but also for cloud detection.

1.2 Related work

Strickland *et al.* [7] proposed an enhancement scheme based on the fact that objects can exhibit variation in color saturation with little or no corresponding intensity variation. Thomas *et al.* [8] proposed an improvement over Strickland's method by considering the correlation between the intensity and saturation components of the image locally. Toet [9] also extended Strickland's method to incorporate all spherical frequency components by representing the original intensity and saturation components of a color image at multiple spatial scales. Pitas and Kiniklis [10] proposed a method to jointly equalize the intensity and saturation components. Trahanias and Venetsanopoulos [11] proposed a method of direct 3D histogram equalization that results in a uniform histogram of the *RGB* values. Mlsna and Rodriguez [12] proposed a multivariate enhancement technique, called “histogram explosion,”

in which the equalization procedure is performed on a series of rays emanating from a common point in a 3D histogram. This principle was later extended to the *CIE LUV* space [13]. The authors also proposed a recursive algorithm for 3D histogram enhancement of color images [14]. Bockstein [15] proposed a color equalization method for both saturation and intensity.

Weeks *et al.* [16] proposed a hue-preserving color image enhancement technique that modifies the saturation and intensity components in a color difference (*C-Y*) space. At first, an image is transformed into the *C-Y* color space (*e.g.*, *YCbCr*) and then segmented into N hue regions and K luminance regions. To avoid the out-of-gamut problem, the values for the maximum realizable saturation $S_{max}(n, k)$, $n = 1, 2, 3, \dots, N$ and $k = 1, 2, 3, \dots, K$, are computed by searching all possible *RGB* combinations and selecting the corresponding maximum saturation value for the hue-intensity combination. This computation is performed once for the desired number of regions, and then the results are stored in a table where the values can be used repeatedly by the equalization algorithm. The authors proposed two methods to equalize the intensity and chromatic components. The first method equalizes the intensity and then equalizes the saturation component based on the enhanced intensity. The second method equalizes the saturation component and then equalizes the intensity component by referring to the enhanced saturation. The different order affects the intensity value if the saturation is limited in the saturation equalization process. The first method may generate images with high contrast and brightness but low saturation. The result comes from increasing the overall range of luminance but limiting the maximum realizable saturation. The second method tends to produce images with high saturation but low brightness and contrast because the high-saturated color limits the allowed intensities in the *RGB* space to a small range. Duan and Qiu [17] mentioned that the more the regions are divided, the fewer cross-session artifacts there are, but more computational time

is needed. Each method has its own advantages and disadvantages; but there is no specific criterion to decide which component should be enhanced first. In addition, there is no specific criterion for deciding the parameters N and K ; moreover, calculating the lookup table is complicated.

Naik and Murthy [18] indicated that though the mentioned algorithms are effective for enhancement, most do not effectively take care of the gamut problem in which the pixel values go beyond the boundaries after processing. Due to the nonlinear nature of uniform color spaces, conversion from these spaces with modified intensity and saturation values to the *RGB* space generates the gamut problem. In general, the problem is tackled by either clipping the out-of-boundary values to the boundaries or normalizing the entire intensity and saturation ranges [15]. Clipping the values to the boundaries creates an undesired shift in the hue. Strickland *et al.* [7] also discussed the clipping problem. Normalization reduces the intensity achieved in the enhancement process, which defeats the original objective [19]. In the above studies, we find there are some problems, such as the contradictions among color components, out-of-gamut, and complicated algorithms. None of those studies proposed a general correction method suitable for different kinds of enhancement and few of them went deep into the relationship between saturation and intensity.

Some color image enhancement algorithms directly enhance the images in the *RGB* color space rather than in other color spaces. Yang and Rodriguez [20] proposed two hue-preserving techniques, scaling and shifting, for processing intensity and saturation components. To implement the techniques, all pixels are processed in the *RGB* space; this means that transformation of the color coordinates is not necessary. Later, the authors also developed clipping techniques [21] in the *LHS* and *YIQ* spaces for enhancement by dealing in particular with the values that fall outside the range of the *RGB* space, where clipping is performed after the enhancement. Rodriguez and Yang [22] also

proposed a high-resolution histogram equalization of color images. The effect of quantization error in the luminance quantization has been studied in detail.

Naik and Murthy [18] suggested a novel and effective way of handling the gamut problem during the processing itself. It is not necessary to bring back the *RGB* values to its bounds after the processing. The enhancement procedure suggested is hue preserving. It generalizes the existing gray level image enhancement techniques to color images. The processing has been done in the *RGB* space and the saturation and hue components of pixels aren't needed for the processing. However, these methods adjusts the intensity and saturation in the *RGB* color space so that some traditional enhancement algorithms which were developed in the *HSI* or *HSV* color space need to be re-deduced or obsolete. On the other hand, manipulating the intensity and saturation in the *RGB* color space does not reflect the intuitive color notion or perception of human vision and is less intuitional than in the *HSI* and *HSV* color spaces.

1.3 The perceptive color model

The hue-saturation-intensity (*HSI*) color model partially encounters the out-of-gamut problem. It describes more exact color than *RGB* model describes for human interpretation [23]. Though the *HSI* model is non-uniform in perception, it is still one of the most popular color models for color image processing. More than 4,670 papers in recent four years (2006-2009) were extracted when we used “*HSI* color” as the keyword to search papers in “Google Scholar” web site. In practical applications, the non-uniformity in perception can be solved by some techniques. For example, in color image segmentation, the deformed boundaries can be used to enclose the target cluster so that the perception uniformity is not so critical. The out-of-gamut problem is really the knotty problem. This study just focuses on solving the out-of-gamut problem for color image enhancement and clarifying the drawback of the traditional *HSI*.

color model. The whole process is unconcerned with the perception uniformity.

Though the transformation between *HSI* and *RGB* models is nonlinear, the transformation theoretically makes the intensity and saturation of manipulated pixels never out of gamut if the manipulation is limited in the range of [0, 1]. Furthermore, if a pixel's intensity is changed, its saturation component is automatically tuned according to the attainable maximum saturation range. Unfortunately, the *HSI* color system is deduced from the three low-intensity planes of the *RGB* cube so that the previous mentioned advantages is successfully achieved in low intensity portion but failed in high intensity portion. Duan and Qiu [17] mentioned that, in the *HSI* color space, the attainable maximum saturation is actually a function of the intensity in the same hue plane as shown in Fig. 1. We practiced color patch analysis and found that the complete *HSI* color model was distorted on the upper portion as [described in Section 2.1](#).

This distortion makes several undesirable phenomena; for example, a pixel's saturation component is automatically increased after conversion from the *HSI* space to the *RGB* space with increased intensity. Hence, the pixel is possibly out of gamut. On the other hand, the saturation is always reduced if the intensity is reduced in the *HSI* color space, whether the attainable maximum saturation ranges is wide or narrow. Consequently, the intensity of an image is correct, but the saturation is decreased; then an extra saturation enhancement procedure is necessary. In the spectra of light, each color is at the maximum purity (or strength or richness) that eyes can appreciate, and the spectrum of colors is described as fully saturated. If a saturated color is diluted by mixing with other colors or white, the color's richness or saturation is decreased [24]. Hence, correct saturation enhancement will produce a more pleasant image. Several enhancement methods have been proposed; however, the enhancement of saturation is not so easy. For example, (i) the attainable maximum saturation

range in the middle intensity region is wider than those in the high- and low-intensity regions so that enhancing saturation must be coordinated with the change of intensity. (ii) The histogram equalization may generate uneven enhanced results for large smooth segments in images. (iii) To avoid an oversaturated image, the pixels in the achromatic segments must not be enhanced, but the achromatic segments are difficult to determine in the image.

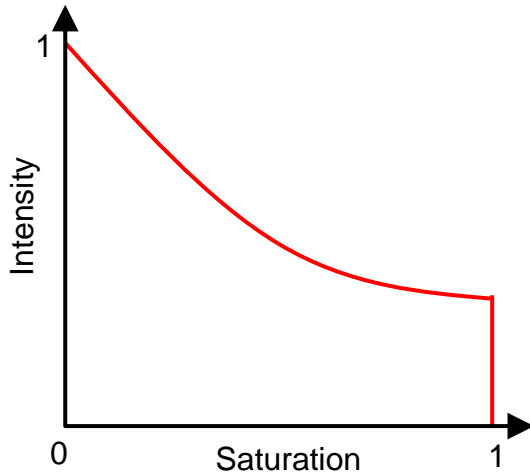


Fig. 1. The attainable maximum saturation at different intensity values for a fixed hue region from 0° to 6° .

The tri-stimulus values of the *HSV* color model can be regarded as the characteristics perceived by the human vision system (*HVS*). The *HSV* system describes more exactly the color system than the *RGB* system in the sense that the *HVS* does recognize colors in terms of the *HSV* tri-stimulus values (*H*, *S*, and *V*) instead of the *RGB* tri-stimulus ones (*R*, *G*, and *B*). Though the *HSV* color model is non-uniform in perception, it is still one of the most popular color systems used in color image manipulation. The *HSV* transformation is one of the pre-defined functions in the *MATLAB* and *OpenCV* library due to its popularity and simple calculation. However, the proposed research deals with color image enhancement. The focus is on clarifying the drawback of the traditional *HSV* color space and proposing a new color model to improve it. The whole process

is unconcerned with the perception uniformity and thus the perception uniformity is less relevant.

The *HSV* color model does not have the out-of-gamut problem, is more intuitionial than the *RGB* color model, and is based on the psychological feelings of human eyes on colors. However, the *RGB* to *HSV* conversion has some defects so that the enhanced results in the *HSV* model are unsatisfying in some cases; for example, in some conditions, speckles will appear in the uniform regions if an image is enhanced with the value histogram equalization in the *HSV* color space.

1.4 Color image enhancement

Weeks *et al.* [16] mentioned that the color enhancement procedure usually suffers from not only the out-of-gamut problem but also the contradiction between intensity and saturation. To resolve both problems, we propose an exact *HSI* (*eHSI*) color model that not only prevents pixels from going out of gamut but also adaptively adjusts the saturation according to the ratio of the target and the source attainable maximum saturation range rather than following the intensity change. In the proposed approach, a color image is first transformed from *RGB* to the proposed *eHSI* color space. Then, we use histogram stretching or histogram equalization to expand the intensity histogram and enhance the contrast of the color images. On the other hand, to enhance the saturation, we may deform the shape of the intensity histogram by moving the intensity mean to the central point (*e.g.*, 128 for 256 gray scales) and then stretching the intensity range on one side of the mean and compressing that on the other side of mean. This operation makes more pixels fall into the region with “larger saturation expansion range” in the color space. Some histograms are dispersed such as a bi-modal histogram with two peaks locating near the two ends, so that the previous operation is useless. Thus, if the saturation enhancement result is

not very conspicuous, we can add an *S-type* transformation [18] to concentrate the intensity in the central region which has a larger saturation range. Then, the image is conversed back to the *RGB* space to complete the enhancement.

Furthermore, we propose an improved *HSV* color model (*iHSV*) whose value histogram is more compatible with the intensity histogram in the *RGB* color model than the conventional *HSV* color model. Moreover, the saturation component in the *iHSV* color model is automatically and linearly rectified according to the target attainable maximum saturation ranges at different value levels so that the correlation between value and saturation can be preserved.

The procedure of image enhancement based on the *eHSI* and *iHSV* color model is described in Fig. 2. After the *eHSI* or *iHSV* color transformation, we use histogram stretching or histogram equalization to expand the value histogram. Furthermore, to enhance the saturation of color images, the value histogram is concentrated in the central region by using an *S-type* function. This transformation moves most pixels to the region of the maximum attainable saturation range. Finally, the processed value component and the original hue and saturation components are converted back to the *RGB* space. During the process, the hue component is unchanged and the saturation component is automatically enhanced when we concentrate the value component in the central region, but the contrast will be mildly sacrificed.

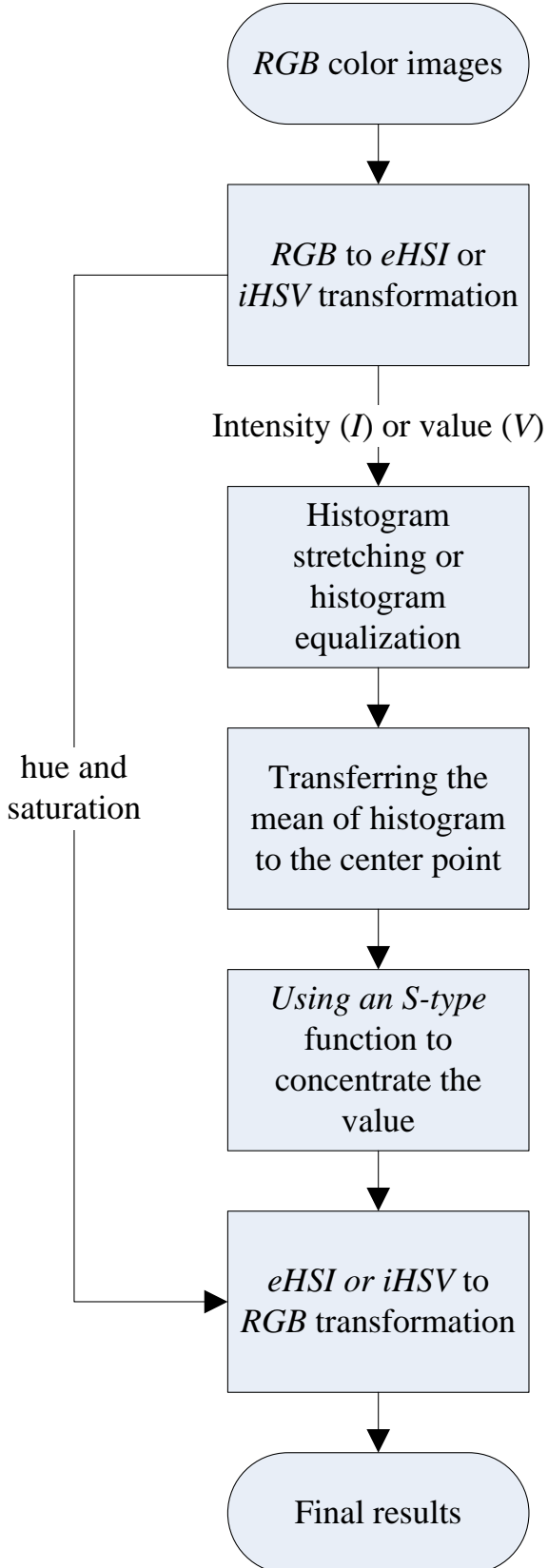


Fig. 2. The procedure of the proposed color image enhancement scheme based on the *eHSI* or *iHSV* color model.

1.5 Cloud removal in satellite images

In recent decades, a tremendous amount of remote sensing images has been received and widely used for many applications, such as geographical visualization, terrain visualization, scene analysis, land-use classification, landscape ecological change detection, etc. However, no matter for what purpose Earth resource satellite images are used, the first step is to extract landscape information from the images. Due to weather conditions, the images acquired from satellites may be interfered with clouds and cloud shadows, especially in humid tropical areas. In general, cloud cover doesn't always appear at the same location; if multiple images were acquired at different times over a specific region, the cloud cover problem may be resolved from complementary multi-temporal images. In other words, it is possible to generate cloud-free images by fusing the cloud-free areas of the images, assuming that the land covers have only a little change in the period of image acquisition.

The generation of cloud-free satellite images is a traditional topic. The complete steps for producing cloud-free images generally include: image enhancement, cloud determination, and image fusion, but most studies only focus on the last two steps. Three different kinds of cloud-removal approaches have been proposed: (i) treating cloud as noise and removing it, (ii) using multi-spectral images to fuse and generate cloud-free images, and (iii) using multi-temporal images to fuse and generate cloud-free images.

The first-kind methods [25] generally use spectral information to filter out the cloud pixels. However, bright and large land-cover areas have similar spectral characteristics to clouds and may also be filtered out; moreover, denoising methods cannot completely recover the land covers blocked by the clouds. The second-kind methods [26-28] only use multi-spectral images to detect and remove clouds. Generally, the clouds appear in almost bands of

multi-spectral images; thus the clouds can only be treated as noise, and similar results to the first-kind methods are obtained. The third-kind methods [29-35] are the mainstream; most researchers use both multi-spectral and multi-temporal data accompanied by various algorithms to generate cloud-free images. These methods used intensity thresholding [34], band-ratio classification with size/shape checking [32], pixel ranking [33], reflectance difference checking with other regions [35], *NDVI* test [29], or regression tree modeling with histogram matching [31] to decide cloud or non-cloud regions. Gabarda and Cristóbal [30] used a 1-D pseudo-Wigner distribution (*PWD*) transformation and a pixel-wise cloud model to fuse partial-cloudy images to generate cloud-free images. Sometimes the above-mentioned methods can achieve good results, but most methods are too simple to completely detect cloud regions. We used a linear spectral unmixing (*LSU*) method to extract all cloud regions according to the material information [36]; the *LSU* method is good for hyper-spectral images, but is weak for fewer-spectral (multi-spectral) images. Multi-spectral images have only three spectral data; this is not enough to separate the cloud and white land-cover regions [36].

After cloud regions are extracted, these regions may be regionally replaced with cloud-free portions, and then a fusion method is used to reduce the visual difference on clipped boundaries of the regions that come from different temporal images. Several wavelet-based methods have been proposed [37-39] for cloud detection or image fusion. Burt and Adelson [37] proposed a multi-resolution spline approach for image blending. Wang *et al.* [35] proposed an automated cloud detection method by simply thresholding the high frequency components of the discrete wavelet transform of two fusing images. Kubo *et al.* [38] represented the cloud distribution as texture, and then used Gabor wavelet transform to detect local regularity to extract cloud regions. Li *et al.* [39] used non-separable wavelet frame transform (*NWFT*) to fuse two registered images;

one is a high spatial-resolution panchromatic image and the other is a low spatial-resolution multi-spectral image. Arellano [29] applied wavelet transform to detect clouds and cloud shadows then filled out the missing information in a multi-temporal set of *ASTER* images.

Most related studies did not consider the problem of image enhancement to make the multi-temporal images have less visual difference in their fused images; for example, the images on Google Earth. In this study, a complete multi-temporal approach is proposed to produce cloud-free and cloud-shadow-free fused images. At first, all original *RGB* images are transformed into our proposed exact *HSI* (*eHSI*) color space and intensity components are enhanced. This study targets the aerial geometrical visualization like the *Google Earth*; thus, the original *RGB* aerial images were used. Secondly, an intensity thresholding is used to extract all cloud pixels. The intensity thresholding cannot handle thin clouds and cloud shadow, and often confuses bright land surfaces with clouds. Thus, we utilize a difference comparison method to eliminate unnecessary marking on plain areas or large buildings by comparing the difference with other temporal images. A morphology opening operator is then used to exclude small bright areas. Subsequently, we choose the base image that has the least thin cloud cover and divide the base image into grid zones to find the thin-cloud and cloud-shadow zones in the eight neighbors of the thick cloud zones based on the relative locations and the sun's elevation angle. Finally, the cloud and cloud-shadow zones of the base image are replaced with the same-location cloud-free zones on the other temporal images, and then a pyramid multi-scale fusion method is used to generate cloud-free fused images with proper brightness and saturation.

1.6 The dissertation organization

The rest of the paper is organized as follows. The proposed transformation between *eHSI* and *RGB* is derived and presented in [Chapter 2](#). The difference between the *eHSI* and the traditional *HSI* color models is analyzed and discussed in [Sections 2.4 and 2.5](#). The out-of-gamut problem in the traditional *HSI* color model could be completely resolved in the proposed *eHSI* color model.

The conversions between the *iHSV* and *RGB* color models are derived and presented in [Chapter 3](#) and the difference between the improved *HSV* and the traditional *HSV* color models is analyzed and discussed in [Section 3.3](#). It's found that the value histogram of the *iHSV* color model is similar to the intensity histogram of the *RGB* color model and is no longer concentrated in the high value portion. Hence the value components of high saturation pixels are not highly separated from those of the low saturation pixels anymore.

However, the saturation of high- or low-intensity pixels is still reduced when they are converted back to the *RGB* space. To improve the saturation of an image, an *S-type* transformation is used to enhance the saturation by sacrificing a little contrast of value as presented in [Chapter 4](#).

[Chapter 5](#) describes the cloud removal approaches from multi-temporal *SPOT* images. The satellite images enhancement method in the proposed *eHSI* color space is described in [Section 5.1](#). [Section 5.2](#) presents the proposed method for determining cloud and cloud-shadow zones in the base image. [Section 5.3](#) presents the pyramid multi-scale fusion method to make seams invisible in the fused images.

Several practical color image enhancement experiments with *eHSI* or *iHSV* color model are reported and discussed in [Chapter 6](#). [Section 6.3](#) reports the experiments of the proposed methods on image enhancement, cloud determination, and image fusion. Finally, conclusions are given in [Chapter 7](#).

Chapter 2

The Exact *HSI* Perceptive Color Model

Converting color from *RGB* to the traditional *HSI* is defined as [23]:

$$\left\{ \begin{array}{l} I = \frac{R + G + B}{3} \\ H = \begin{cases} \theta & , \text{if } B \leq G \\ 360^\circ - \theta & , \text{if } B > G \end{cases} \\ \text{with } \theta = \cos^{-1} \left\{ \frac{\frac{1}{2}[(R-G)+(R-B)]}{[(R-G)^2+(R-B)(G-B)]^{1/2}} \right\} \\ S = 1 - \frac{3}{R+G+B} \min(R, G, B) \end{array} \right. \quad (1)$$

where I and S are in the range of $[0, 1]$ and H is in the range of $[0, 360]$.

To convert color from the *HSI* to *RGB*, three cases of the H range must be considered.

RG section: $0^\circ \leq H < 120^\circ$

$$\left\{ \begin{array}{l} B = I(1 - S) \\ R = I \left[1 + \frac{S \cos H}{\cos(60^\circ - H)} \right] \\ G = 3I - (R + B) \end{array} \right. \quad (2)$$

GB section: $120^\circ \leq H < 240^\circ$

$$H = H - 120^\circ$$

$$\left\{ \begin{array}{l} R = I(1 - S) \\ G = I \left[1 + \frac{S \cos H}{\cos(60^\circ - H)} \right] \\ B = 3I - (R + G) \end{array} \right. \quad (3)$$

BR section: $240^\circ \leq H < 360^\circ$

$$H = H - 240^\circ$$

$$\begin{cases} G = I(1 - S) \\ B = I \left[1 + \frac{S \cos H}{\cos(60^\circ - H)} \right] \\ R = 3I - (G + B) \end{cases} \quad (4)$$

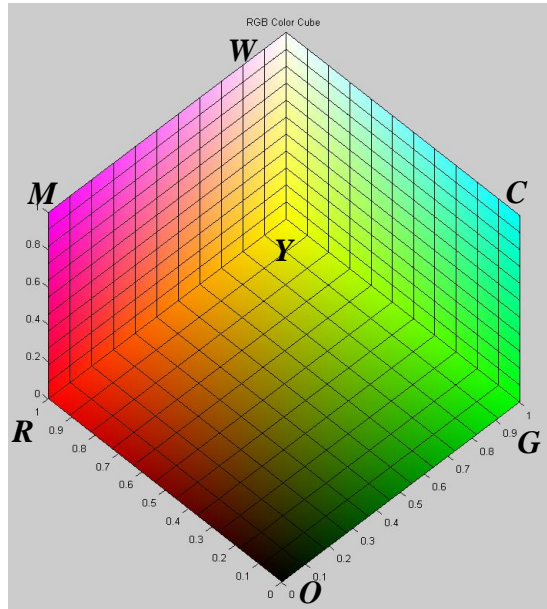
2.1 The color patch analysis of traditional *HSI* color model

Color patches analysis is a visual tool and can be used to understand the shapes of different color models. We use this tool to verify the correctness of the proposed *eHSI* and *iHSV* color models. To observe the 3D model of different color spaces, we pasted color patches all over the surface of a color model. We first divided each face of the *RGB* cube into $11 \times 11 = 121$ patches. The vertices of every color patch were defined by their *RGB* coordinates. The color in every patch was defined by the interpolation of the four patch vertices with the reciprocal of the distance being the interpolation weight, as illustrated in Fig. 3 (a). We then transferred the vertex coordinates of all patches to the *HSI* color space and kept the vertices and face colors unchanged as illustrated in Fig. 3 (b) and (c). The lower part of the *HSI* model is cylindrical (you may look the hexagonal shape at the bottom due to the discrete patches), but the upper part is deformed because the *HSI* color transformation is deduced from the three low-intensity planes of the *RGB* cube (*i.e.*, the *ORYG*, *OGCB*, and *OBMR* planes) as illustrated in Fig. 3 (a); thus, the three high-intensity planes (*i.e.*, the *WYRM*, *WMBC*, and *WCGY* planes) are distorted.

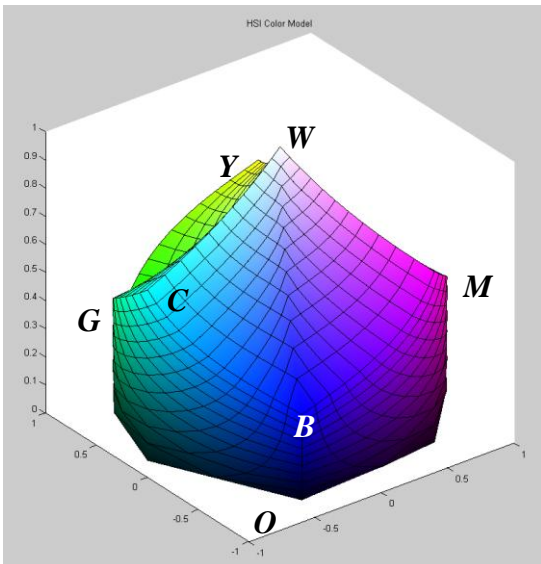
This distorted model will generate several unusual phenomena after the intensity is enhanced. First, the color of a pixel may go out of gamut. If the intensity or saturation of some pixels is increased so that they are out of the top

surface of the *HSI* model, the out-of-gamut problem will be generated and their intensity and saturation values will be clipped when they are transformed back to the *RGB* space. Second, if a pixel's intensity is increased by an enhancement procedure, the pixel's saturation will be linearly expanded; on the other hand, if a pixel's intensity is decreased, the pixel's saturation will be linearly shrunk whether the target saturation range is wider or narrower. The details will be described in [Section 2.4](#).

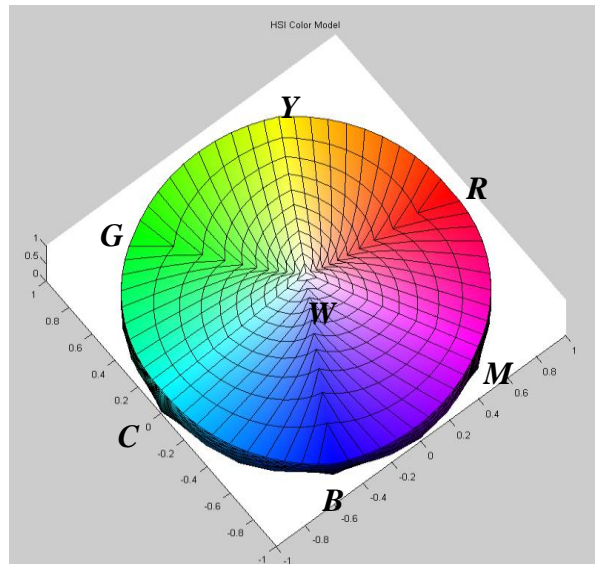
To resolve the out-of-gamut and shrunken saturation problems, we improved the *HSI* color transformation formulas. The idea is that if the intensity is higher than certain boundaries, then the *HSI* formulas will be derived from the three high-intensity planes in the *RGB* cube (*i.e.*, the *WYRM*, *WMBC*, and *WCGY* planes) as illustrated in [Fig. 3 \(a\)](#).



(a)



(b)



(c)

Fig. 3. The color patch analysis. (a) The color patches of the *RGB* cube. (b) The color patches of the *HSI* color model. (c) The top-viewed *HSI* color model.

2.2 *RGB* to *eHSI* transformation

We can derive the saturation for the *eHSI* model based on the geometric structure of the *RGB* cube as shown in Fig. 4 (b). In the figure, an arbitrary color point p has coordinates (R, G, B) and is located on the triangle $C'M'Y'$ that is perpendicular to the black-white gray axis and intersects the axis at u point. The saturation of a color is defined as the degree to which the color is diluted by white; thus, the saturation S of color point p is given by the ratio $|\overline{up}|/|\overline{up}'|$, where p' is the intersection of the extension of \overline{up} line and one border of the triangle $C'M'Y'$. Let t be the orthogonal projection of u on the *WCM* plane, and let q be the orthogonal projection of p on the \overline{ut} line. According to the two similar triangles Δupq and $\Delta up't$, we have

$$S = \frac{|\overline{up}|}{|\overline{up}'|} = \frac{|\overline{uq}|}{|\overline{ut}|} = \frac{|\overline{ut}| - |\overline{qt}|}{|\overline{ut}|}. \quad (5)$$

From Fig. 3 (b), we can find that q and p have the same B value; thus, $|\overline{qt}| = 1 - B$. Furthermore, we can find that the length $|\overline{Wu}|$ is

$$|\overline{Wu}| = \frac{\overline{Wp} \cdot (1, 1, 1)}{\|(1, 1, 1)\|} = \frac{(1-R) + (1-G) + (1-B)}{\sqrt{3}}. \quad (6)$$

If the coordinate of u is (ω, ω, ω) , then $|\overline{ut}|$ is $1 - \omega$. Since

$$|\overline{Wu}| = \sqrt{3(1-\omega)^2} = \frac{(1-R) + (1-G) + (1-B)}{\sqrt{3}} = \sqrt{3}(1-I), \quad (7)$$

then

$$1 - \omega = \frac{(1-R) + (1-G) + (1-B)}{3} = 1 - I. \quad (8)$$

That is,

$$|\bar{ut}| = \frac{(1-R)+(1-G)+(1-B)}{3} = 1 - \frac{(R+G+B)}{3} = 1 - I \quad (9)$$

in the presented (*CM*) section; thus,

$$S = 1 - \frac{3(1-B)}{3 - (R+G+B)}. \quad (10)$$

From [Figs. 3 \(a\) and 4 \(b\)](#), we can find $B = \max(R, G, B)$ in the *CM* section. Hence, the saturation can be formularized as

$$S = 1 - \frac{3(1 - \max(R, G, B))}{3 - (R+G+B)}. \quad (11)$$

The same results can be acquired for the two other sections, the *MY* and *YC* sections, with a similar derivation.

In applications, we must have a criterion to judge using the traditional saturation formula or the proposed saturation formula. That is, if the attainable maximum saturation of a pixel is located in the three high-intensity planes of the *RGB* cube, then the pixel's saturation should be calculated by the proposed saturation calculation; otherwise, the pixel's saturation is calculated by the traditional saturation calculation. The boundary between the traditional saturation and the new saturation regions is shown in [Fig. 5](#). Based on the intensity and hue values, if a pixel is above the boundary, the new formula is used; otherwise, the traditional formula is used. In practice, we divide the hue range into three sections ($[0, 120]$, $[120, 240]$, and $[240, 360]$) and then use the central point of each section as the reference point. If a pixel's hue angle is equal to the central point (*i.e.*, 60° , 180° , or 300°) and the pixel's intensity is greater than $1/3$, then the new saturation formula is used. On the other hand, if a pixel's hue angle is equal to the boundary point of each section (*i.e.*, 0° , 120° , or 240°) and the pixel's intensity is greater than $2/3$, then the new saturation formula is used. Hence the calculation of saturation accompanying the decision criterion is

summarized as

$$\left\{ \begin{array}{l} H = H \bmod 120^\circ \\ \\ \text{if } I > \frac{2 - \text{abs}(H - 60^\circ)}{3}, \text{ then} \\ \quad S = 1 - \frac{180^\circ}{3 - (\max(R, G, B))} \\ \\ \text{else} \\ \quad S = 1 - \frac{3}{R + G + B} \min(R, G, B). \end{array} \right. \quad (12)$$

The computational burden of the transformation from *RGB* to *eHSI* is not much higher than the traditional *HSI* since the extra load is just the calculation “ $H = H \bmod 120^\circ$ ” and the decision in Eq. (12).

We have transformed the color patches on the *RGB* cube to the *eHSI* model as illustrated in Fig. 6. The upper portion of the *eHSI* model is a perfect cylinder; that is, the *eHSI* model is undistorted and is correct.

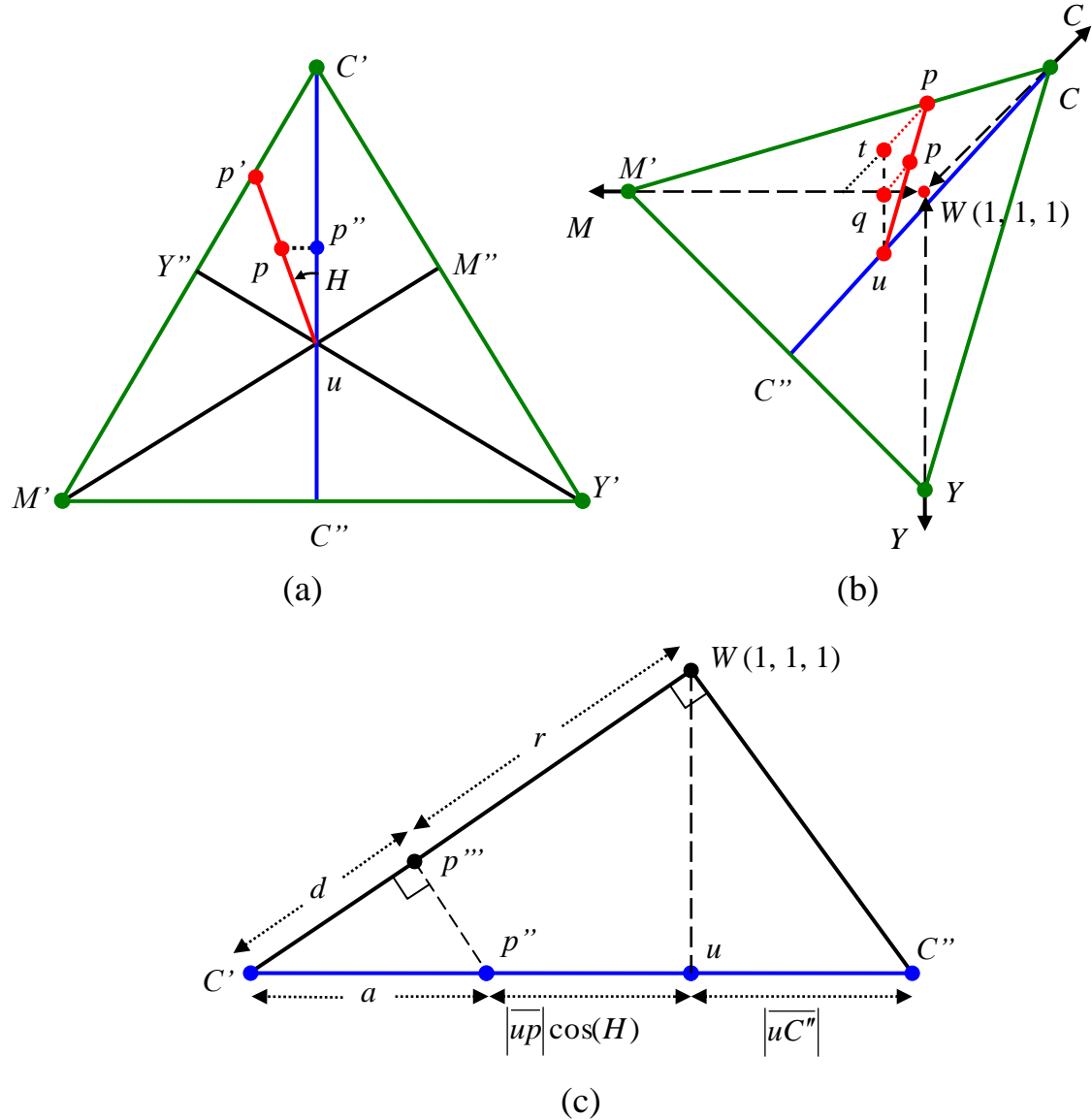


Fig. 4. Details of the *eHSI* triangle for acquiring an accurate saturation component. (a) The top view of the $C'M'Y'$ triangle. (b) Oblique top view for deriving *RGB* to *eHSI* conversion formulas. (c) Side view for deriving *eHSI* to *RGB* conversion formulas.

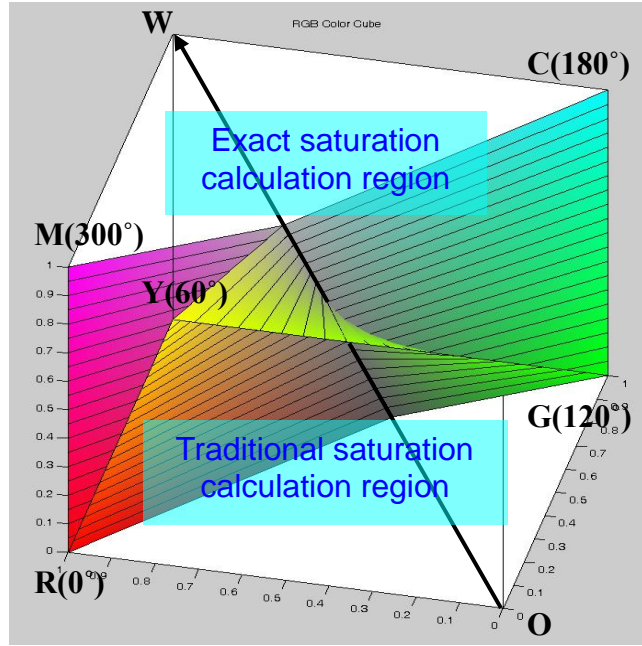


Fig. 5. The boundary for determining to use the traditional saturation formula or the exact saturation formula. If a pixel is located under the boundary, the pixel's saturation is calculated by the traditional *HSI* formulas; otherwise, the pixel's saturation is calculated by the proposed *eHSI* formulas.

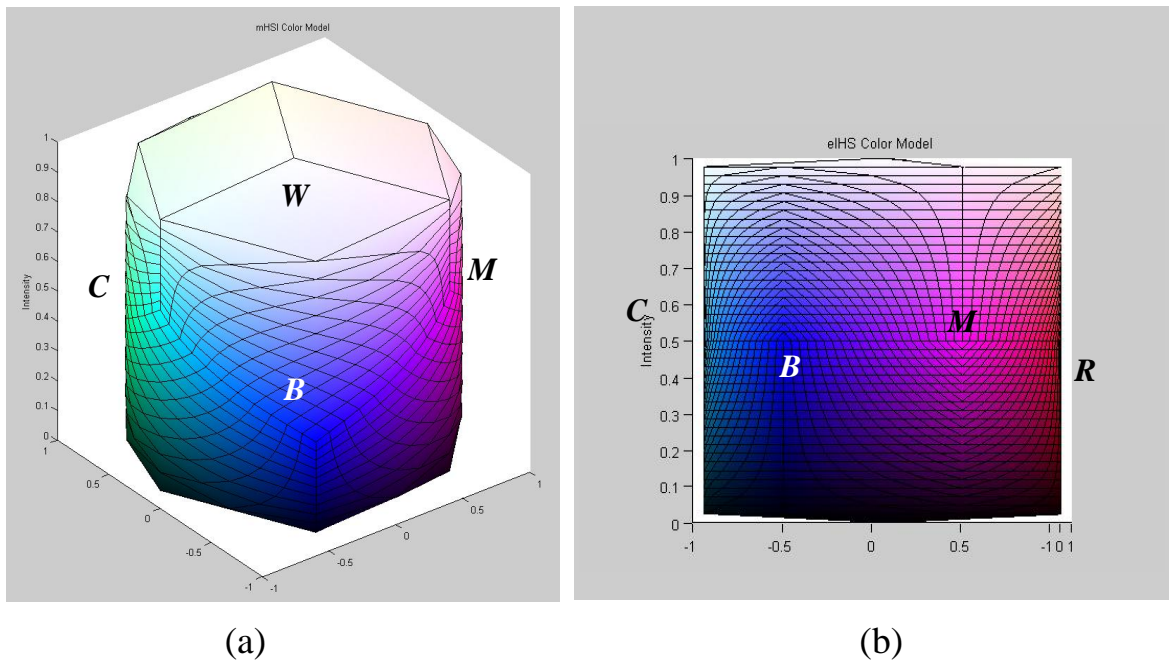


Fig. 6. The color patches of the *eHSI* color model. (a) The oblique top view. (b) The side view.

2.3 *eHSI* to *RGB* transformation

We need conversion formulas from *eHSI* to *RGB* after the processing is completed in the *eHSI* color space. The traditional transformation is separated into three cases: the *RG*, *GB*, and *BR* sections to convert *HSI* to *RGB*. For the *eHSI* to *RGB* transformation, we must consider six cases: the *RG*, *GB*, *BR*, *CM*, *MY*, and *YC* sections. The former three cases are the same as the traditional transformation, but the intensity component must be restricted. That is,

$$\text{The } RG \text{ section: } 0 < H \leq 120^\circ \text{ & } I \leq \frac{2}{3} - \frac{\text{abs}(H - 60^\circ)}{180^\circ}$$

$$\begin{cases} B = I(1 - S) \\ R = I \left[1 + \frac{S \cos H}{\cos(60^\circ - H)} \right] \\ G = 3I - (R + B) \end{cases} \quad (13)$$

$$\text{The } GB \text{ section: } 120^\circ < H \leq 240^\circ \text{ & } I \leq \frac{2}{3} - \frac{\text{abs}(H - 180^\circ)}{180^\circ}$$

$$H = H - 120^\circ$$

$$\begin{cases} R = I(1 - S) \\ G = I \left[1 + \frac{S \cos H}{\cos(60^\circ - H)} \right] \\ B = 3I - (R + G) \end{cases} \quad (14)$$

$$\text{The } BR \text{ section: } 240^\circ < H \leq 360^\circ \text{ & } I \leq \frac{2}{3} - \frac{\text{abs}(H - 300^\circ)}{180^\circ}$$

$$H = H - 240^\circ$$

$$\begin{cases} G = I(1 - S) \\ B = I \left[1 + \frac{S \cos H}{\cos(60^\circ - H)} \right] \\ R = 3I - (G + B) \end{cases} \quad (15)$$

For the CM , MY , and, YC sections, the conversion formulas should be modified based on the 3D geometric structure of the CM , MY , and YC sections. For the CM section ($180^\circ < H \leq 300^\circ$), the S component can be derived from Eq. (10); that is,

$$S = 1 - \frac{1-B}{1-I} , \quad (16)$$

then

$$B = I(1-S) + S . \quad (17)$$

From Fig. 4 (b) and (c), we can find that the value of r is the orthogonal projection of \overline{Wp} on the C axis. Consider the triangle $\Delta C'WC''$ shown in Fig. 4 (c), where W is the highest point $(1, 1, 1)$ of the RGB coordinate system. From the two similar triangles $\Delta C'WC''$ and $\Delta C'p''p''$, we have

$$\frac{|\overline{C'C''}|}{|\overline{C'W}|} = \frac{a}{d} , \quad (18)$$

where p'' is the orthogonal projection of p on the $\overline{C'C''}$ line, and p''' is the orthogonal projection of p'' on the $\overline{C'W}$ line. We derived the length $|\overline{Wu}|$ in Eq. (7). Accordingly, if the coordinates of C' are $(\delta, 1, 1)$, then the length of $|\overline{C'W}|$ is equal to $1-\delta$. Since

$$\frac{((1, 1, 1) - (\delta, 1, 1)) \cdot (1, 1, 1)}{|(1, 1, 1)|} = \frac{1-\delta}{\sqrt{3}} = |\overline{Wu}| ; \quad (19)$$

hence,

$$|\overline{C'W}| = \sqrt{3} |\overline{Wu}| = 3(1-I) . \quad (20)$$

From Fig. 4 (a) and (c) and Eq. (20), we have

$$d = |\overline{C'W}| - r, \quad (21)$$

$$a = |\overline{C'C''}| - (\overline{|up|} \cos H + \overline{|uC''|}), \quad (22)$$

and

$$|\overline{C'C''}| = 3 |\overline{uC''}|. \quad (23)$$

Substituting Eqs. (18), (20), (22), and (23) into Eq. (21) and simplifying yields

$$\begin{aligned} r &= |\overline{C'W}| - d = |\overline{C'W}| - \frac{a |\overline{C'W}|}{|\overline{C'C''}|} = |\overline{C'W}| \left(\frac{\overline{|up|} \cos H + \overline{|uC''|}}{|\overline{C'C''}|} \right) \\ &= 3(1-I) \left(\frac{1}{3} + \frac{\overline{|up|} \cos H}{|\overline{C'C''}|} \right) = (1-I) \left(1 + \frac{3 \overline{|up|} \cos H}{|\overline{C'C''}|} \right). \end{aligned} \quad (24)$$

The only unknown in this equation is $|\overline{up}|$. In Fig. 4 (a), we know that $|\overline{up}| = S |\overline{up'}|$. At u , the angle included by the line segments $\overline{uC'}$ and $\overline{uY''}$ is 60° ; thus, $|\overline{up'}| = |\overline{uY''}| / \cos(60^\circ - H)$. We know that $|\overline{uY''}| = |\overline{uC''}|$; hence, $|\overline{up'}| = |\overline{uC''}| / \cos(60^\circ - H)$. Substituting these results and Eq. (23) into Eq. (24) yields

$$\begin{aligned} r &= (1-I) \left(1 + \frac{3S |\overline{up'}| \cos H}{|\overline{C'C''}|} \right) = (1-I) \left(1 + \frac{3S |\overline{uC''}| \cos H}{|\overline{C'C''}| \cos(60^\circ - H)} \right) \\ &= (1-I) \left(1 + \frac{S \cos H}{\cos(60^\circ - H)} \right). \end{aligned} \quad (25)$$

As illustrated in Figs. 3 (a) and 4 (c), the coordinates of W are $(1, 1, 1)$; thus, R can be obtained by

$$R = 1 - r = 1 - (1-I) \left(1 + \frac{S \cos H}{\cos(60^\circ - H)} \right). \quad (26)$$

Since $I = (R + G + B)/3$, we then have

$$G = 3I - (R + B). \quad (27)$$

Similar results can be acquired for the MY and YC sections in the same derivation manner. The final conversion formulas for the YC , CM , and MY sections are summarized as follows.

$$\text{The } YC \text{ section: } 60^\circ < H \leq 180^\circ \text{ & } I > \frac{1}{3} + \frac{\text{abs}(H - 120^\circ)}{180^\circ}$$

$$H = H - 240^\circ$$

$$\begin{cases} G = I(1 - S) + S \\ B = 1 - (1 - I) \left[1 + \frac{S \cos H}{\cos(60^\circ - H)} \right] \\ R = 3I - (G + B) \end{cases}. \quad (28)$$

$$\text{The } CM \text{ section: } 180^\circ < H \leq 300^\circ \text{ & } I > \frac{1}{3} + \frac{\text{abs}(H - 240^\circ)}{180^\circ}$$

$$\begin{cases} B = I(1 - S) + S \\ R = 1 - (1 - I) \left[1 + \frac{S \cos H}{\cos(60^\circ - H)} \right] \\ G = 3I - (B + R) \end{cases}. \quad (29)$$

$$\text{The } MY \text{ section: } \left(300^\circ < H \leq 360^\circ \text{ & } I > \frac{1}{3} + \frac{360^\circ - H}{180^\circ} \right) \text{ or } \left(0^\circ < H \leq 60^\circ \text{ & } I > \frac{1}{3} + \frac{H}{180^\circ} \right)$$

$$H = H - 120^\circ$$

$$\begin{cases} R = I(1 - S) + S \\ G = 1 - (1 - I) \left[1 + \frac{S \cos H}{\cos(60^\circ - H)} \right] \\ B = 3I - (R + G) \end{cases}. \quad (30)$$

The MY section is across 0° boundary, so hue angles less than 0° and greater than 0° should be considered with different intensity ranges.

The computational burden of the transformation from *eHSI* to *RGB* is also not much higher than from the traditional *HSI* since the extra load is only the decision for [Eqs.\(13\) - \(15\) and \(28\) - \(30\)](#).

We also used the previous patch analysis to verify the correctness of the *eHSI* to *RGB* transformation. The reversed *RGB* cube is completely the same as the original *RGB* cube; thus, we confirmed that the proposed *eHSI* to *RGB* transformation is correct. The proposed new *HSI* color model creates an exact color transformation between *RGB* and *HSI*; thus we call it the exact *HSI (eHSI)* color model.

2.4 The influence of intensity on saturation

We use a geometric graph to explore the co-variation of intensity and saturation in the *HSI* and the *eHSI* color spaces. Moreover, we use a color palette to verify the correctness of the relationship between intensity and saturation.

We have stated that the traditional *HSI* is derived from the low-intensity planes of the *RGB* cube. Since the three planes are expanded outward as the intensity is increased, we speculate that the saturation is always enhanced as the intensity is increased. As illustrated in [Fig. 7 \(a\)](#), if the intensity of pixel “*a*” is increased from L_1 to L_2 in the *HSI* color space, this means that pixel “*a*” is transferred to “*b*”. In this case, “*b*” is out of gamut, but actually, the pixel’s intensity is bounded by the *RGB* cube and can’t reach L_2 level. On the other hand, if the intensity of pixel “*c*” is decreased from L_2 to L_1 , the pixel’s location is transferred to “*d*”, and the pixel’s saturation is always decreased.

In the proposed *eHSI* color model, the maximum saturation is coincident with the attainable maximum saturation range in the *RGB* space; the out-of-gamut problem is solved and the saturation is adjusted according to the

attainable maximum saturation range. As illustrated in Fig. 7 (b), if the intensities of pixels “ a ” and c are increased from L_1 to L_2 , their locations are transferred to “ b ” and “ d ”, respectively; but the pixels’ saturations are adaptively changed according to the border structure of the color space. The saturation expansion range for “ d ” is wider than for “ c ”, so the pixel’s saturation is enhanced; on the other hand, the saturation expansion range for “ b ” is narrower than that for “ a ”, so the pixel’s saturation is reduced. In the $eHSI$ space, there is no out-of-gamut problem, and the change in saturation depends completely on the relative saturation ranges of the target and the original intensity levels. In image enhancement, if the saturation range of the target intensity level is greater than that of the original intensity level, the saturation is enhanced; otherwise, the saturation is reduced. This is beneficial for saturation enhancement; that is, if we sacrifice a little contrast and push the pixel’s intensity toward the central region on the intensity axis, the saturation is automatically enhanced.

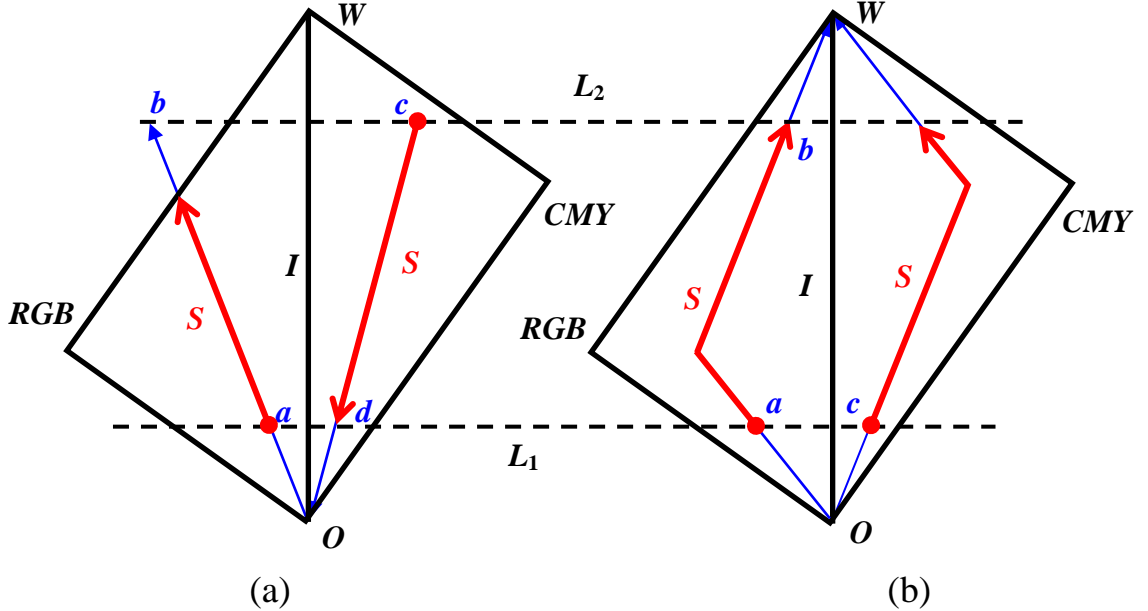


Fig. 7. The saturation variation coincides with the intensity change. (a) Saturation change in the HSI color space. (b) Saturation change in the $eHSI$ color space.

2.5 Quantitative evaluation

To quantitatively evaluate the influence of intensity on saturation while the intensity is being adjusted, we create a color palette with six rectangle color blocks to verify the proposed transformation as illustrated in Fig. 8 (a). The six colors are the pure R , Y , G , C , B , and M ; their hues are just 0° , 60° , 120° , 180° , 240° , and 300° . Every color block is divided into left and right squares. All six left squares have $1/3$ the intensity and the maximum saturation, and all six right squares have $1/6$ the intensity and $1/2$ the maximum attainable saturation. In the figure, there are two real numbers in each square; the upper number is the intensity, and the lower number is the saturation. The intensity is in the range of $[0, 1]$ and the saturation value is calculated from the geometric distance on the RGB cube.

The saturation calculation of the high-intensity portion is different for the HSI and the $eHSI$ color spaces. To compare the results, we must unify the saturation values by using the geometric distance on the RGB cube as the unit. As illustrated in Fig. 9, the length of the intensity axis (\overline{OW} axis) is $\sqrt{3}$. The saturation value is directly calculated from the perpendicular distance to the intensity axis. The orthogonal projection of p on the \overline{OW} axis is

$$\frac{(R, G, B) \cdot (1, 1, 1)}{\sqrt{3}} = \frac{R + G + B}{\sqrt{3}}, \quad (31)$$

so that the perpendicular distance S is

$$S = \sqrt{R^2 + G^2 + B^2 - \frac{(R + G + B)^2}{3}} = \sqrt{\frac{(R - B)^2 + (B - G)^2 + (G - R)^2}{3}}. \quad (32)$$

For example, the saturation of $(1, 0, 0)$ in the traditional representation is 1, but here the saturation will become $\sqrt{\frac{(1-0)^2 + (0-0)^2 + (0-1)^2}{3}} = \sqrt{\frac{2}{3}} \approx 0.8165$.

Next, we add $1/3$ to the intensity of every rectangle block of the color palette; that is, the intensity of the left squares becomes $2/3$, and that of the right squares becomes $1/2$. According to the previous analysis, we predict that, in the *HSI* color space, the pure R , G , and B pixels will become out of gamut after their intensity exceeds $1/3$. As shown in Fig. 8 (b), the intensity and saturation of the left squares of the R , G , and B blocks are not changed, but those of the right squares are enhanced. This is an unusual phenomenon that the intensity of the right squares exceeds that of the left squares after the intensity is increased because the left squares are out of gamut and bounded by the *RGB* cube. On the other hand, the intensity and saturation of the C , Y , and M blocks are all enhanced. Contrary to the *HSI* color space, the intensity in the *eHSI* color space is normally changed as illustrated in Fig. 8 (c); the saturation of all the squares is increased or decreased according to the attainable saturation range as described in Fig. 7 (b).

Another analysis is illustrated in Fig. 8 (d). The left square of every rectangle block has $2/3$ the intensity and the maximum saturation, and all six right squares have $1/2$ the intensity and the maximum attainable saturation. Now, we subtract $1/6$ from the intensity of every rectangle block. In the *HSI* color space, the intensity and saturation of all blocks are all reduced as illustrated in Fig. 8 (e). Contrarily, in the *eHSI* color space, the intensity of all blocks is reduced, but the saturations of the R , G , and B blocks are enhanced as illustrated in Fig. 8 (f). The target saturation expansion range is wider than the source expansion range.

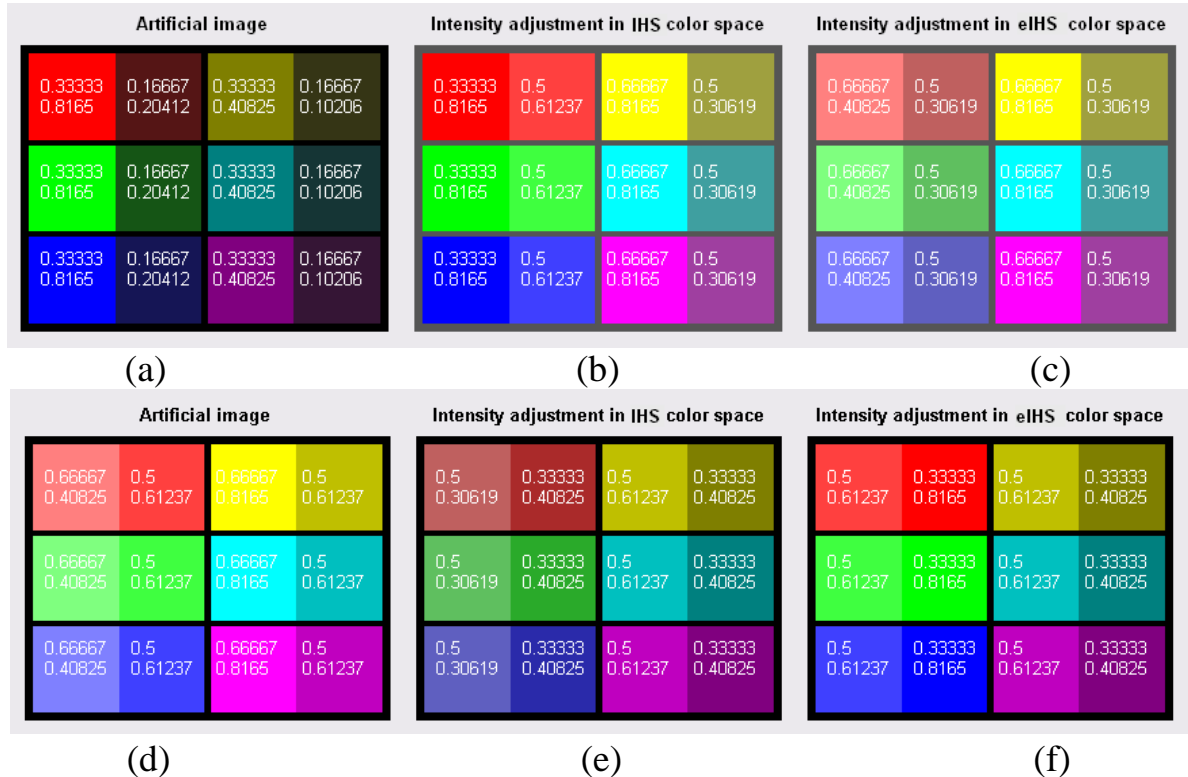


Fig. 8. The influence of intensity on saturation. There are two real numbers in each square; the upper number is the intensity, and the lower number is the saturation. (a) A low-intensity artificial image. (b) The intensity is increased 1/3 in the *HSI* color space. (c) The intensity is increased 1/3 in the *eHSI* color space. (d) A high-intensity artificial image. (e) The intensity is decreased 1/6 in the *HSI* color space. (f) The intensity is decreased 1/6 in the *eHSI* color space.

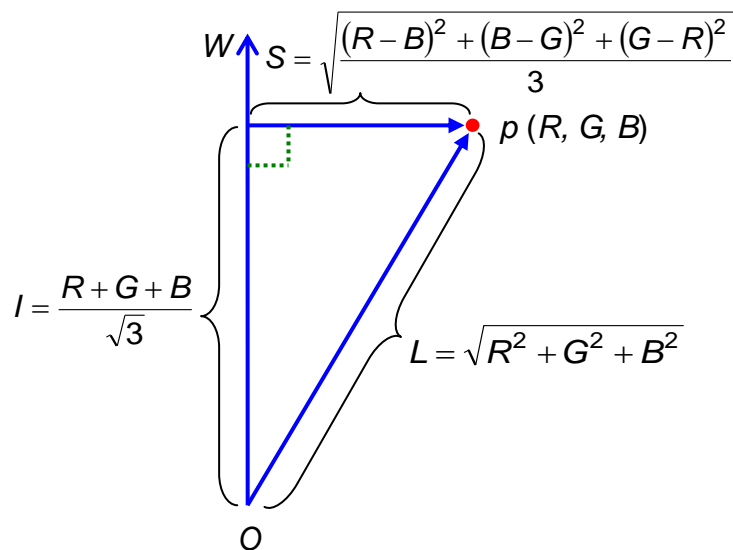


Fig. 9. The calculation of Intensity and saturation is based on the geometric distance of the *RGB* cube.

Chapter 3

The Improved *HSV* Perceptive Color Model

The *HSV* color space is one of the popular color spaces due to its simple computation where no trigonometric function is involved. Many libraries including MATLAB® and OpenCV have provided the transformation formulas between the *RGB* and *HSV* color spaces. The *RGB* to *HSV* conversion is defined as follows [40]:

$$\left\{ \begin{array}{l} H = 60 \frac{G - B}{\max(R, G, B) - \min(R, G, B)} + 0, \quad \text{if } R > G, R > B, \text{ and } G \geq B, \\ H = 60 \frac{G - B}{\max(R, G, B) - \min(R, G, B)} + 360, \quad \text{if } R > G, R > B, \text{ and } G < B, \\ H = 60 \frac{B - R}{\max(R, G, B) - \min(R, G, B)} + 120, \quad \text{if } G > R \text{ and } G > B, \\ H = 60 \frac{R - G}{\max(R, G, B) - \min(R, G, B)} + 240, \quad \text{if } B > R \text{ and } B > G, \end{array} \right. \quad (33)$$

the saturation (*S*) is defined as

$$S = \frac{\max(R, G, B) - \min(R, G, B)}{\max(R, G, B)}, \quad (34)$$

and the value (*V*) is defined as

$$V = \max(R, G, B). \quad (35)$$

On the other hand, the *R*, *G*, and *B* in the *HSV* to *RGB* conversion are obtained by defining

$$H' = \left\lfloor \frac{H}{60} \right\rfloor \bmod 6, \quad (36)$$

where the floor operator $\lfloor \cdot \rfloor$ returns a maximum integer which is less than or equal to the quotient;

$$\begin{cases} f = \frac{H}{60} - H', \\ p = V(1 - S), \\ q = V(1 - fS), \\ t = V(1 - (1 - f)S), \end{cases} \quad (37)$$

According to the H' , f , p , q , t , the R , G and B are obtained as

$$\begin{cases} \text{if } H' = 0, \text{ then } R = V, G = t, B = p, \\ \text{if } H' = 1, \text{ then } R = q, G = V, B = p, \\ \text{if } H' = 2, \text{ then } R = p, G = V, B = t, \\ \text{if } H' = 3, \text{ then } R = p, G = q, B = V, \\ \text{if } H' = 4, \text{ then } R = t, G = p, B = V, \\ \text{if } H' = 5, \text{ then } R = V, G = p, B = q, \end{cases} \quad (38)$$

3.1 The color patch analysis of traditional *HSV* color model

In the *HSV* color space, the value components of fully saturated pixels such as the R , G , B , C , Y and M are all equal to 1, which is not matched with the conventional intensity in the *RGB* color space where the intensity of the R , G , and B is equal to 1/3 and of the C , Y , and M equal to 2/3. On the other hand, the same-value area is increased as the value is increased as illustrated in Fig. 10 (a). The value histogram in the *HSV* color space is condensed in the high-value region. The value component of the low saturation pixels is separated from that of the high saturation ones though their intensities in the *RGB* color space are identical. Furthermore, the value component of the low saturation pixels is highly separated from that of the high saturation pixels if histogram equalization is used. In addition, the saturation component is always decreased if the value is

decreased no matter the target attainable maximum saturation range is wider or narrower.

From the color patches analysis, we observed that the value components of the fully saturated pixels such as the R , G , B , C , M , and Y were all over-transformed so that they were all equal to 1, *i.e.*, the value of white (W). This characteristic will lead to some undesired results such as the speckles in the uniform regions if the image is enhanced in a traditional HSV color space. To solve the problems in the traditional HSV color space, we propose an improved HSV color space, the $iHSV$, to better the color image enhancement.

3.2 RGB and $iHSV$ conversion

First, we restore the value component to a proper position so that the value histogram is matched with the Gaussian distribution characteristic of the intensity histogram in the RGB color space. For that purpose, the value components of the pixels around the circle of R , G , B , C , M , and Y should be located at half of the maximum value. Hence we modify the value component as

$$\begin{aligned} V' &= V \left(1 - \frac{S}{2} \right) = \max(R, G, B) \left(1 - \frac{\max(R, G, B) - \min(R, G, B)}{2 \max(R, G, B)} \right) \\ &= \frac{\max(R, G, B) + \min(R, G, B)}{2} \end{aligned} \quad (39)$$

As illustrated in Fig. 10 (b), the value components of the R , G , B , C , M , and Y are restored to a more reasonable position; they are all equal to 0.5. However, the maximum saturation values of the upper half portion are not normalized to 1. To avoid the out-of-gamut problem, we normalize the saturation of the upper half portion to be in the range of [0, 1] in the second step. That is, the saturation S of the upper half portion is modified as follows:

If $0.5 < V' \leq 1$, then

$$\begin{aligned} S' &= \frac{S}{2 - 2V'} = \frac{\frac{\max(R, G, B) - \min(R, G, B)}{\max(R, G, B)}}{2 - (\max(R, G, B) + \min(R, G, B))} \\ &= \frac{\max(R, G, B) - \min(R, G, B)}{\max(R, G, B)(2 - \max(R, G, B) - \min(R, G, B))}. \end{aligned} \quad (40)$$

The saturation of the lower half portion is the same as that of the original. As shown in Fig. 10 (c), the improved *HSV* (*iHSV*) color space is a perfect cylinder. The out-of-gamut problem can be avoided if the value and saturation components are manipulated in the range of [0, 1].

For the *iHSV* to *RGB* conversion, we first restore the improved saturation and value components to the traditional *HSV* color space and then use the traditional *HSV* to *RGB* conversion to transform the color values back to the *RGB*. The restoration of saturation is

if $0.5 < V' \leq 1$, then

$$S = S'(2 - 2V'), \quad (41)$$

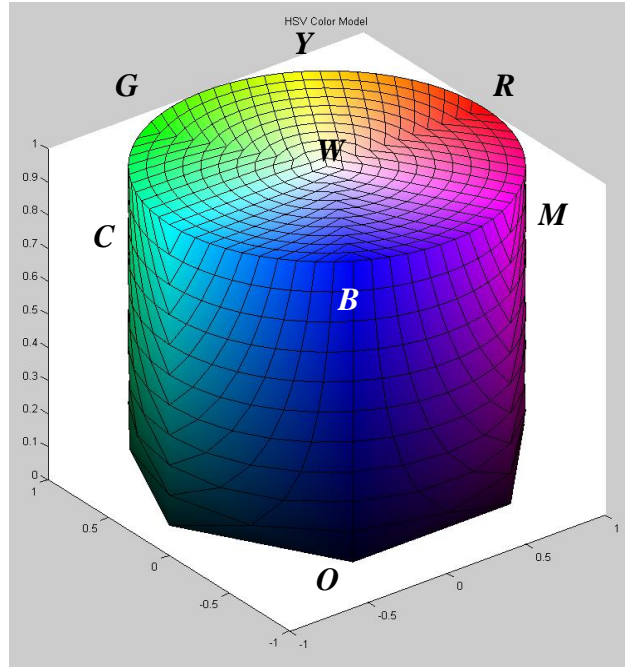
and the value restoration is

$$V = \frac{2V'}{2 - S}. \quad (42)$$

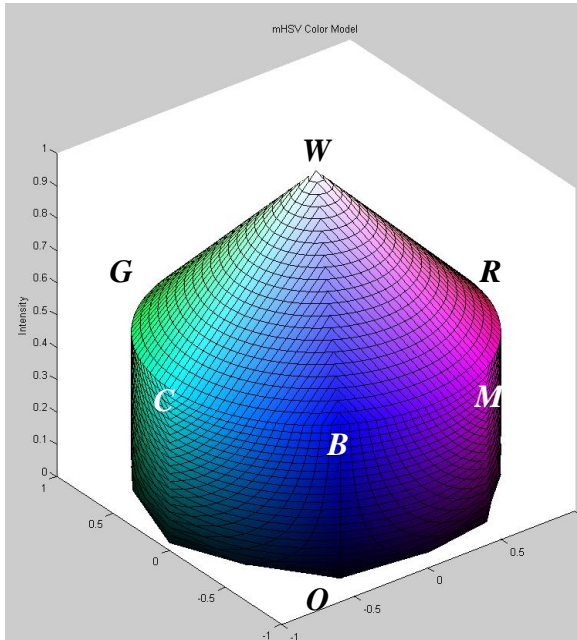
Then the *HSV* components are transformed to the *RGB* color space.

The *iHSV* color space has several advantages. Firstly, compared with the conventional *HSV* color space, the value histogram in the *iHSV* color space is better matched with the intensity histogram in the *RGB* color space. Secondly, after the *iHSV* to *RGB* conversion, the desired intensity in the *RGB* color space

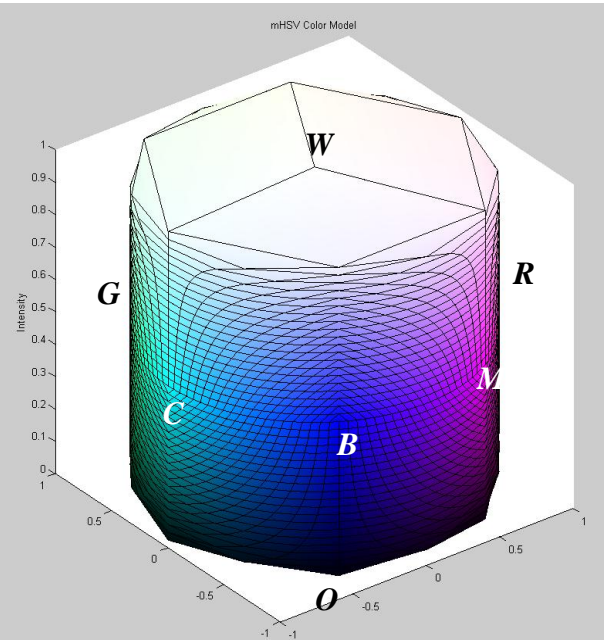
can be achieved by tuning the value component in the *iHSV* color space and will not be bounded by the *WYGC*, *WCBM*, and *WMRY* three planes of the *RGB* cube. Finally, the saturation component is automatically and linearly tuned according to the attainable maximum saturation range and the correlation between the value and saturation components is preserved. Hence the saturation enhancement can be achieved by applying an *S-type* function. After the transformation with the *S-type* function, the value component is centralized in the central region which has a wider attainable saturation range.



(a)



(b)



(c)

Fig. 10. The color patches analysis. (a) The color patches of the traditional *HSV* color model. (b) The intensity restored *HSV* color space. We observed that the value component of the outer circle of *RGBCYM* is lowered to 0.5. This is more conformable to the original intensity in *RGB* cube. (c) The color patches of *iHSV* color model. We observed that not only the value components were restored but also the saturation components were normalized. Hence the out-of-gamut problem was avoided.

3.3 The mutual influence between intensity and saturation

We use a geometric model to explore the co-variation of intensity and saturation in *HSV* and *iHSV* color spaces. As described in Eq. (35), the value component (V) in the *HSV* color space is equal to the maximum value of the R , G , and B components in the *RGB* color space so the planes of identical-value points in the *HSV* color space are parallel to one of the *WYGC*, *WCBM*, and *WMRY* three planes of the *RGB* cube as shown in Fig. 11 (a). For example, the planes V_1 and V_2 are parallel to the ceiling of the *RGB* cube. If the value component of pixel “ a ” is increased from V_1 to V_2 , pixel “ a ” is transferred to “ b ”. On the other hand, if the value component of pixel “ c ” is decreased from V_2 to V_1 , “ c ” is transferred to “ d ”. The *HSV* color space produces several undesired effects:

- (i) If the value component of a pixel is reduced, the pixel’s saturation component will be reduced. On the other hand, the pixel’s saturation component is increased if its value component is increased.
- (ii) The value component of high-saturated pixels is bounded by the *WYGC*, *WCBM*, and *WMRY* three planes of the *RGB* cube and can’t be tuned to higher value level.
- (iii) There are more accumulation of value histogram at the higher value and saturation level and less accumulation at the lower value and saturation level, so the value histogram is concentrated in the higher value level region.
- (iv) The value components of low saturation pixels are separated from that of high saturation pixels although their intensities are the same in the *RGB* color space. Furthermore, they are more and more separated from each other after value histogram equalization, which is due to the distortion of

the value histogram described in (iii).

As shown in [Fig. 11 \(a\)](#), the range of value histogram accumulation at value level V_2 is wider than that at value level V_1 . For example, the pixels at the maximum value level, *i.e.*, from *RGB* to *W* to *CYM*, are all accumulated as the maximum value level of the value histogram. If we enhance a bright image with value histogram equalization, most pixels' intensity and saturation of the image will be reduced and some speckles will be generated in the uniform regions. We will demonstrate the examples in [Section. 6](#).

The proposed *iHSV* color space does not have the above-mentioned problems. As illustrated in [Fig. 11 \(b\)](#), its value level is parallel to the *RGBCYM* surface shown in [Fig. 12](#) in which the value of same-value surface is equal to 0.5. The saturation components of the pixels are automatically tuned according to the attainable maximum saturation range of the target value position. As shown in [Fig. 11 \(b\)](#), if the value components of pixels “*a*” and “*c*” are increased from level V_1 to level V_2 , the pixels will be transferred to “*b*” and “*d*”. Moreover, the value level is unbounded and can be freely increased until the highest value level. Furthermore, the range of value histogram accumulation at the central value level is wider than that at both end levels. Hence the value histogram is not concentrated in the high value level region and is similar to the Gaussian distribution of the intensity histogram in the *RGB* color space.

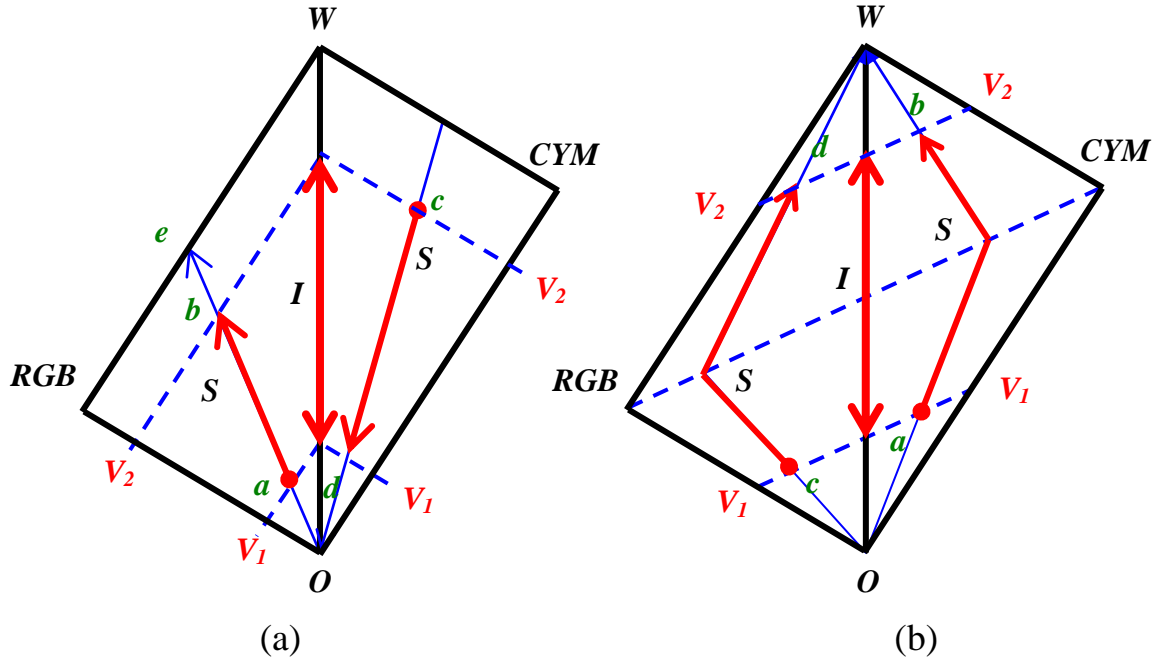


Fig. 11. The mutual influence between intensity and saturation. (a) The intensity and saturation changes in *HSV* color space. (b) The intensity and saturation changes in *iHSV* color space.

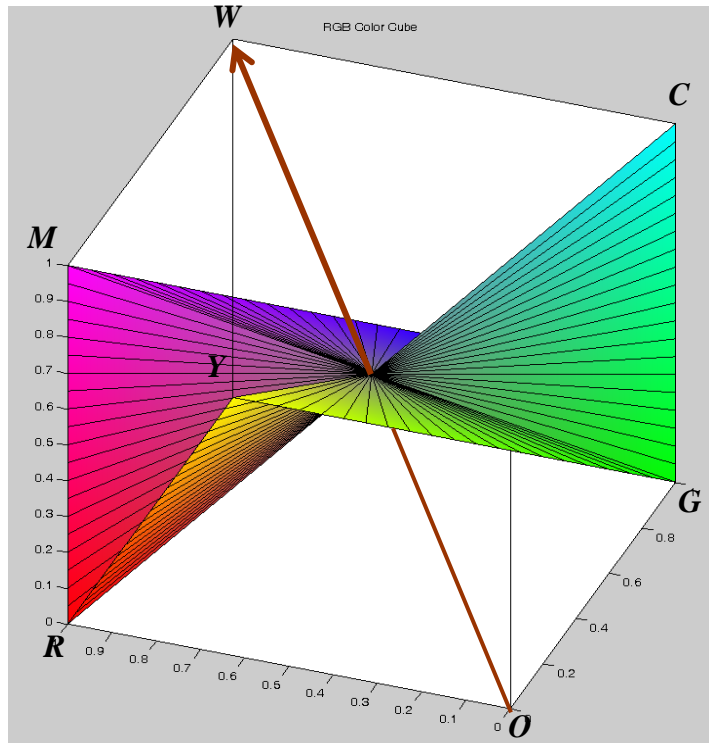


Fig. 12. The value level of 0.5 in *iHSV* color space.

Chapter 4

Color Image Enhancement

Weeks *et al.* [16] mentioned that there is a contradiction between intensity and saturation. In order to enhance the saturation, we can sacrifice a little contrast to improve the saturation.

4.1 The color image enhancement with *eHSI* color model

Along the intensity axis, the central region of the *RGB* cube has the widest saturation expansion range, and if we centralize the intensity in this region, the image will become more saturated. As illustrated in Fig. 13 (a), we observed that the intensity between *P* and *Q* has a wider saturation expansion range. In the general definition, one edge length of the *RGB* cube is 1, and the length of \overline{RW} is equal to the diagonal of one square surface of the *RGB* cube; that is, $|\overline{RW}| = \sqrt{1^2 + 1^2} = \sqrt{2}$, and the length $|\overline{OW}| = \sqrt{2 + 1^2} = \sqrt{3}$. From similar triangles ΔWRP and ΔORP , we have

$$\frac{|\overline{OW}|}{1} = \frac{1}{|\overline{OP}|}. \quad (43)$$

Since $|\overline{OW}| = \sqrt{3}$, $|\overline{OP}| = \frac{1}{\sqrt{3}}$, and $\frac{|\overline{OW}|}{|\overline{OP}|} = 3$. Hence, we conclude that the central 1/3 of the intensity range (*i.e.*, from $|\overline{OW}|/3$ to $2|\overline{OW}|/3$) has a wider saturation expansion range. Moreover, we observe that, in this central range, the attainable maximum saturation range is from *b* to *a*; at the *R* (*or G, B*) or *C* (*or Y, M*) point, the attainable maximum saturation range is from *c* to *a*, where

$$\begin{cases} \frac{a}{1} = \frac{|\overline{WR}|}{|\overline{OW}|} = \frac{\sqrt{2}}{\sqrt{3}} & \Rightarrow a = \frac{\sqrt{2}}{\sqrt{3}} = \frac{4\sqrt{6}}{12} \\ \frac{b}{|\overline{OW}|/2} = \frac{1}{|\overline{WR}|} \Rightarrow \frac{b}{\sqrt{3}/2} = \frac{1}{\sqrt{2}} \Rightarrow b = \frac{\sqrt{3}}{2\sqrt{2}} = \frac{3\sqrt{6}}{12} \\ \frac{c}{|\overline{OW}|/3} = \frac{1}{|\overline{WR}|} \Rightarrow \frac{c}{\sqrt{3}/3} = \frac{1}{\sqrt{2}} \Rightarrow c = \frac{\sqrt{3}}{3\sqrt{2}} = \frac{2\sqrt{6}}{12} \end{cases}. \quad (44)$$

According to the previous analysis, we know that there is a trade-off or conflict between saturation and contrast, that is, some intensity enhancement processes such as histogram equalization or stretching generally expand the value histogram into the entire range as much as possible. Such intensity or value adjustments will make some pixels unsaturated if they have higher or lower values. In contrast, if we centralize the value component in the central value region, the image will be more saturated but the contrast may be reduced. This property is the same as that of the *RGB* cube; that is, the central one third region of the intensity range has a wider attainable maximum saturation range.

In some conditions, we may sacrifice a little contrast to improve the saturation. As illustrated in Fig. 13 (a), the central intensity level in *eHSI* color spaces has the widest attainable maximum saturation range. We can deform the shape of the intensity histogram by moving the intensity mean to the central point (*e.g.*, 128 for 256 gray scales) and then stretching the intensity range on one side of the mean and compressing that on the other side of the mean, then use an *S-type* function to centralize the intensity to the central region. As illustrated in Fig. 13 (b), the *S-type* transformation can be set as

$$f(x) = \begin{cases} 0.5 \left(\frac{x}{0.5} \right)^n, & 0 \leq x \leq 0.5 \\ 1 - 0.5 \left(\frac{1-x}{0.5} \right)^n, & 0.5 < x \leq 1 \end{cases}, \quad (45)$$

where n is a constant. If $n = 0.5$, Eq. (45) can be simplified as

$$f(x) = \begin{cases} \sqrt{0.5x}, & 0 \leq x \leq 0.5 \\ 1 - \sqrt{0.5(1-x)}, & 0.5 < x \leq 1 \end{cases}, \quad (46)$$

After the *S-type* function transformation, the intensity histogram in the *eHSI* color space is concentrated in the central region so that the contrast is slightly reduced but the image is more saturated. Some experiment results will be demonstrated in Section 6.1.

4.2 The color image enhancement with *iHSV* color model

On the other hand, there is a widest attainable maximum saturation range at the central value level of the proposed *iHSV* color space as shown in Fig. 14 (a). If we set the value components in the *iHSV* color space of the image all equal to 0.5, the original fruits image as shown in Fig. 15 (a) will be most saturate but it will have no contrast as shown in Fig. 15 (b). Some color difference details are enhanced, like the red snake-like pattern on the right-bottom corner. This colorful image has less intensity variation and thus suits better for some color segmentation applications. In contrast, if we set the value components in the *HSV* color space of the image all equal to 1.0, the image will also be saturate but the intensity variation will be obvious as shown in Fig. 15 (c).

As illustrated in Fig. 14 (b), we can deform the shape of the intensity histogram by moving the intensity mean to the central point and then stretching the intensity range on one side of the mean and compressing that on the other side of the mean, then use an *S-type* function to centralize the intensity to the central region. After transformation, the contrast is slightly reduced but the image is more saturated. Some experiment results will be demonstrated in Section 6.2.

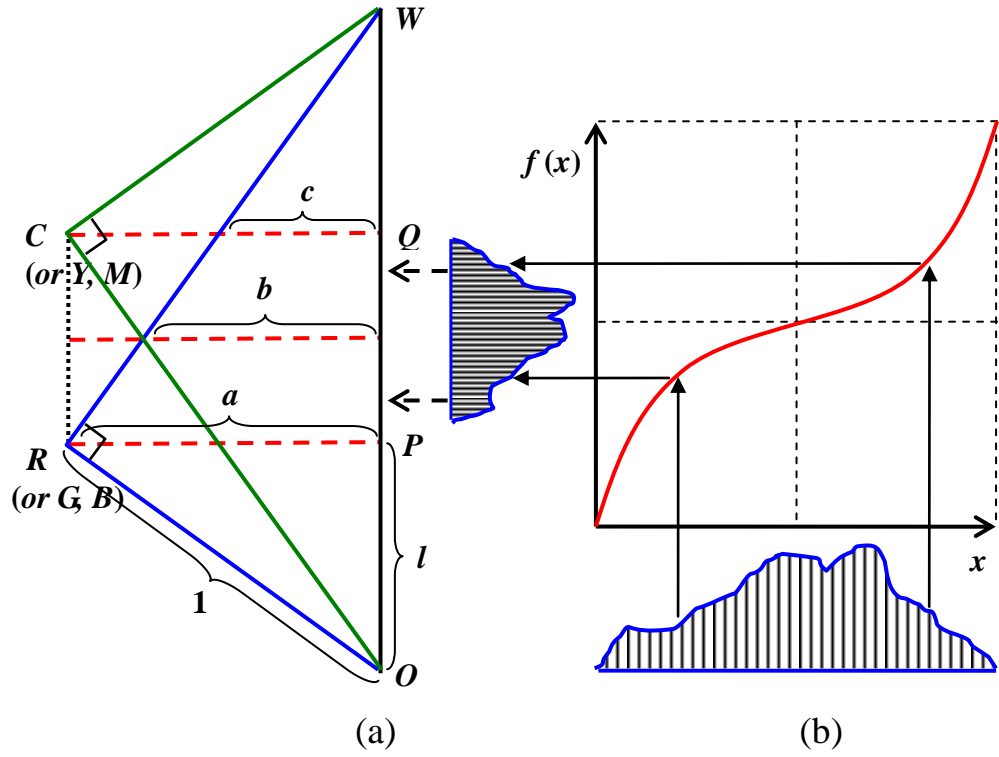


Fig. 13. The saturation is enhanced by using an *S-type* transformation to centralize the intensities to the intensity center area where the attainable maximum saturation range is wider. (a) The side view of the *RGB* cube. (b) The *S-type* transformation.

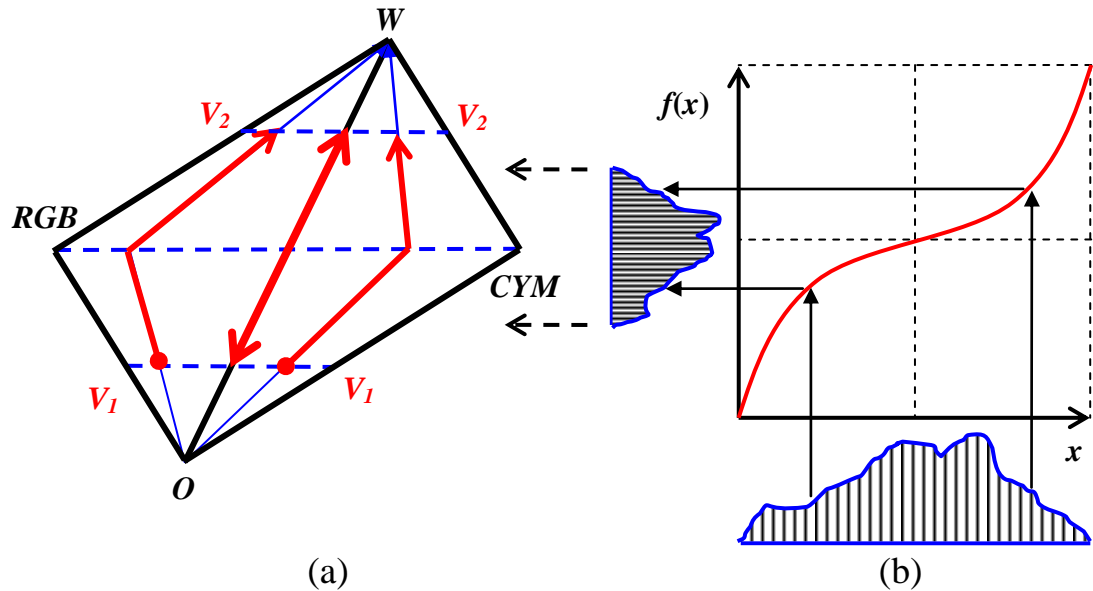


Fig. 14. The saturation enhancement by using the *S-type* function. (a) The side view of *RGB* cube. (b) Using the *S-type* function to centralize the intensity histogram.



(a)



(b)



(c)

Fig. 15. The color map of an image. (a) The original image. (b) The value components of all pixels being changed to 0.5 in *iHSV* color space. (c) The value component of all pixels being changed to 1 in *HSV* color space.

Chapter 5

Cloud Removal Approaches for Aerial Image Visualization

In this chapter, a complete automatic multi-temporal approach is proposed to produce cloud-free and cloud-shadow-free satellite images as shown in Fig. 16. At first, the original images are transformed into our proposed exact *HSI* (*eHSI*) color space and enhanced in both luminance and saturation components. Secondly, the intensity thresholding is used to extract all cloud-cover pixels. The intensity thresholding cannot handle thin clouds and cloud shadow, and often confuses bright land surfaces with clouds. Thus, we utilize a difference comparison method to eliminate unnecessary marking on plain areas or large buildings by checking difference with other *SPOT* images. The morphology opening operator is then used to exclude small bright areas. Subsequently, we choose the base image that has the least thin cloud cover and divide the base image into grid zones. We find the thin-cloud and cloud-shadow zones in the eight neighbors of the thick cloud zones based on the relative locations and the sun elevation angle. At last, the cloud and cloud-shadow zones of the base image are replaced by the same-location cloud-free zones on other images with the pyramid multi-scale fusion method to generate the high-quality cloud-free satellite images.

5.1 Multi-spectral image enhancement

Pseudo *SPOT* images were used for our study. The original *SPOT* images we obtained generally lacked dynamic range. The gray levels were concentrated at the dark end of the gray scale and had a small dynamic range as a low contrast image. Thus, we stretched the intensity of the original images in the range [0, 1]

to enhance the images. The enhancement has two benefits: one is ease of setting the threshold value for cloud detection because the cloud white is almost the maximum value ($RGB = (1, 1, 1)$), and the other is always improving the visual quality of the final results. However, the second process contradicts the first benefit of image enhancement because it will reduce the intensity of cloud areas and the thresholding will result in more errors. Hence the following process should be added to the final results.

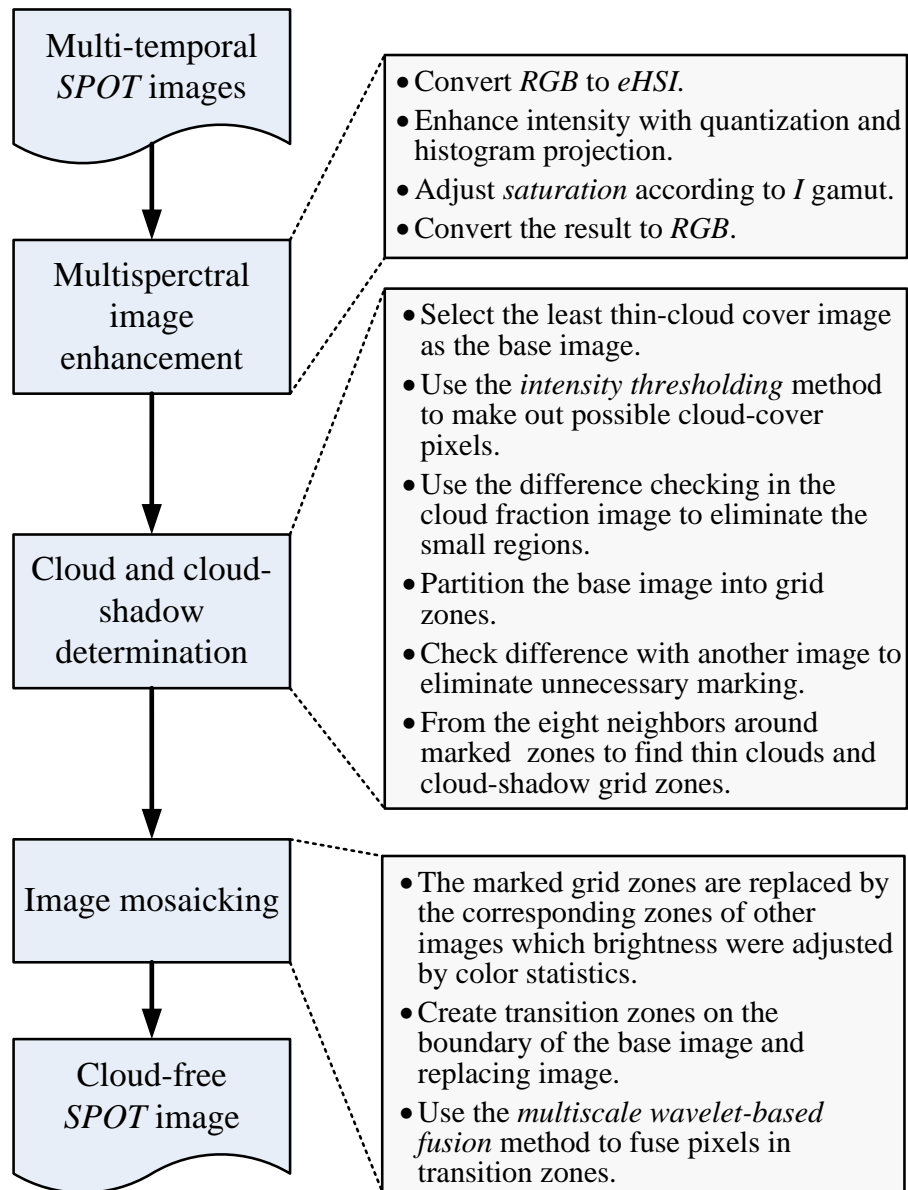


Fig. 16. The diagram of the proposed system for cloud removal.

As examples shown in Fig. 17 (c) and (d), the intensities of the original images shown in Fig. 17 (a) and (b) are linearly stretched and the contrast are enhanced. After transferring the mean of the intensity histogram to the central point and using the *S-type* function to concentrate the intensity to the central region, we get more saturated images as examples shown in Fig. 17 (e) and (f). The saturation is linearly enhanced according to the ratio of the source saturation range to the target saturation range. The oversaturated achromatic region produced by some enhancement methods such as histogram equalization does not appear in the results of the proposed method.

The out of gamut problem contradicts the first benefit of image enhancement; that is, if the saturation component of cloud is not zero, the cloud area is difficult to enhance to the pure white maximum value ($RGB = (1, 1, 1)$). As one example shown in Fig. 18 (a), the cloud areas are still not pure white after intensity histogram stretching or histogram equalization. In order to extract all non-pure white clouds, we must decrease the threshold value from the maximum value and then result in more errors.

The broken tiny cloud areas are not detected and the large smooth reservoir area is misjudged as cloud by the *PWD* method, but the intensity thresholding based on the *eHSI* color model has none of these drawbacks. In practice, the cloud area which is detected by the *PWD* method is smaller than the actual cloud area, but the intensity thresholding method has no such problem. Cloud extraction based on the traditional *HSI* and proposed *eHSI* color models is given in Fig. 18 (c) and (d) for comparison. *eHSI* is significantly superior to traditional *HSI* for cloud extraction. The intensity thresholding based on the proposed *eHSI* color model has satisfactory results and is more efficient than the other methods; thus we use this method as our cloud detection method for the following processes.

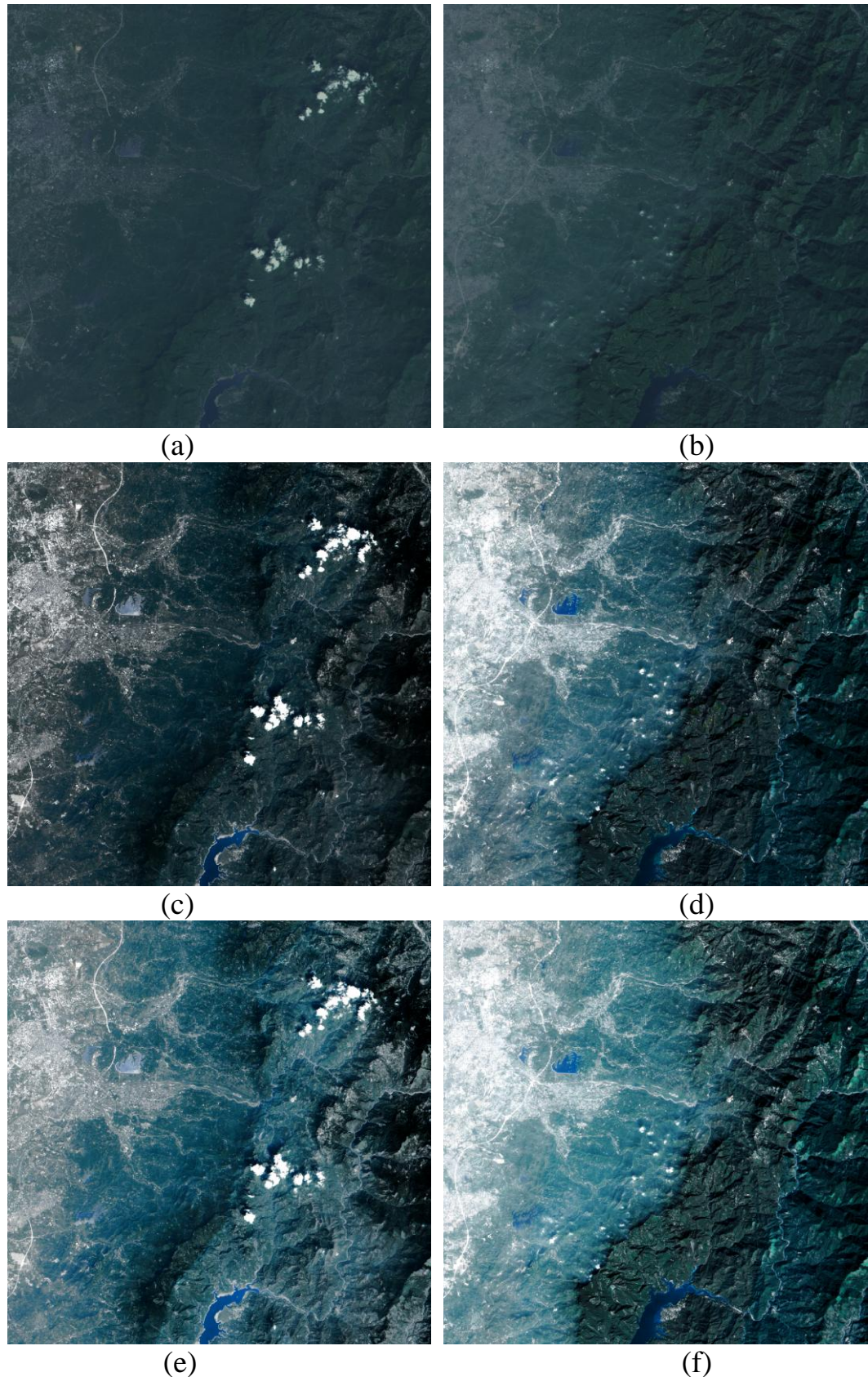


Fig. 17.The enhancement result of a color image. (a) and (b) The original image. (c) and (d) The intensity histogram of original image is linearly stretched. (e) and (f) The intensity histogram is concentrated by an *S-type* function.

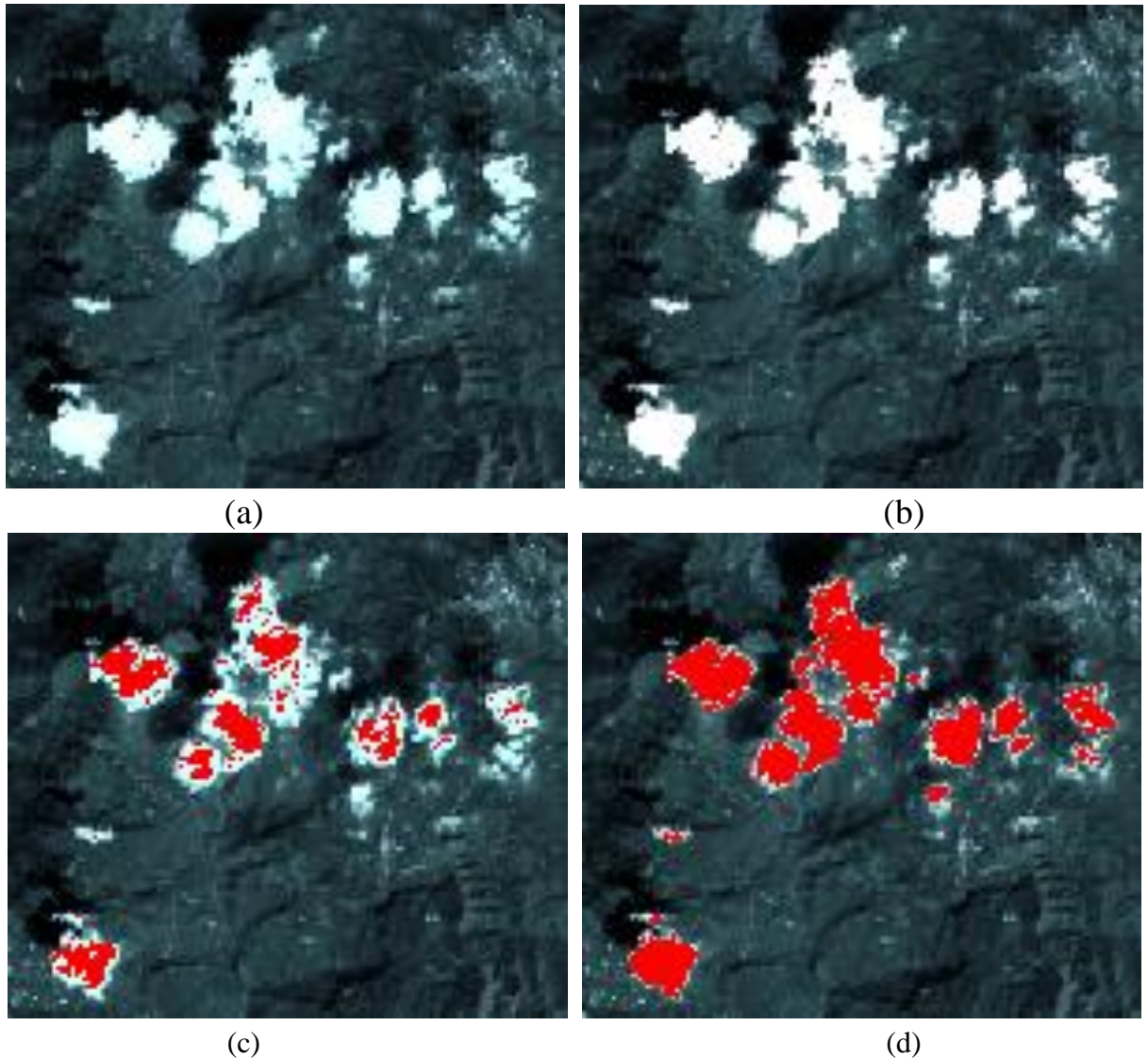


Fig. 18. The saturation variation coincides with the intensity adjustment and the comparison of cloud extraction based on the traditional *HSI* and the proposed *eHSI* color models. (a) The cloud areas enhanced in *HSI* color space, we observed that the cloud areas are not pure white. (b) The cloud areas enhanced in *eHSI* color space, we observed that the cloud areas are pure white. (c) The cloud areas are extracted from the *HSI*-enhanced image. (d) The cloud areas are extracted from the *eHSI*-enhanced image. In all cases, the cloud threshold value is (0.97, 0.97, 0.97).

5.2 Cloud detection

Accurately determining cloud and cloud-shadow regions is one of the key tasks for cloud removal. Several concepts have been used to determine cloud regions. Cloud detection is usually regarded as a bi-level thresholding problem. That is, the original images are transferred to a proper feature domain; then a suitable threshold value is used to separate the pixels into cloud or non-cloud regions. However, the bi-level threshold value is hard to find; moreover, most cases cannot be solved by just one threshold value. For example, the famous Otsu and Kapur methods are not suitable for cloud thresholding, because the distribution of cloud and non-cloud pixels is unbalanced and the methods will produce many errors.

To accurately extract cloud regions, we consider three important factors: (*i*) the color of cloud is white, (*ii*) cloud regions are smooth and flat, and (*iii*) the cloud area has different color and smoothness in two different temporal images. Hence, three kinds of information: gradient, spatial frequency, and color information are utilized to extract cloud regions. We assume the cloud region has low gradient, low spatial frequency, and white color; moreover, the three kinds of information are all different in two different temporal images.

5.2.1 *The gradient-based method*

The cloud region is generally smooth and flat in gray levels. One useful datum to evaluate the smoothness of a region is the gradient. The gradient of an image f is

$$\nabla f = \left(\frac{\partial f}{\partial x}, \frac{\partial f}{\partial y} \right). \quad (47)$$

First, we set a threshold value to delete the high-gradient (magnitude)

portion; we can obtain most cloud regions and several low-gradient areas such as the reservoir area illustrated in Fig. 19 (a). Second, to exclude the fixed smooth areas such as the reservoir area, we check the absolute differences among the same regions on different temporal images. If the differences are not greater than a pre-defined threshold value, we take the region as a non-cloud region. Thus, we use the morphology “and” operation on all low-gradient images to obtain a low-gradient and high-difference image. Finally, we use the morphology “opening” operation to eliminate small fragments as shown in Fig. 19 (b). We superimpose the final results on the corresponding original images to demonstrate the effect of the gradient-based method as examples shown in Fig. 19 (c) and (d).

The method has two drawbacks: (*i*) if the cloud regions are small and broken, the cloud regions are hard to detect as one example shown in Fig. 19 (d), and (*ii*) several non-cloud low-gradient areas are wrong taken as cloud regions. The first drawback comes from the fact that the edge pixels of cloud regions are excluded in the first step because they have a high gradient; hence the boundary of a small smooth area is eroded and then the area disappears in the low-gradient images.

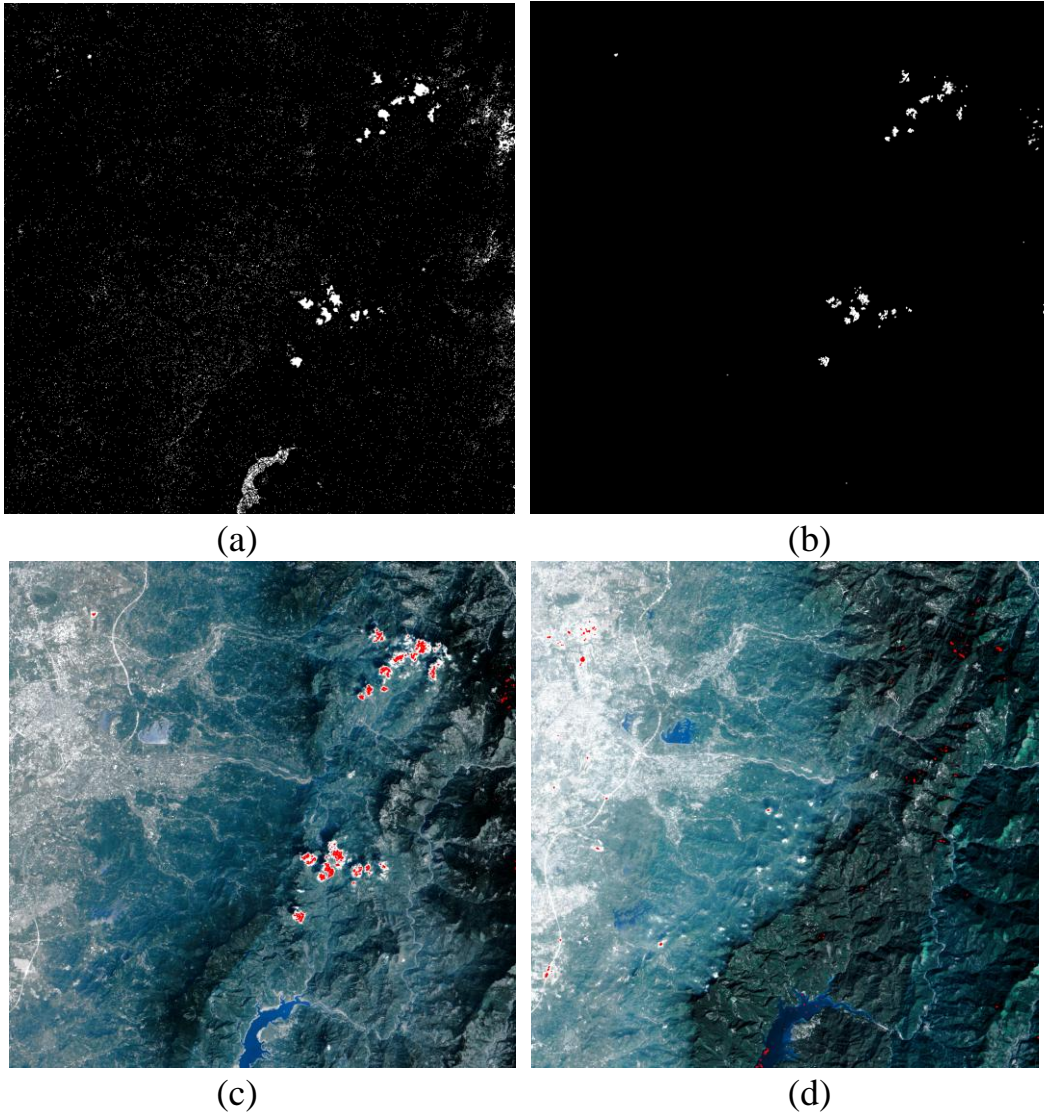


Fig. 19. The gradient-based cloud segmentation. (a) The low-gradient regions after thresholding. (b) Excluding low-difference area from (a) and then eliminating small fragments. (c) Superimpose on one source image. (d) Another segmentation result in which some small broken clouds cannot be detected.

5.2.2 *The spatial-frequency analysis method*

Another measurement for evaluating the smoothness of a local region is the spatial frequency. Several formulas can be used to compute the frequency, such as the short-term Fourier transform (*STFT*), wavelet transform, Wigner distribution, etc. Gabarda and Cristóbal [30] used the Pseudo-Wigner Distribution (*PWD*) method to evaluate the local spatial frequency of cloudy

images. The *PWD* method is pixel-based replacement rather than region-based replacement; thus, the *PWD* method always selects the lowest-distance pixel from one of the different temporal images as the resulted pixel, whether the pixel is in a cloud area or not. If the appearances (*e.g.*, intensity or color) of the different temporal images are similar, this method can get good results. However, if the image appearances are different, this method will select mixed pixels from different temporal images to synthesize a random result.

Moreover, the method cannot tell us whether a pixel is in a cloud area or not. To solve the problem, we can take that if the *PWD* distance of a pixel is smaller than a pre-defined threshold value, we regard it as a cloud pixel. The difference between cloud and reservoir regions is small; thus we always extract most cloud regions, reservoir regions, and some low spatial frequency regions as an example shown in [Fig. 20 \(a\)](#). Next, we check the difference among source images and exclude the low difference portion. Here we can get rid of the reservoir area and some wrong detected areas as shown in [Fig. 20 \(b\)](#). Finally, we use the morphological opening operation to delete small chips. We superimpose the final results on the corresponding source images as shown in [Fig. 20 \(c\) and \(d\)](#).

In the figures, we can find that the thick cloud areas were detected successfully, but the broken thin clouds were not detected. The results come from the row-major 1-D *PWD*. If the small cloud areas are in vertical alignment, their low frequency feature will not be detected. Moreover, the *PWD* method has the “uncertainty principle” problem; that is, the sliding window size must be large enough to maintain the accuracy of frequency evaluation. However, if the window size is much larger than the cloud area, the actual cloud position cannot be detected.

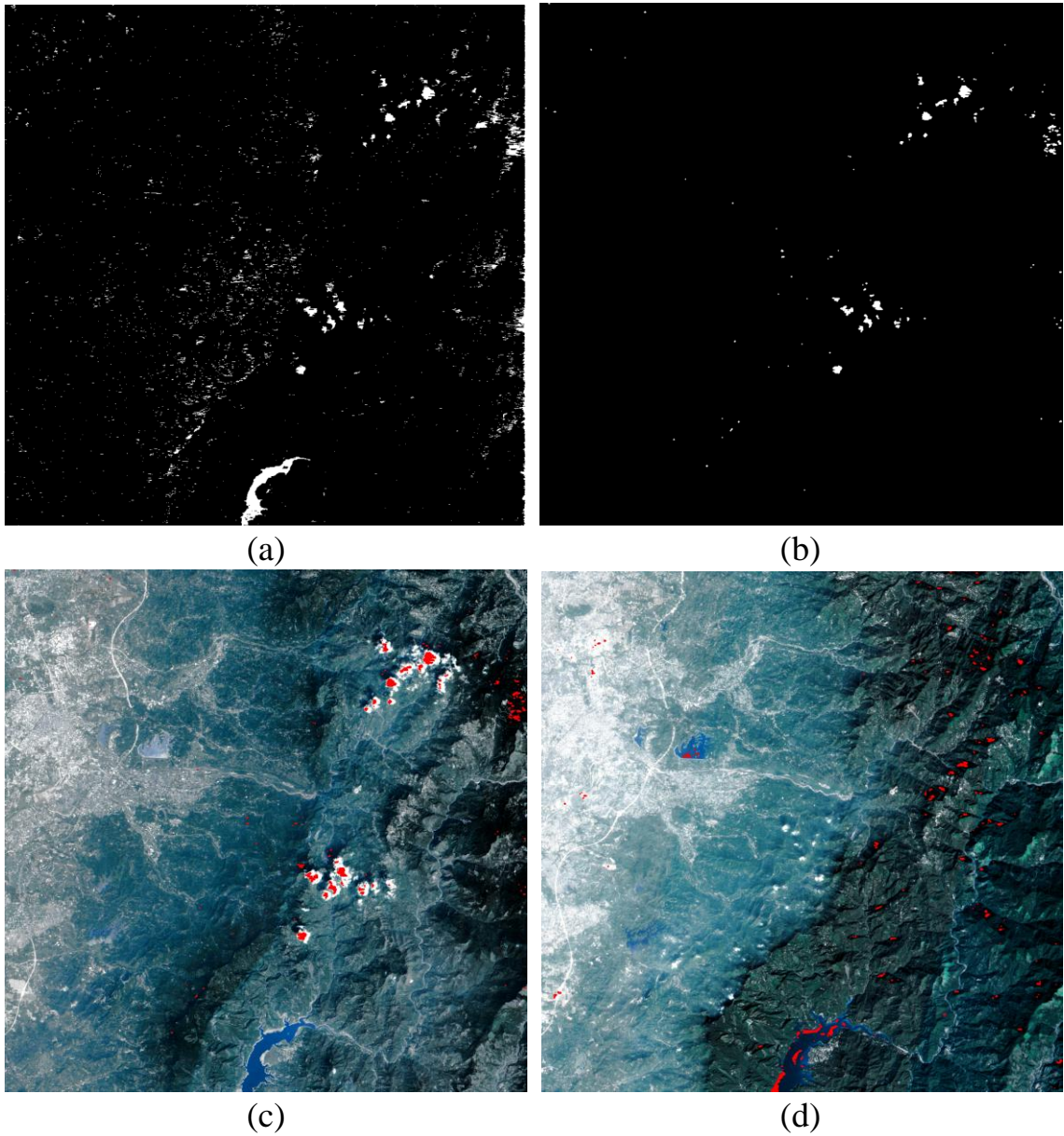


Fig. 20. The frequency-based cloud detection. (a) The low spatial frequency regions. (b) Excluding low difference area from (a) and then eliminating small fragments. (c) Superimpose on one source image. (d) Another case.

5.2.3 Linear spectral unmixing (LSU) method

The original *SPOT* images are with a ground resolution of 12.5 meters, which is large enough to contain various cover types; that is, the information in a pixel may contain various materials and the pixel is called a mixed pixel as examples shown in Fig. 21. The marked region represented a pixel in a SPOT image, which is composed of 40% soil, 20% wood and 40% road. For mixed pixels, a more sensible approach is to construct a mixture map in which a series of maps give the concentration of each ground-cover class. In such a map, the contribution of each pixel is assigned in proportion to the percentage area of each ground cover class occupying in the mixed pixel. This process of assigning more than one class label to an individual mixed pixel is called spectral unmixing. The map that uses the intensity to represent the percentage of the ground cover class in each pixel is called a fraction image.

Linear mixing model is a popular mixing model. According to the assumption of this model, a mixed pixel is linearly consisted of different materials. The unmixing process of the model is to solve a system of linear equations based on a least-square-error criterion. It can only be used to unmixing pixels when the number of bands is greater than the number of component materials. The linear spectral unmixing (LSU) method [41] was generally used to solve the mixed pixel problem and generate a fraction image for each ground cover class based on a least-square-error criterion of a linear system. The basic assumption of linear mixing model is the signal received from each pixel can be considered as a linear superposition of the spectral contributions of all pixel components.

In our previous study [36], we used multiple spectral data to unmix the material components, and then to extract the cloud pixels. However, the method can only be used to unmix pixels when the number of bands is greater than the number of component materials. Thus, the *LSU* method is excellent for

hyper-spectral images, but is weak for fewer-spectral (multi-spectral) images [41]. We have only *RGB* pseudo-color data; there is no enough spectral information to uniquely describe the cloud material. Thus, partial non-cloud pixels were also regarded as the cloud pixels as examples shown in Fig. 22.

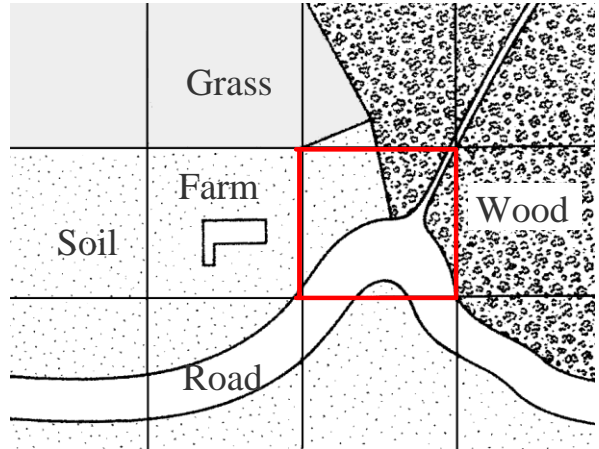


Fig. 21. Examples of mixed pixels.

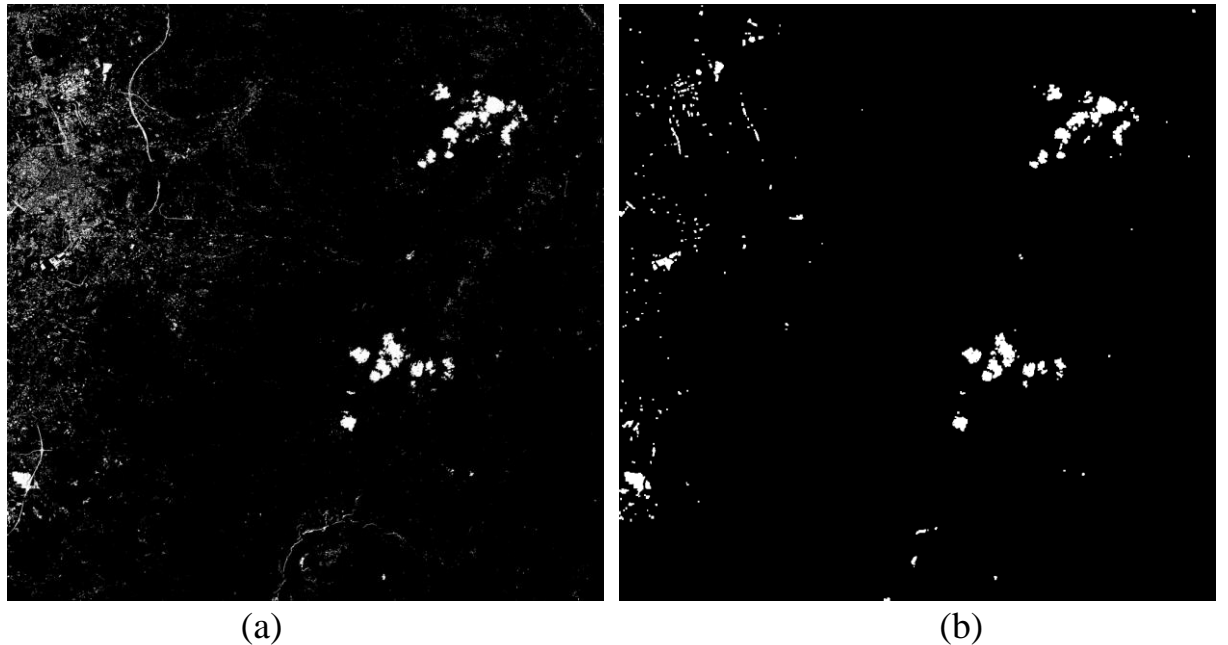


Fig. 22. The cloud segmentation result based on the *LSU* method. (a) The cloud areas detected by *LSU* method. (b) The cloud areas in (a) are processed by opening operator.

5.2.4 The color-based method

Instead of evaluating the smoothness, the third measurement uses color to judge the cloud or non-cloud pixels. Unlike the gradient and spatial-frequency analysis methods, which both tend to erroneously detect some smooth but non-cloud regions such as reservoir area, the color-based method tends to detect the near-white regions.

Actually, the intensity of white color is maximum in the *RGB* cube ($RGB = (1, 1, 1)$); we can use the intensity thresholding method instead of the *LSU* method to find the cloud pixels. We set a threshold value near the maximum intensity value (e.g., 0.95) to obtain an acceptable result as shown in Fig. 23 (a), based on the proposed *eHSI* color model [42]. The method still has a few errors, like the *LSU* method, if an image has high intensity non-cloud pixels. To solve the problem, we check the intensity difference among the different temporal images; if the difference in some detected cloud regions is low, we take the region as a non-cloud region. We use the “and” operation to extract the high intensity and high difference areas, and then use the “opening” operation to eliminate most tiny and broken regions as shown in Fig. 23 (b). Finally, we superimpose the final results on the corresponding original images as shown in Fig. 23 (c) and (d). Note that many broken tiny cloud areas are correctly detected as shown in Fig. 23 (d), and some high-intensity non-cloud areas are correctly excluded as the yellow circles shown in Fig. 23 (c) and (d).

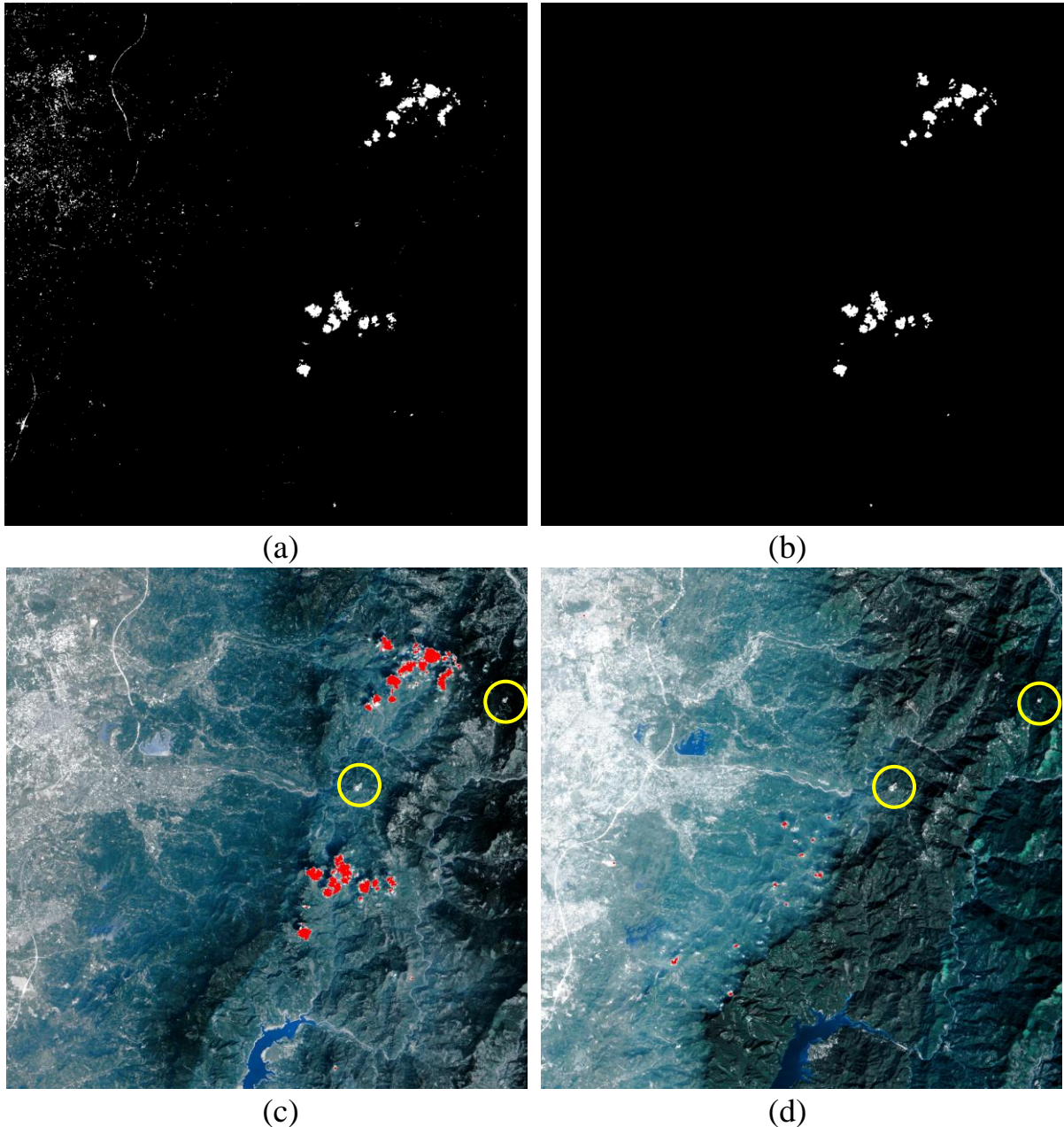


Fig. 23. The intensity thresholding-based cloud detection. (a) The high intensity areas. (b) Eliminating the low difference areas from (a) and then eliminating the small fragments. (c) Superimposing on the source image. (d) Another case.

5.3 Image fusion

The cloud and cloud-shadow regions in the base image are clipped out and replaced by same-location regions from the other temporal images. Mostly, the seams will appear in the adjacent areas between the base and the replacing regions. Image fusion is a process to make the seam invisible. The basic idea is that the appearance in the adjacent zones is fused across their boundaries. We create a multi-resolution weighting mask for image fusion. The mask will process a region comprising two adjacent zones; one is on the base image and the other is on the replacing image. Then the adjacent zones are fused into a final zone as smoothly as possible. The fusion steps consist of color matching and pyramid multi-scale fusion.

5.3.1 Determining the augmented zone

To handle the fragmentary cloud regions that surround the detected cloud areas, we segment the base image into 32×32 -pixel zones. If the number of cloud pixels in one zone is greater than five, we mark the grid as a cloud zone and the zone will be totally replaced by the same zone in the replacing image. As one example shown in Fig. 24 (a), the black zones are marked as the cloud zones.

On the other hand, to remove the cloud shadow areas and the thin cloud areas which appear beside the detected thick cloud areas, we create augmented zones to enclose the possible cloud areas. The augmented zones are determined by the eight-neighbor grid zones around the detected cloud zones. The contour bands composed of augmented zones for the cloud zones are then generated as the gray zones shown in Fig. 24 (a). However, if an augmented zone in the replacing image has more than five cloud pixels, we don't include the augmented zone in the contour band as the yellow circle shown in Fig. 24 (a).

5.3.2 Color uniformity

In general, the multiple temporal images have different brightness due to the atmospheric effects, sun angles, and sensor viewing angles as examples shown in Fig. 17 (a) and (b). Here we use the color of the replaced region in the base image to modify the color of the corresponding region in the replacing image based on the *laβ* color model [43, 44]. At first, we transform the *RGB* values to *laβ*, and then compute the color means and standard deviations of the replaced and replacing regions, respectively. The replacing colors (l_r, α_r, β_r) are modified by scaling and offsetting according to the color means and standard deviations of the replaced and replacing regions to ($l'_r, \alpha'_r, \beta'_r$),

$$\begin{cases} l'_r = (l_r - \bar{l}_r) \frac{\sigma_b^l}{\sigma_r^l} + \bar{l}_b \\ \alpha'_r = (\alpha_r - \bar{\alpha}_r) \frac{\sigma_b^\alpha}{\sigma_r^\alpha} + \bar{\alpha}_b, \\ \beta'_r = (\beta_r - \bar{\beta}_r) \frac{\sigma_b^\beta}{\sigma_r^\beta} + \bar{\beta}_b \end{cases} \quad (48)$$

where $(\bar{l}_b, \bar{\alpha}_b, \bar{\beta}_b)$ and $(\bar{l}_r, \bar{\alpha}_r, \bar{\beta}_r)$ are the mean color vectors of the replaced and replacing regions, respectively; $(\sigma_b^l, \sigma_b^\alpha, \sigma_b^\beta)$ and $(\sigma_r^l, \sigma_r^\alpha, \sigma_r^\beta)$ are the standard deviations of the color vectors of the replaced and replacing regions, respectively.

The modification makes the color of the replacing region more similar to the replaced region as examples shown in Fig. 24 (b). However, the replaced result generally has a few visible boundaries as shown in Fig. 24 (b); these boundaries will be further removed by the following fusion process.

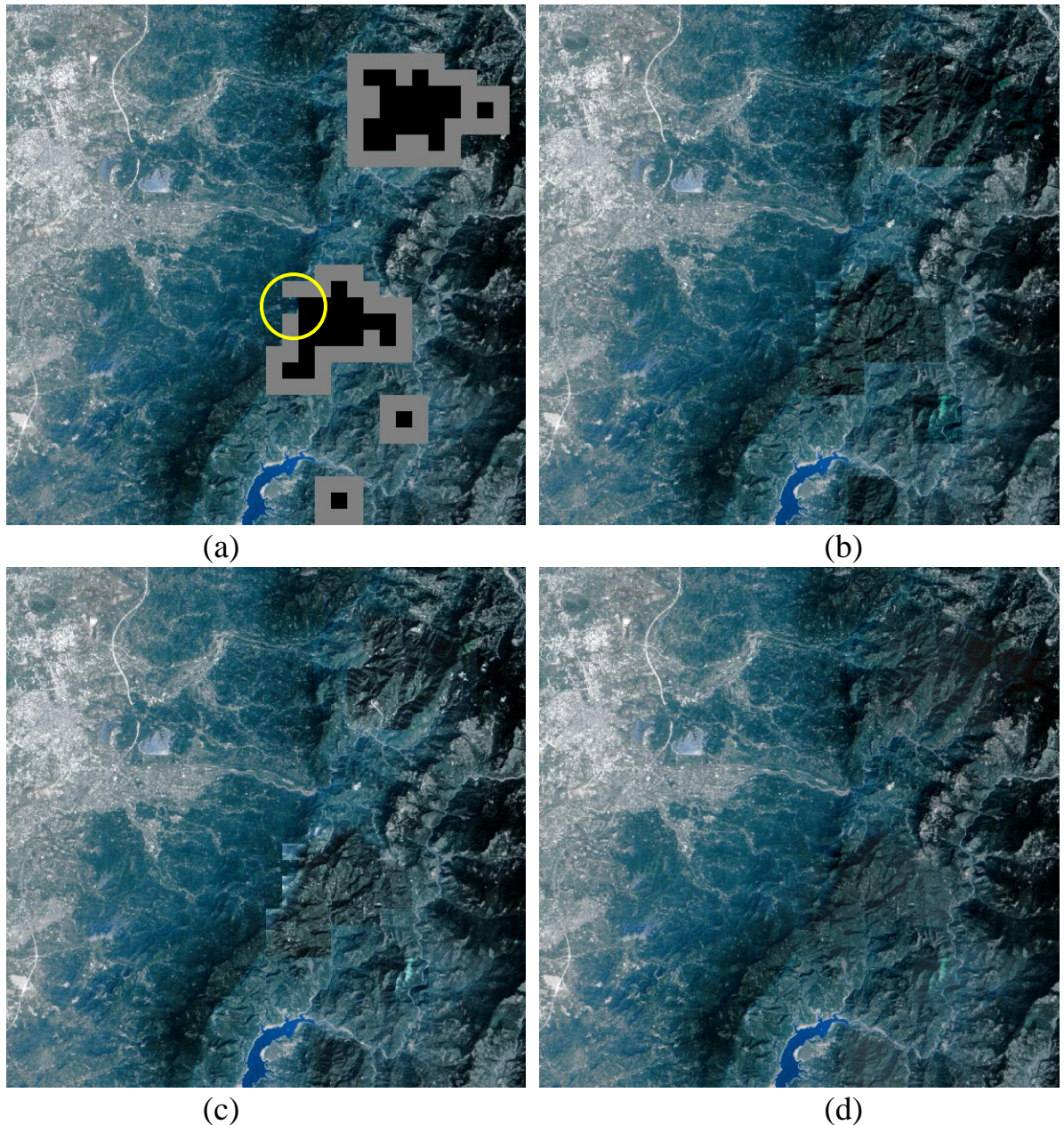


Fig. 24. The cloud zones and augmentative zones. (a) Original base image and the cloud detected zones and the augmentative zones are clipped. (b) The clipped zones are patched with the same areas in another replacing image. (c) Replacement with the color corrected image. (d) The multi-scale image fusion result.

5.3.3 Multi-scale fusion

The pyramid multi-scale fusion method [37] is more efficient than a wavelet-based fusion method [36] for our purpose; thus the pyramid multi-scale based method is used to fuse images. At first, both images are decomposed into N different resolution images (Gaussian pyramid), and the residual images (Laplacian pyramid) are obtained from the difference between every two contiguous-resolution images,

$$L_l = G_l - EXPAND[G_{l+1}], \quad (49)$$

where G_l is the l -th level of the Gaussian pyramid, L_l is the l -th level of the Laplacian pyramid, and

$$EXPAND[G_{l+1}] = G'_l(i, j) = \frac{1}{\alpha(i, j)} \sum_{m=-2}^2 \sum_{n=-2}^2 G_{l+1}\left(\frac{i+m}{2}, \frac{j+n}{2}\right), \quad (50)$$

$$\text{where } \alpha(i, j) = \begin{cases} 4, & \text{if both } i \text{ and } j \text{ are odd,} \\ 6, & \text{if one of } i \text{ and } j \text{ is odd and the other is even,} \\ 9, & \text{if both } i \text{ and } j \text{ are even.} \end{cases}$$

In Eq. (50), only integer $(i+m)/2$ or $(j+n)/2$ is included in the summation term. The pyramid multi-scale fusion method is described as follows:

- Step 1.* Create two Laplacian pyramids for the base and replacing images, respectively.
- Step 2.* Create a pyramid of weighting masks which is the Gaussian pyramid of the detected cloud regions.
- Step 3.* Fuse the corresponding levels of the Laplacian pyramids of the two images with the corresponding weighting mask. For each level l and pixel (i, j)

$$LS_l(i, j) = w_l(i, j) LB_l(i, j) + [1 - w_l(i, j)] LR_l(i, j), \quad (51)$$

where LS_l , LB_l , and LR_l are the l th-level Laplacian pyramids of the fused, base, and replacing images, respectively, and w_l is the l th-level weighting mask.

- Step 4.* Repeatedly construct the finer Gaussian pyramid GS_l from the fused LS_l and the coarser-level GS_{l+1} ,

$$GS_l = LS_l + EXPAND[GS_{l+1}], \quad (52)$$

until the fused image GS_0 is obtained, where $GS_N = LS_N$.

The final Laplacian image is equal to the final lowest resolution Gaussian image, and at the recovering process, the Gaussian pyramid no more required as Fig. 25 illustrated.

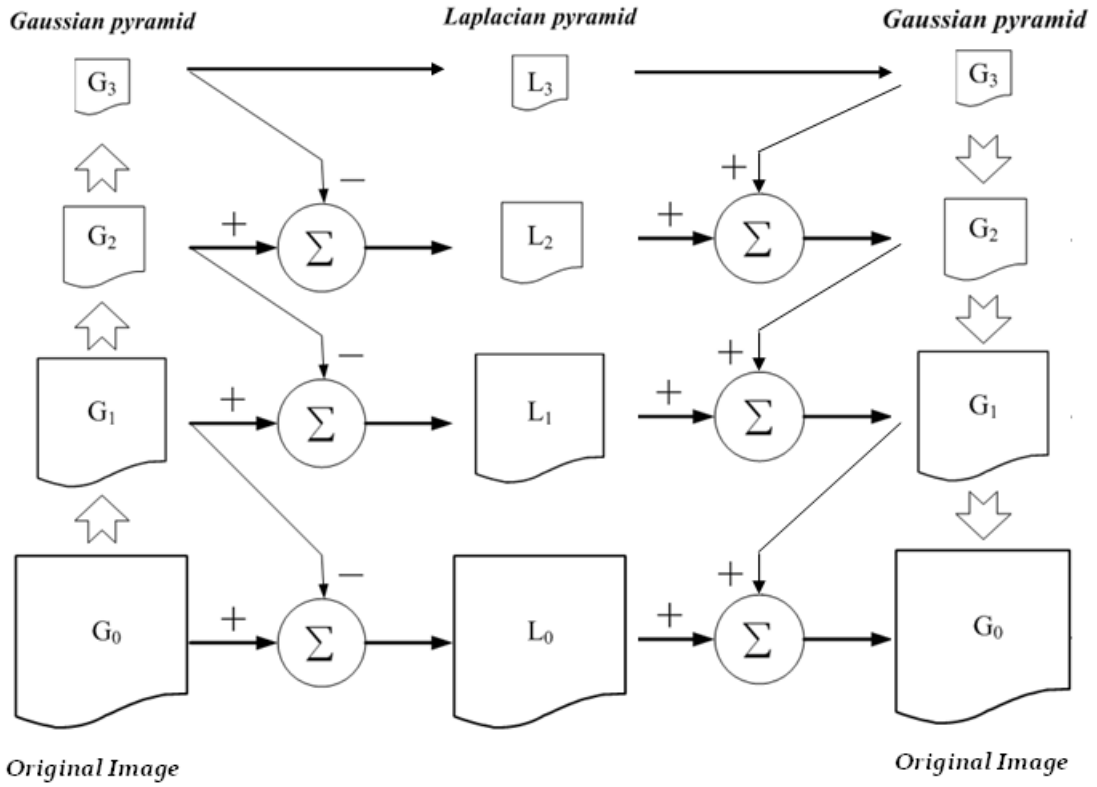
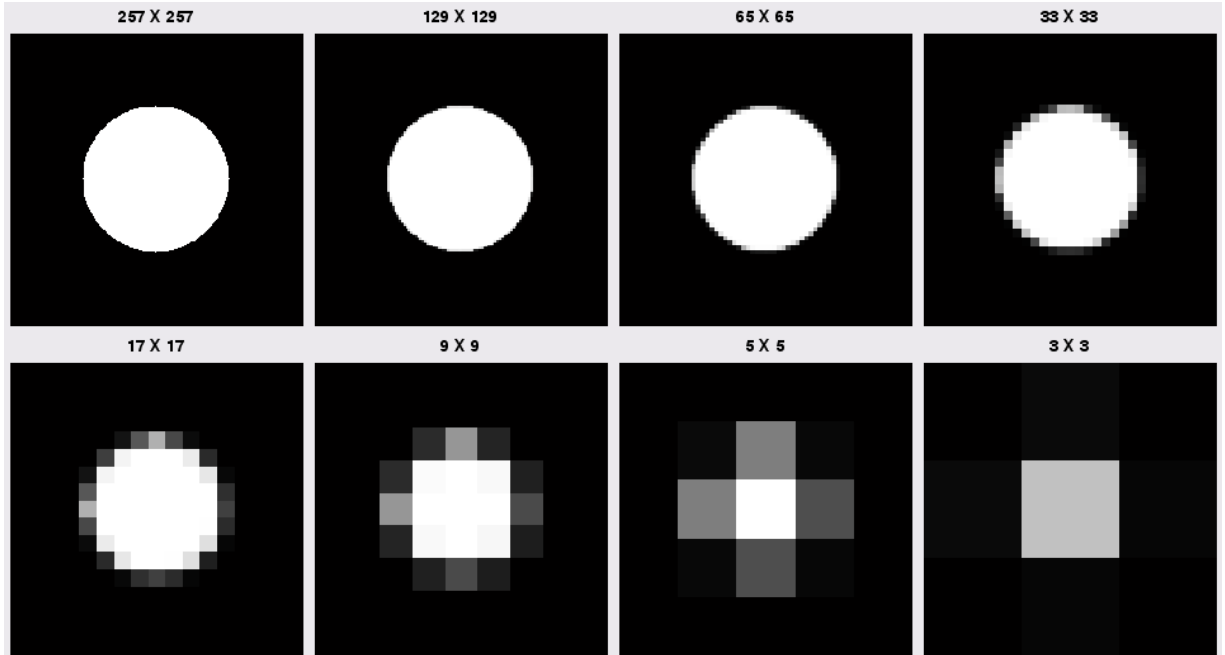


Fig. 25. The decomposition and re-combination procedure of Gaussian pyramid and Laplacian pyramid.

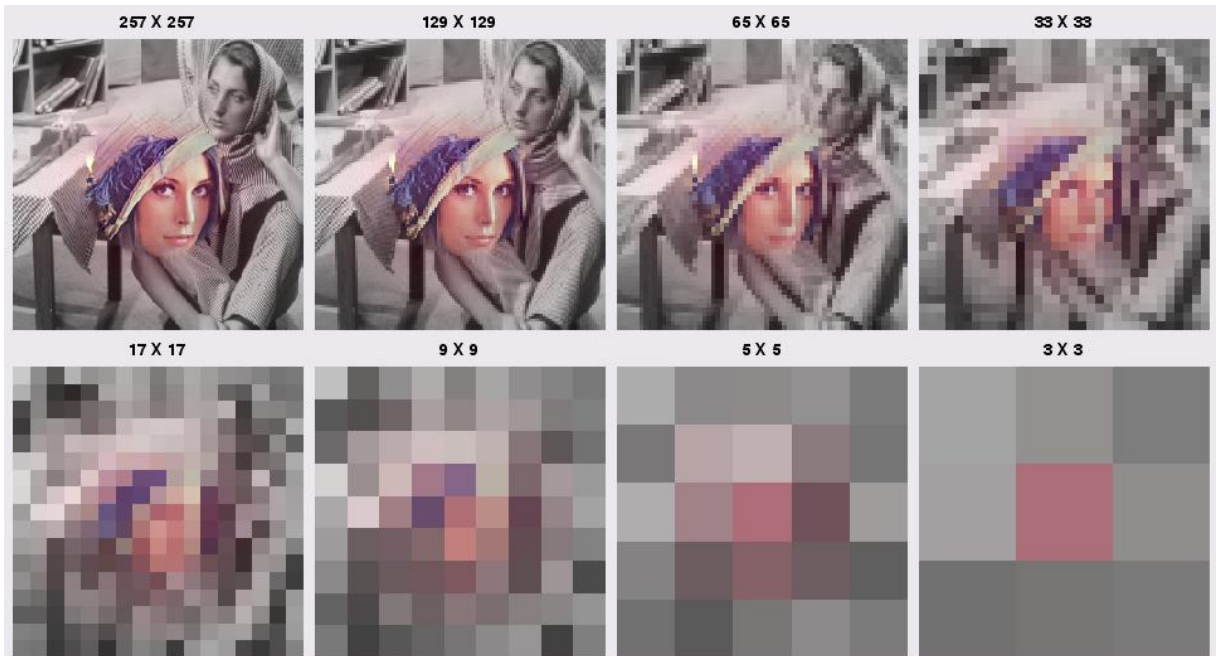
One example of the multi-scale fusion method is shown in Fig. 26, where we fuse the central region of Lena image into the central region of the Barbara image. The original Lena image can be divided into eight different resolution images by *Gaussian* smoothing and down sampling. These images constitute a *Gaussian* pyramid. The Barbara image can be also divided into eight level of *Gaussian* and *Laplacian* pyramid as previous stated. In order to melt the central region of Lena image into the central region of Barbara image, we create a circle mask whose radius is equal to 128 pixels and located at the central position. Besides, we created its multi-resolution *Gaussian* pyramid as Fig. 26 (a) illustrated. The created multi-resolution masks can be regarded as the fusion weight of replacing image, and its complementary part can be regarded as the fusion weight of base image. It should be note that the *Gaussian* pyramid of mask image and the *Laplacian* pyramid of source images are participated in final recovery operation.

As illustrated in Fig. 26 (b), the lowest *Laplacian* pyramid of Lena was multiplied by the lowest *Gaussian* pyramid of mask image, and the lowest *Laplacian* pyramid of Barbara was multiplied by the complement of lowest *Gaussian* pyramid of mask image. After that, the two results were added together. The next step is to up-sampling it and adds the next level weighted residual image. Finally, we can obtain a fused image and the boundary between the two different images was melted.

We use the multi-scale fusion technique to fuse the remote-sensing images. The fusion mask is the cloud zone as one example shown in Fig. 23 (d). The mosaicing result by using our previous cloud segmentation grid has very good appearance and the color difference in the result of previous section is disappeared.



(a)



(b)

Fig. 26. Multiscale image fusion. (a) The Gaussian pyramid of mask image (b) The fusion process at different level of resolution.

Chapter 6

Experiments and Discussions

Five color models: *HSI*, *eHSI*, *HSV*, *iHSV*, and *CIELAB* and two enhancement methods: histogram equalization and *S-type* transformation were compared for color image enhancement quality. On the other hand, Another cloud removal case was demonstrated

6.1 Color image enhancement with *eHSI* color model

If an image is high bright, the intensity of most pixels is reduced after intensity histogram equalization. According to the previous analysis, the saturation will be also reduced in the *HSI* color space. As illustrated in Fig. 27, the contrast of the Tiffany image is enhanced, but the saturation is deteriorated after intensity histogram equalization in the *HSI* color space, as shown in Fig 27 (b). The similar result was obtained as shown in Fig. 27 (d), where *L* histogram of the *CIELAB* color model is equalized. Contrarily, the contrast and saturation are enhanced, as shown in Fig. 27 (f), where intensity histogram of *eHSI* model was equalized. If the *S-type* transformation instead of the histogram equalization is applied on the intensity histogram of *HSI*, *CIELAB*, and *eHSI* models, we also get the similar results as shown in Fig. 27 (c), (e), and (g), respectively. The saturation in *HSI* and *CIELAB* models is not adapted to the attainable maximum saturation range; as shown in Fig. 27 (c) and (e). However, with the *eHSI* model, the contrast is slightly reduced, but the color is more saturated, as shown in Fig. 27 (g).

We used a cosmetic image to conduct another experiment as shown in Figs. 28 and 29. We artificially brightened and darkened the original cosmetic image to evaluate the enhancement effect, respectively. With the traditional *HSI* model, the brightened image becomes less saturated after intensity histogram

equalization and the *S-type* transformation as illustrated in Fig. 28 (c) and (d), respectively. With the *CIELAB* model, the saturation is slight reduced after *L* histogram is equalized and processed by the *S-type* transformation as shown in Fig. 28 (e) and (f), respectively. With the *eHSI* model, the saturation of the brightened image is further enhanced after intensity histogram is equalized and processed by the *S-type* transformation as illustrated in Fig. 28 (g) and (h), respectively.

On the other hand, the darkened cosmetic image becomes oversaturated after the intensity histogram is equalized and centralized by the *S-type* transformation as illustrated in Fig. 29 (b) and (c), respectively. In the results, the out-of-gamut problem limits the increase in intensity so that intensity does not reach the desired value (*e.g.*, the white color panel) and the contrast is limited (*e.g.*, the texture of red color panel). With the *CIELAB* model, the contrast is enhanced but saturation is unchanged after *L* histogram is equalized and centralized by the *S-type* transformation as shown in Fig. 29 (d) and (e), respectively. Contrarily, there are no out-of-gamut and oversaturation problems with the same enhancements on the *eHSI* model as shown in Fig. 29 (f) and (g), respectively; moreover, intensity and contrast can reach the desired levels.

Here, we conclude that the intensity enhancement of high-saturated images in the *eHSI* space is better than that in the traditional *HSI* space. Furthermore, reducing intensity of a high-intensity image in the *eHSI* space will always produce a better enhancement result than in the *HSI* space.



Fig. 27. The enhanced results of Tiffany image. (a) The original image. (b) (c) (d) Intensity histogram is equalized in HSI , $CIELAB$, and $eHSI$ spaces, respectively. (e) (f) (g) Intensity histogram is centralized by S -type transformation in HSI , $CIELAB$, and $eHSI$ spaces, respectively.

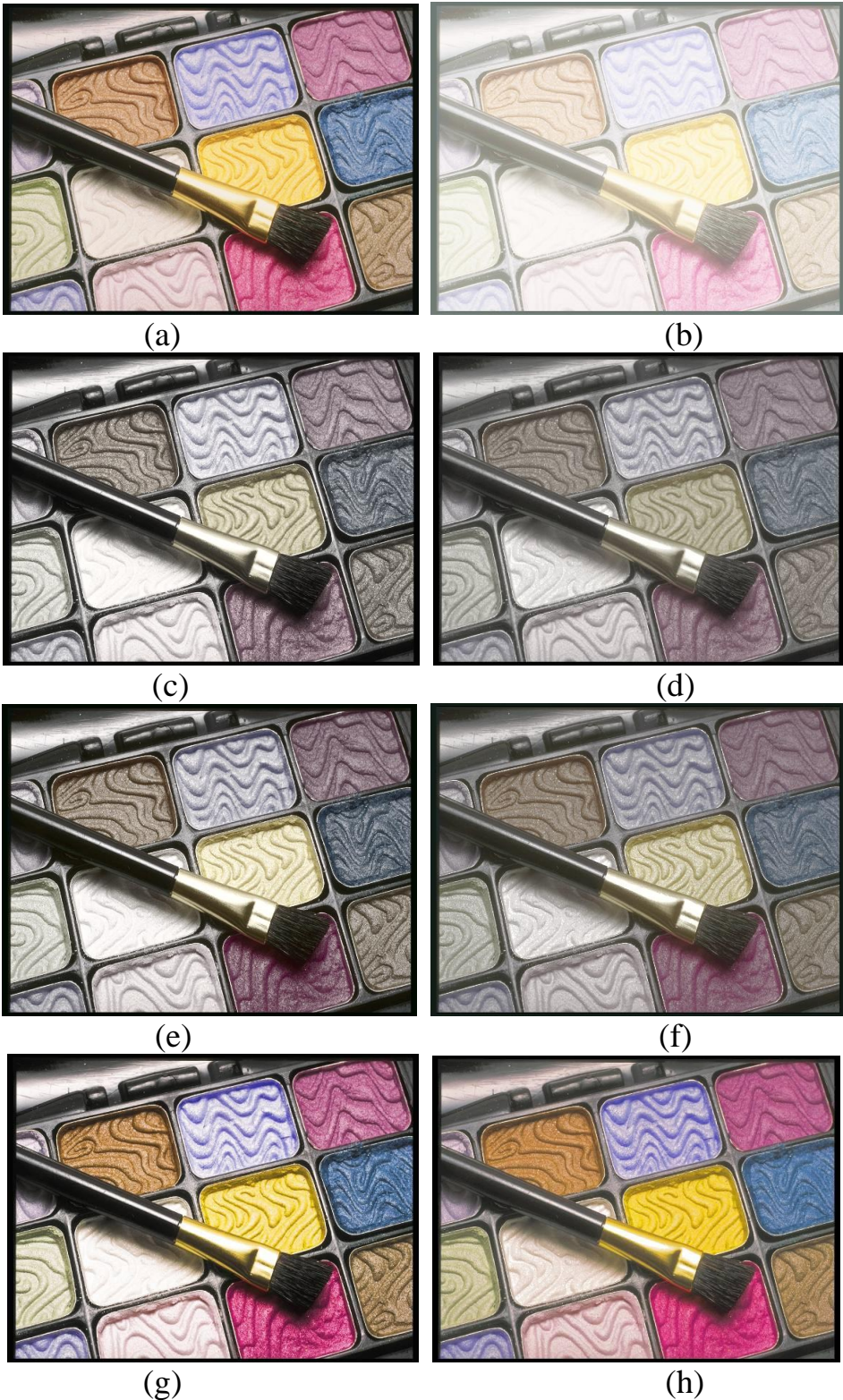


Fig. 28. The enhanced results of the brightened cosmetic image. (a) The original image. (b) The brightened image. (c) (e) (g) Intensity histogram is equalized in *HSI*, *CIELAB*, and *eHSI* spaces, respectively. (d) (f) (h) Intensity histogram is centralized by *S*-type transformation in *HSI*, *CIELAB*, and *eHSI* spaces, respectively.

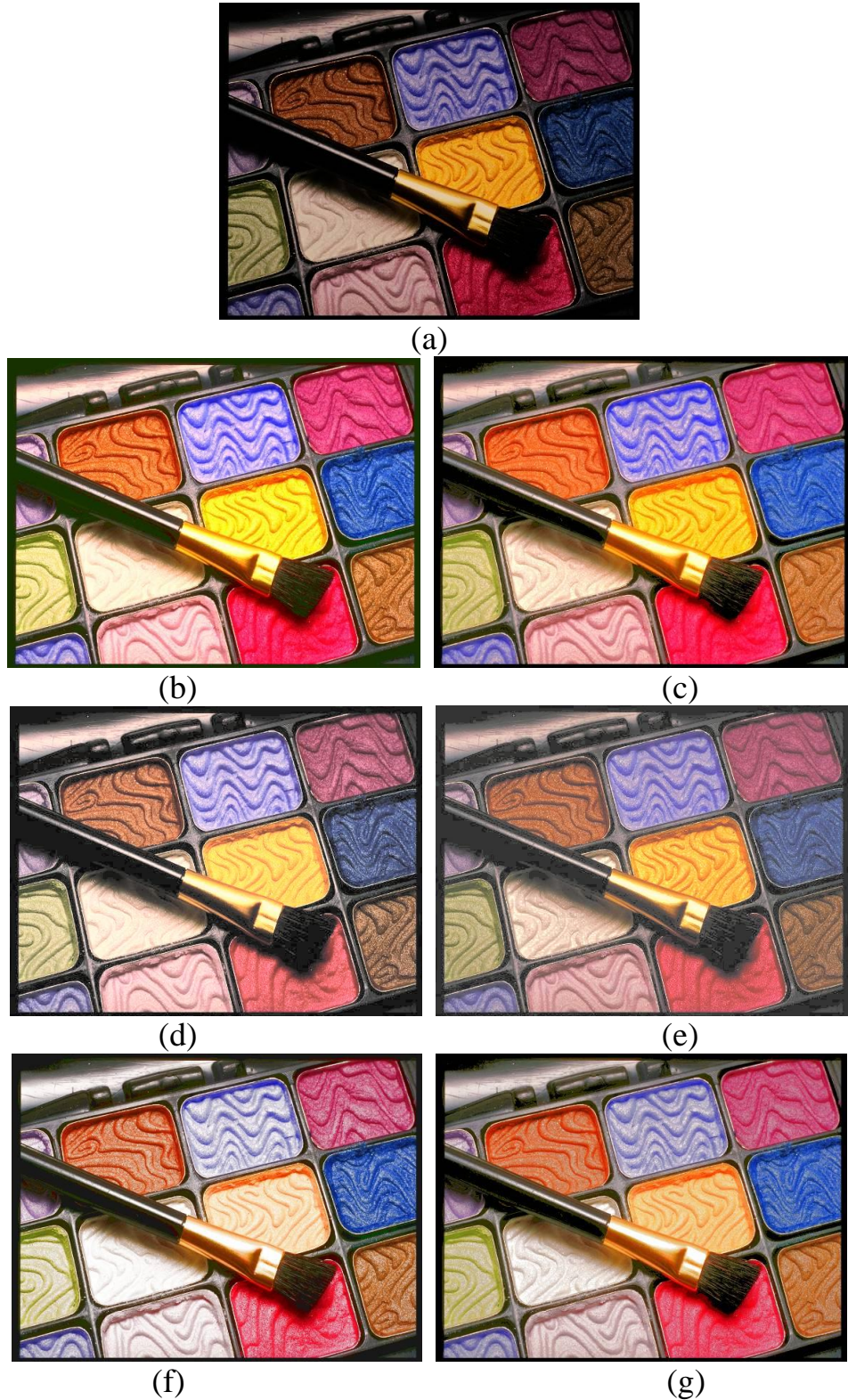


Fig. 29. The enhanced results of the darkened cosmetic image. (a) The darkened image. (b) (d) (f) Intensity histogram is equalized in HSI , $CIELAB$, and $eHSI$ spaces, respectively. (c) (e) (g) Intensity histogram is centralized by S -type transformation in HSI , $CIELAB$, and $eHSI$ spaces, respectively.

6.2 Color image enhancement with *iHSV* color model

The defects of the traditional *HSV* color space are apparent for bright and saturate images because the bright and saturated pixels are all accumulated in the high value region of the value histogram. Let's take the Tiffany image ([Fig. 30 \(a\)](#)) as an example. Its intensity histogram is shown in [Fig. 31 \(a\)](#). For comparison purpose, the intensity is calculated by $(R+G+B) / 3$, thus independent of the *HSV* and *iHSV* color spaces. As described in [Chapter 3](#), after the *HSV* color space transformation, most pixels' values are concentrated in the higher value region and the Gaussian distribution of value histogram is distorted as shown in [Fig. 31 \(b\)](#) due to more accumulation of value histogram at the high value and saturation level. In contrast, the value histogram in the *iHSV* color space is similar to and matched with the original intensity histogram as shown in [Fig. 31 \(c\)](#).

After value histogram equalization in the *HSV* color space, the dominant higher value bin expels all other bins to the low value region as illustrated in [Fig. 31 \(d\)](#). The processed image is darker and unsaturated because most of the pixels' values are reduced and transferred to the low value region and the saturation in the *HSV* color space is simultaneously decreased with the decreased value component. Furthermore, many black speckles appear in the final result as shown in [Fig. 30 \(b\)](#). On the other hand, the equalized histogram in the proposed *iHSV* color space is more uniform as shown in [Fig. 31 \(e\)](#) and the final result is brighter and more saturate as shown in [Fig. 31 \(c\)](#).

We observed that there is a contradiction between contrast and saturation. That is because the higher and lower intensity regions have narrower attainable maximum saturation ranges. In order to improve the saturation of the contrast-enhanced images, we sacrificed a little contrast to concentrate the value histogram in the central region which has a wider attainable maximum saturation range. In the proposed *iHSV* color space, the saturation component is

automatically and linearly tuned according to the target attainable maximum saturation range of different values, hence the correlation between the value and saturation components is preserved and additional saturation enhancement procedure is not necessary. After value histogram centralization with the *S-type* function, the contrast of the enhanced image is mildly reduced but the saturation is increased as shown in Fig. 30 (e). On the other hand, the saturation is not enhanced with the *S-type* function in the traditional *HSV* color space as shown in Fig. 30 (d) because the saturation is always decreased simultaneously with the decreased value component no matter the attainable maximum saturation range of the target is wider or narrower.

Another experiment is shown in Fig. 32. After value histogram equalization in the *iHSV* color space, the contrast of the original car image shown in Fig. 32 (a) is enhanced as shown in Fig. 32 (c). In contrast, the enhanced image whose value histogram is equalized in the *HSV* color space is not satisfying and has many speckle noises as shown in Fig. 32 (b). The value histogram shown in Fig. 33 (b) is different from the original intensity histogram (Fig. 33 (a)) and concentrated in the high value region. On the other hand, the value histogram in the *iHSV* color space is similar to the original intensity histogram as shown in Fig. 33 (c). After value histogram equalization, four dominant high value bins in the value histogram of the *HSV* color space exclude the remaining bins from the high value region as shown in Fig. 33 (d). That is why the speckle noises appeared in the uniform blue sky. In contrast, the equalized value histogram in the *iHSV* color space is quite uniform as shown in Fig. 33 (e). After the *S-type* function transformation, the value histogram in the *iHSV* color space is so concentrated in the central region that the contrast is mildly reduced but the image is more saturated as shown in Fig. 32 (e). On the other hand, the value-histogram-centralized image in the *HSV* color space is still not satisfying.

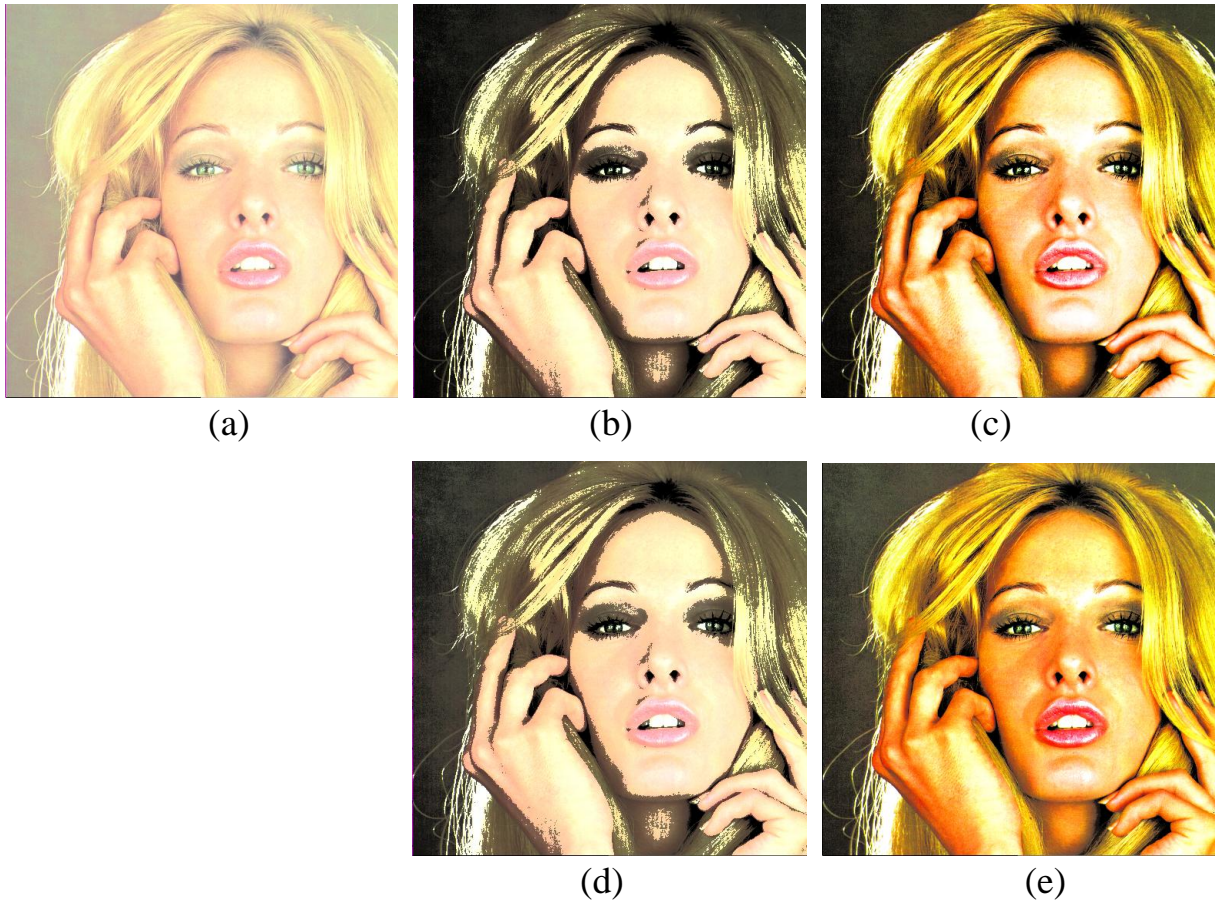


Fig. 30. The enhancement result of the Tiffany image. (a) The original image. (b) Contrast enhancement result with histogram equalization in the *HSV* color space. (c) Contrast enhancement result with histogram equalization in the *iHSV* color space. (d) Saturation enhancement in *HSV* color space with the *S-type* function. (e) Saturation enhancement in *iHSV* color space with the *S-type* function.

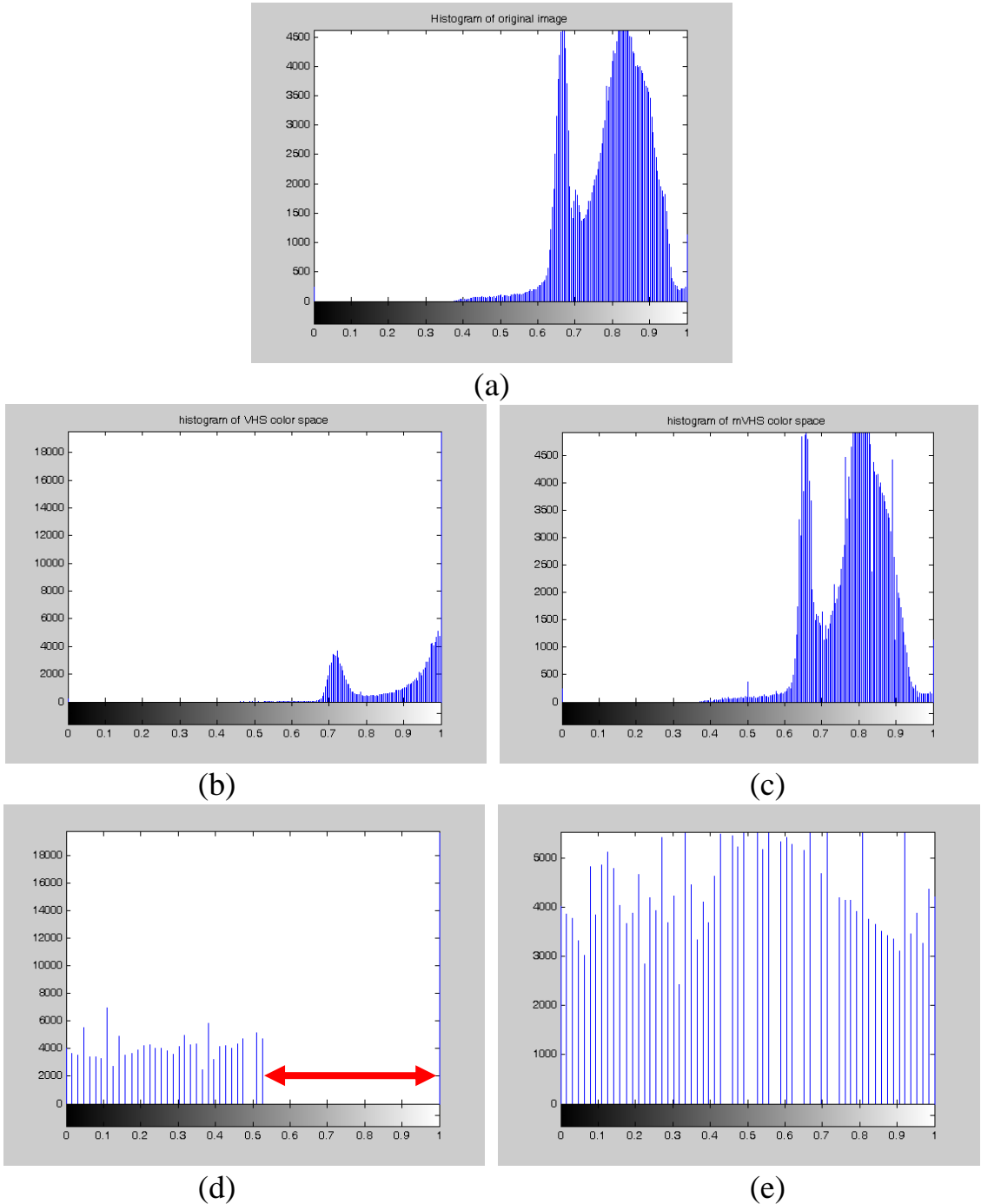


Fig. 31. The histogram variations of the Tiffany image in different color spaces.
 (a) The intensity histogram of original image. (b) The value histogram of original image in *HSV* color space. (c) The value histogram of original image in *iHSV* color space. (d) The value histogram equalized in *HSV* color space. (e) The value histogram equalized in *iHSV* color space.



(a)



(b)



(c)



(d)



(e)

Fig. 32. The enhancement result of the car image. (a) Original image. (b) The enhancement result by using histogram equalization in the *HSV* color space. (c) The enhancement result by using histogram equalization in the *iHSV* color space. (d) Saturation enhancement in *HSV* color space with the *S-type* function. (e) Saturation enhancement in *iHSV* color space with the *S-type* function.

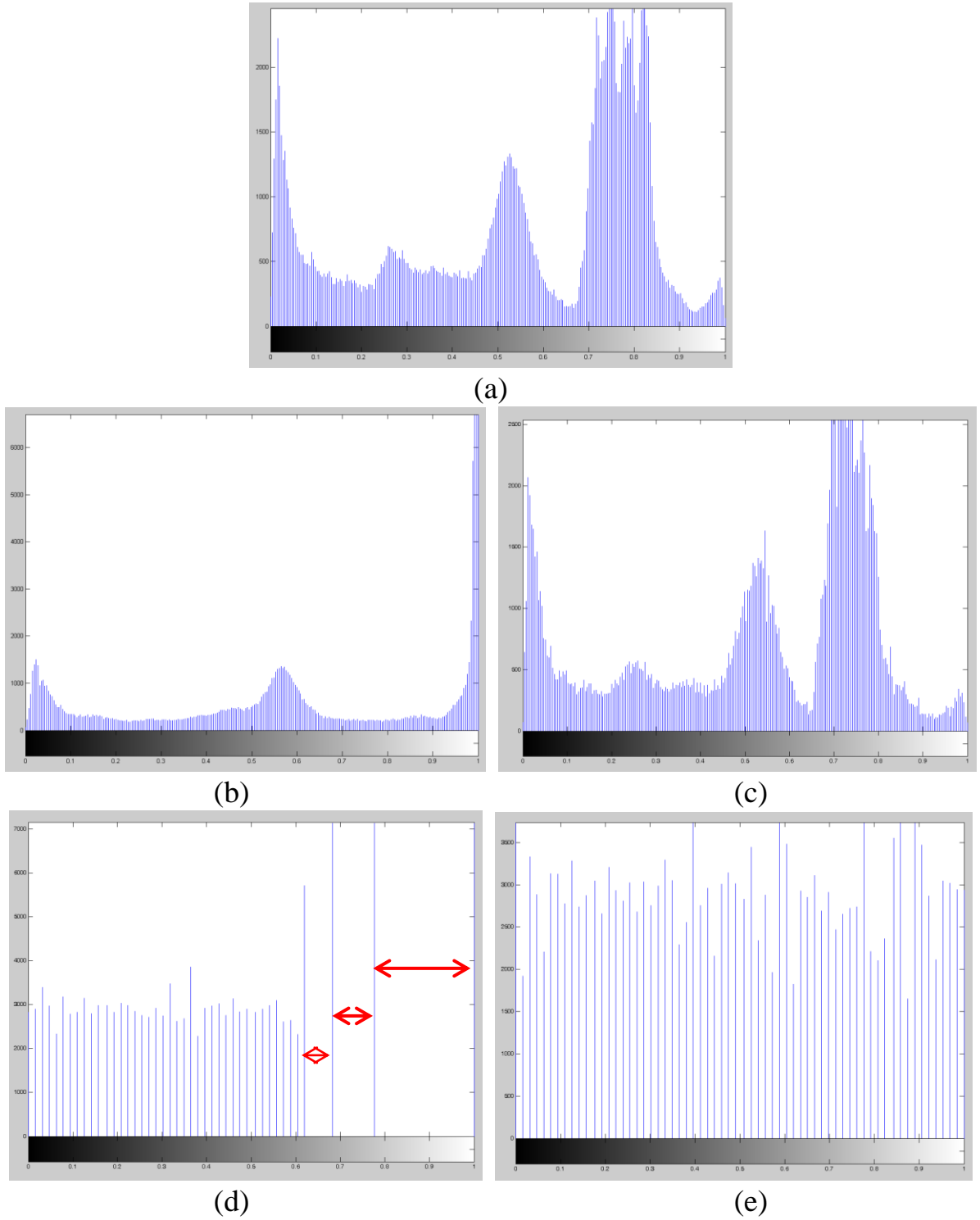


Fig. 33. The histogram variations of the car image in different color spaces. (a) The intensity histogram of original image. (b) The value histogram of original image in *HSV* color space. (c) The value histogram of original image in *iHSV* color space. (d) The value histogram of (b) processed by histogram equalization. (e) The value histogram of (c) processed by histogram equalization.

6.3 Cloud removal

We used 6.25 meter-resolution synthesized *SPOT* images to evaluate the proposed approach. The processed images show the same regions but were captured in different years. We assume that the land covers have only a little change in the period of image acquisition and the locations of clouds are not overlapped. Two *SPOT* images near the Tseng-Wen Reservoir captured in years 2001 and 2000 are shown in Fig. 17 (a) and (b), respectively. At first, both images were respectively enhanced by the proposed *eHSI*-based method, and we selected the 2001 image as the base image. Then, we used the intensity thresholding with comparison method to separate the cloud and non-cloud pixels. The cloud fraction images are shown in Fig. 23 (a); some bright pixels of land cover or buildings were mistaken as cloud pixels. Thirdly, we check the difference from the 2000 image (the replacing image) to eliminate unnecessary marking and use the morphology “opening” operation to exclude small bright areas such as the megalopolis shown in Fig. 23 (b). Fourthly, we partitioned the enhanced base image into 32×32 pixels zones, and the zones were determined as cloud zones if they had more than five cloud pixels. Subsequently, we used eight-neighbor grid zones around the thick cloud zones to include the thin cloud and cloud-shadow zones as shown in Fig. 24 (a). Finally, the cloud and augmented zones were replaced with the color-unified target source image as shown in Fig. 24 (b); the result being replaced with the non-unified target source image was also given for comparison as shown in Fig. 24 (c). The final fused result of the pyramid multi-scale fusion method is shown in Fig. 24 (d). Another case is shown in Fig. 34, in which the source images have more difference in brightness and contrast, but the case also shows a well fused result.

This study targets the applications of geographical visualization like Google Earth; thus all clouds to be removed are small scale. For most cases, two different-temporal images are enough to produce a satisfied cloud-free image.

However, if clouds appear in the same location of both source images, additional images are required for retrieving cloud-free pixels.

The results of cloud-free fusion on natural aerial images are hard to quantitatively evaluate because the multi-temporal images are variant in brightness and cloud cover. Here only cloud detection is quantitatively comparison. The procedure for cloud removal is generally detecting cloud pixels and then replacing the cloud pixels with non-cloud pixels; thus, we compare the performance of cloud detection for variant cloud detection methods. We manually label the cloud pixels on several cloud images to construct the ground truth for the comparison. There are totally 4,194,304 pixels in the processed images and 13,853 pixels are cloud pixels. Four mentioned cloud detection methods: gradient, *PWD*, *LSU*, and intensity thresholding were comparison as the results shown in [Table 1](#). The evaluation criteria included Type I error, Type II error, and detection rate. Type I error means missing the detection of cloud pixels; it is also called the “false positive”. Type II error means classifying the non-cloud pixels as cloud pixels and is also called “false negative”. Detection rate is the ratio of correctly-detected cloud pixels to all cloud pixels. The unit of Type I and II errors is number.

There are thin and fragmented cloud regions in the processed images. Gradient and *PWD* methods are hard to detect the thin cloud pixels; thus their detection rates are low. The bright pixels in megalopolis have the same characteristic as cloud pixels; thus many bright pixels were wrong taken as cloud pixels. The difference checking is used to release these bright pixels by checking the pixel differences in two images. Thus the Type II error of the methods with difference checking is obviously reduced. The cloud characteristic of cloud pixels on the cloud boundary is very unapparent; these cloud pixels are transformed to non-cloud pixels after difference checking; thus the detection rate is degraded. The Opening process for *LSU* has the similar function as the

difference checking. Though the detection rate of *LSU* is better than that of intensity thresholding, the latter has better Type II error than the former. More Type I errors may result in more incomplete cloud removal. On the other hand, more Type II errors may result in more unnecessary processes; moreover, it may not only be time consuming, but also generate over-mosaic images. The proposed “intensity thresholding + difference checking” approach has the least Type I + Type II errors.

Table 1. The comparison of cloud detection among the eight methods.

Methods	<i>Type I</i> error	<i>Type II</i> error	Detection rate
Gradient	7,539	514,329	45.58 %
Gradient + Difference checking	9,646	4,207	30.37 %
<i>PWD</i>	6,461	136,419	53.36 %
<i>PWD</i> + Difference checking	9,222	5,008	33.43 %
<i>LSU</i>	136	108,321	99.02 %
<i>LSU</i> + Opening	2,261	39,409	83.68 %
Intensity thresholding	354	61,294	97.44 %
Intensity thresholding + Difference checking	925	1,425	93.33 %

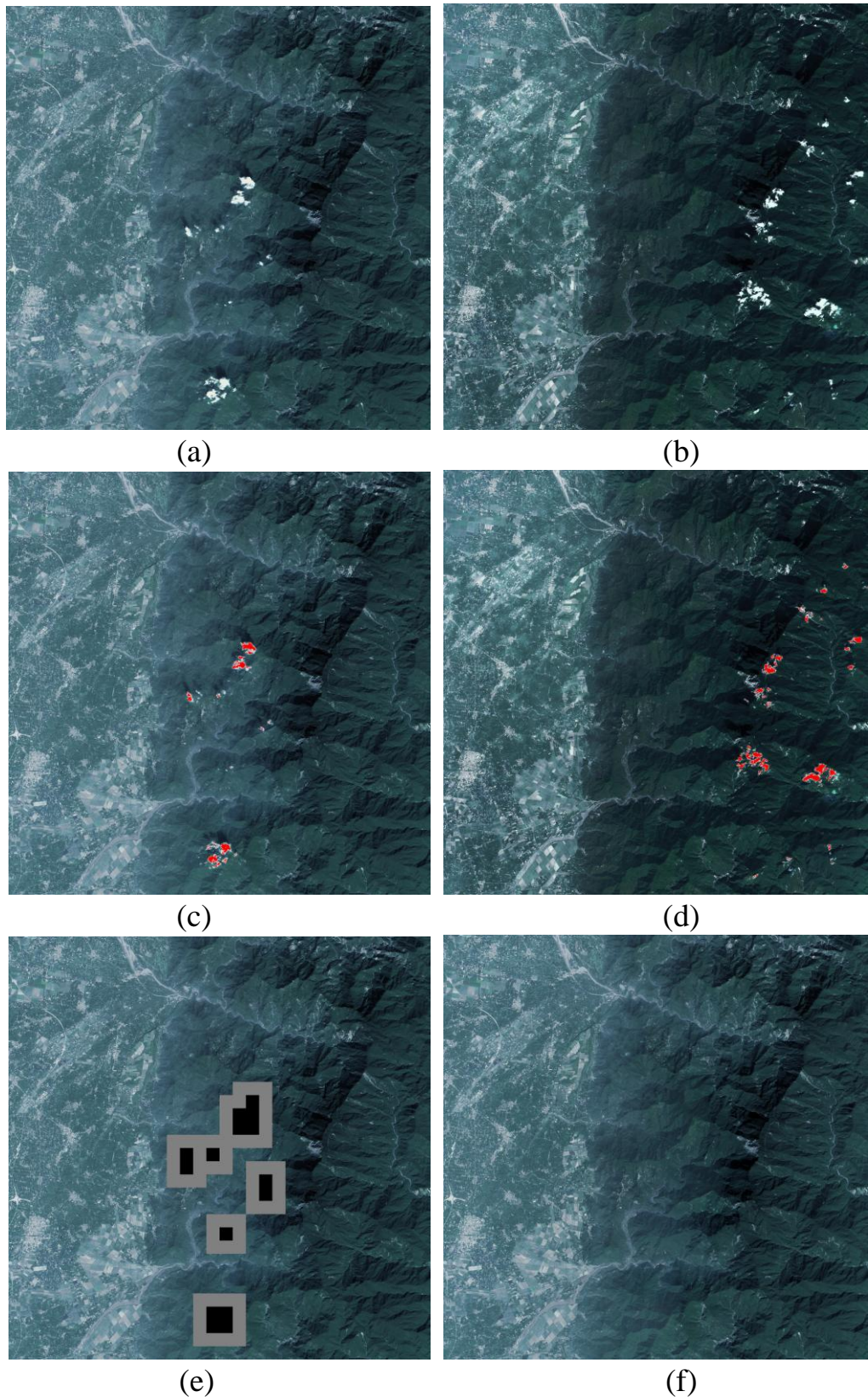


Fig. 34. Another example of cloud removal. (a) and (b) The original cloudy images. (c) and (d) The detected cloud areas by using the intensity thresholding and difference checking method. (e) The cloud detected zones and transition zones. (f) The final fusion result.

Chapter 7

Conclusions

In this paper, we proposed two improved color models for color image enhancement. Furthermore, a multidisciplinary method is used to synthesize high-quality cloud-free images from multi-temporal aerial images.

The main purpose of exact *HSI* color model is to improve the traditional *HSI* model for variant applications on color images, not to compare enhancement results. The proposed *eHSI* color model has several advantages over the traditional *HSI* color model.

First, the model has no out-of-gamut problem and the intensity component can be changed faithfully. As mentioned in the introduction chapter, Weeks *et al.* [45] suggested hue-preserving color image enhancement techniques that partition the whole (*C-Y*) color space into $N \times K$ subspaces, where N and K are the number of partitions in the luminance and saturation components, respectively. However, the decision of the subspace numbers N and K is crucial to the results. Duan and Qiu [17] stated that the more the regions were divided, the fewer cross-session artifacts there are, but more computational time is needed. Moreover, the calculation of lookup table is complicated. Here, the proposed *eHSI* model needs not consider the subspace division and create lookup tables. Of course, we can also divide the *eHSI* color space into subspaces and enhance each subspace separately without the out-of-gamut problem and lookup table calculation.

Second, the saturation component is automatically adjusted according to the attainable maximum saturation range. Hence, the saturation enhancement is simultaneously achieved with the intensity enhancement. Most color image enhancement procedures enhance intensity and saturation separately so that the correlation between intensity and saturation is destroyed and some abnormal

patches are appeared. For some color image enhancement algorithms in the traditional *HSI* model, the achromatic region must be specially treated to avoid the over-enhancement problem. Contrarily, in the *eHSI* space, the saturation is automatically adjusted according to its attainable maximum saturation range. With the suggested *S-type* transformation method, the intensity is mildly adjusted toward the intensity central region, and the attainable maximum saturation range is mildly expanded; hence, over-enhancement of saturation in the achromatic region rarely occurs.

Third, in the traditional *HSI* space, the saturation is always reduced if the intensity is decreased and the saturation is always increased if the intensity is increased. Furthermore, the intensity increasing is disrupted if the pixel is out of gamut. However, these problems are totally solved in the proposed *eHSI* space.

Naik and Murthy [18] proposed an effective method for handling the out-of-gamut problem during color processing. The processing is completely done in the *RGB* space; thus, there is no need to back the *RGB* values to their bounds after the processing. Moreover, the saturation and hue values of pixels need not be processed, but the hue is preserved. However, several enhancement algorithms developed in the *HSI* space cannot be used by this method. On the other hand, manipulating intensity and saturation in the *RGB* space requires far less intuition than that in the *HSI* space.

The computational burden of the proposed *eHSI* transformation is not much higher than that of the traditional *HSI* transformation because the extra load is just a few decision criteria. Though *HSI* and *eHSI* transformations have the similar computational complexity, they are still more complicated than *HSV* color model. *HSV* color model is more popular and simpler computation than *HSI* color model. We will analyze the *HSV* properties and evaluate whether it is more suitable for color image enhancement or not in the future.

The value histogram in the traditional *HSV* color space is concentrated in

the high value region due to more accumulation of value histogram at the high value and saturation level. If we equalize the value histogram in the *HSV* color space, most pixels' values will be decreased, finally a darker image will be produced and some speckles in the uniform region will appear. Furthermore, according to the characteristics of the *HSV* color space, the pixel's saturation is decreased simultaneously with the decreased value component no matter the attainable maximum saturation range of the target is wider or narrower than that of the source. Hence value histogram equalization is not suitable for the *HSV* color space, especially for bright and high saturated images.

On the other hand, the value histogram distribution in the proposed *iHSV* color space is similar to the Gaussian distribution of the intensity histogram in the *RGB* color space; that is, the attainable maximum saturation range is wider in the central value histogram region and narrower in the high and low value histogram regions. Moreover, the computational burden is similar to the transformation between the *RGB* and *HSV* color spaces.

Moreover, for most color image enhancement algorithms, the intensity enhancement and saturation enhancement are performed separately [45]. For the saturation enhancement, the achromatic region must be considered; that is, some pixels around the white-black axis are not colorful and enhancing these color pixels is meaningless. However, in the proposed *iHSV* color space, the intensity is adjusted from a source point to a target point; the saturation is automatically and linearly tuned according to the target attainable maximum saturation range and the correlation between the value and saturation components is preserved. Hence the saturation enhancement is automatically achieved and the saturation over-enhancement of achromatic pixels rarely occurs.

In conclusion, the proposed *iHSV* color space does not have the defects of the *HSV* color space and is more suitable for many color image processing applications.

For cloud removal application, the proposed approach has the following characteristics: (i) an *eHSI*-based enhancement method was proposed to enhance intensity and saturation components of the original images; (ii) intensity thresholding accompanied by difference checking was proposed for cloud determination; (iii) $l\alpha\beta$ color matching was used to unify the color of the base and replacing images; (iv) a contour band composed of augmented zones for the cloud zones was designed for image fusion; (v) a pyramid multi-scale fusion method was used to fuse images making seams invisible; and (vi) a complete system was proposed to generate cloud-free images. Few complete approaches were proposed for cloud removal. Here we placed much effort on the color processing and proposed a complete approach to synthesize the high-quality images with proper brightness and saturation; the results quite fit human visual perception and achieve practical applications.

The procedure steps of this study are the same as our previous work [36]; but, the methods of all three main steps: image enhancement, cloud detection, and image fusion, are different and improved in effect and efficiency. First, we enhance the color image in the *eHSI* color space; there is no out-of-gamut problem and the saturation and intensity enhancements are simultaneously completed. In the previous work, the out-of-gamut problem was solved by a complicated strategy; sometimes, the out-of-gamut problem could not be completely solved. Moreover, the saturation was enhanced by an additive process and the correlation between intensity and saturation is not solved. Second, we detect and segment cloud regions with the color thresholding method in the *eHSI* color space. The method is more efficient than the previous-used linear spectral unmixing (*LSU*) method; the *LSU* method is not suitable for the images that are composed of *RGB* bands because the number of bands is much less than the number of component materials.

References

- [1] W.-C. Kao, L.-Y. Chen, and S.-H. Wang, "Tone reproduction in color imaging systems by histogram equalization of macro edges," in *Proc. of IEEE Tenth International Symposium on Consumer Electronics*, St. Petersburg, Sep. 11, 2006, pp. 1-6.
- [2] W.-C. Kao, S.-H. Wang, L.-Y. Chen, and S.-Y. Lin, "Design considerations of color image processing pipeline for digital cameras," *IEEE Trans. on Consumer Electronics*, vol.52, no.4, pp.1144-1152, 2006.
- [3] T. Tateyama, Z. Nakao, X. Han, and Y.-W. Chen, "Contrast enhancement of mr brain images by canonical correlations based kernel independent component analysis," *Int. Journal of Innovative Computing, Information and Control*, vol.5, no.7, pp.1857-1866, 2009.
- [4] M. Hossain and M. Alsharif, "Minimum mean brightness error dynamic histogram equalization for brightness preserving image contrast enhancement," *Int. Journal of Innovative Computing, Information and Control*, Vol.5, no.10, pp.3249-3260, 2009.
- [5] J. Pan, C. Zhang, and Q. Guo, "Image enhancement based on the shearlet transform," *ICIC Express Letters*, vol.3, no.3 (B), pp.621-626, 2009.
- [6] Y. Zhang, C. Zhang, J. Chi, and R. Zhang, "An algorithm for enlarged image enhancement," *ICIC Express Letters*, vol.3, no.3 (B), pp.669-674, 2009.
- [7] R. N. Strickland, C. Kim, and W. F. McDonnell, "Digital color image enhancement based on the saturation component," *Optical Engineering*, vol.26, pp.609-616, 1987.
- [8] B. A. Thomas, R. N. Strickland, and J. J. Rodriguez, "Color image enhancement using spatially adaptive saturation feedback," in *Proc. of Int. Conf. on Image Processing*, Santa Barbara, CA, Oct. 26-29, 1997, vol.3, pp.30-33.
- [9] A. Toet, "Multiscale color image enhancement," in *Proc. of Int. Conf. on Image Processing and its Application*, Maastricht, Netherlands, Apr.7-9, 1992, pp.583-585.
- [10] I. Pitas and P. Kiniklis, "Multichannel techniques in color image enhancement and modeling," *IEEE Trans. on Image Processing*, vol.5, no.1, pp.168-171, 1996.

- [11] P. E. Trahanias and A. N. Venetsanopoulos, "Color image enhancement through 3-D histogram equalization," in *Proc. of 11th IAPR Int. Conf. on Pattern Recognition*, The Hague, Netherlands, Aug.30 - Sep.3, 1992, vol.3, pp. 545-548.
- [12] P. A. Mlsna and J. J. Rodriguez, "A multivariate contrast enhancement technique for multispectral images," *IEEE Trans. on Geoscience and Remote Sensing*, vol.33, no.1, pp.212-216, 1995.
- [13] P. A. Mlsna, Q. Zhang, and J. J. Rodriguez, "3-D histogram modification of color images," in *Proc. of Int. Conf. on Image Processing*, Lausanne, Switzerland, Sep.16-19, 1996, pp.1015-1018.
- [14] Q. Zhang, P. A. Mlsna, and J. J. Rodriguez, "A recursive technique for 3-D histogram enhancement of color images," in Proc. of the *IEEE Southwest Symp. on Image Analysis and Interpretation*, San Antonio, TX, Apr.8-9,1996, pp. 218-223.
- [15] I. M. Bockstein, "Color equalization method and its application to color image processing," *J. Opt. Soc. Am. A*, vol.3, no.5, pp.735-737, 1986.
- [16] A. R. Weeks, G. E. Hague, and H. R. Myler, "Histogram equalization of 24-bit color images in the color difference (C-Y) color space," *Journal of Electronic Imaging*, vol.4, no.1, pp.15-22, 1995.
- [17] J. Duan and G. Qiu, "Novel histogram processing for colour image enhancement," in *Proc. of The Third Int. Conf. on Image and Graphics*, Hong Kong, Dec.18-20, 2004, pp.55-58.
- [18] S. K. Naik and C. A. Murthy, "Hue-preserving color image enhancement without gamut problem," *IEEE Trans. on Image Processing*, vol.12, no.12, pp.1591-1598, 2003.
- [19] M.-S. Shyu and J.-J. Leou, "A genetic algorithm approach to color image enhancement," *Pattern Recognition*, vol.31, no.7, pp.871-880, 1998.
- [20] C. C. Yang and J. J. Rodriguez, "Efficient luminance and saturation processing techniques for bypassing color coordinate transformations," in *Proc. of IEEE Int. Conf. on Systems, Man and Cybernetics*, Vancouver, BC, Canada, Oct.22-25, 1995, pp.667-672.
- [21] C. C. Yang and J. J. Rodriguez, "Saturation clipping in the LHS and YIQ color spaces," in *Proc. of Conf. on Color Imaging: Device-Independent Color, Color Hard Copy, and Graphic Arts*, San Jose, CA, Jan.29, 1996, pp.297-307.

- [22] J. J. Rodriguez and C. C. Yang, "High-resolution histogram modification of color images," *Graphical Models and Image Processing*, vol.57, no.5, pp.432-440, 1995.
- [23] R. C. Gonzalez and R. E. Woods, *Digital Image Processing*, 3rd edition, Prentice Hall, Upper Saddle River, NJ, 2007.
- [24] G. J. Chamberlin, *The CIE International Color System Explained*, 2nd edition, The Tintometer Ltd., Salisbury, England, 1951.
- [25] F. Chun, M. Jian-wen, D. Qin, and C. Xue, "An improved method for cloud removal in ASTER data change detection," in *Proc. Int. Geoscience and Remote Sensing Symp.*, Anchorage, Alaska, Sep.20-24, 2004, pp.3387-3389.
- [26] U. Amato, A. Antoniadis, V. Cuomo, L. Cutillo, M. Franzese, L. Murino, and C. Serio, "Statistical cloud detection from SEVIRI multispectral images," *Remote Sensing of Environment*, vol.112, no.3, pp.750-766, 2008.
- [27] Y. S. Choi, C. H. Ho, M. H. Ahn, and Y. M. Kim, "An exploratory study of cloud remote sensing capabilities of the Communication, Ocean and Meteorological Satellite (COMS) imagery," *Int. Journal of Remote Sensing*, vol.28, pp.4715-4732, 2007.
- [28] Z. Wang, J. Jin, J. Liang, K. Yan, and Q. Peng, "A new cloud removal algorithm for multi-spectral images," in *Proc. SAR and Multispectral Image Processing*, Wuhan, China, Oct.31 - Nov.2, 2005, pp.60430W-11.
- [29] P. Arellano, *Missing Information in Remote Sensing: Wavelet Approach to Detect and Remove Clouds and Their Shadows*, Master Thesis, Int. Institute of Geo-information Science and Earth Observation, Enschede, The Netherlands, 2003.
- [30] S. Gabarda and G. Cristóbal, "Cloud covering denoising through image fusion," *Image and Vision Computing*, vol.25, no.5, pp.523-530, 2007.
- [31] E. H. Helmer and B. Ruefenacht, "Cloud-free satellite image mosaics with regression trees and histogram matching," *Photogrammetric Engineering and Remote Sensing*, vol.71, no.9, pp.1079, 2005.
- [32] M. Li, S. C. Liew, and L. K. Kwok, "Generating "cloud free" and "cloud-shadow free" mosaic for SPOT panchromatic images." in *Proc. IEEE Int. Geoscience and Remote Sensing Symp.*, Toronto, Canada, Jun.24-28, 2002, vol.4, pp.2480-2482.

- [33] M. Li, S. C. Liew, and L. K. Kwoh, "Producing cloud free and cloud-shadow free mosaic from cloudy IKONOS images," in *Proc. IEEE Int. Geoscience and Remote Sensing Symp.*, Toulouse, France, Jul.21-25, 2003, vol.6, pp. 3946-3948.
- [34] S. C. Liew, M. Li, L. K. Kwoh, P. Chen, and H. Lim, ""Cloud-free" multi-scene mosaics of SPOT images." in *Proc. IEEE Int. Geoscience and Remote Sensing Symp.*, Seattle, WA, Jul.6-10, 1998, vol. 2, pp. 1083-1085.
- [35] B. Wang, A. Ono, K. Muramatsu, and N. Fujiwara, "Automated detection and removal of clouds and their shadows from Landsat TM images," *IEICE Tran. on information and systems*, vol.82, no.2, pp.453-460, 1999.
- [36] D.-C. Tseng, H.-T. Tseng, and C.-L. Chien, "Automatic cloud removal from multi-temporal SPOT images," *Applied Mathematics and Computation*, vol.205, no.2, pp.584-600, 2008.
- [37] P. Burt and E. Adelson, "The Laplacian pyramid as a compact image code," *IEEE Trans. on Communications*, vol.31, no.4, pp.532-540, 1983.
- [38] M. Kubo, H. Koshinaka, and K. I. Muramoto, "Extraction of clouds from satellite imagery in the Antarctic using wavelet transform and Mahalanobis classifier." in *Proc. IEEE Int. Geoscience and Remote Sensing Symp.*, Sydney, Australia, Jul.9-13, 2001, vol.5, pp.2158-2160.
- [39] Z. Li, Z. Jing, X. Yang, and S. Sun, "Color transfer based remote sensing image fusion using non-separable wavelet frame transform," *Pattern Recognition Letters*, vol.26, no.13, pp.2006-2014, 2005.
- [40] J. Foley, *Computer Graphics: Principles and Practice*, Massachusetts Addison-Wesley, 1995.
- [41] Y. H. Hu, H. B. Lee, and F. L. Scarpace, "Optimal linear spectral unmixing," *IEEE Trans. on Geoscience and Remote Sensing*, vol.37, no.1, pp.639-644, 1999.
- [42] C. L. Chien and D.-C. Tseng, "Color image enhancement with the exact IHS (*eIHS*) color transformation," *Int. Journal of Innovative Computing, Information and Control*, 2011. (to appear)
- [43] E. Reinhard, M. Adhikhmin, B. Gooch, P. Shirley, "Color transfer between images," *IEEE Computer Graphics and Applications*, vol.21, no.5, pp.34-41, 2001.
- [44] D. L. Ruderman, T. W. Cronin, and C.-C. Chiao, "Statistics of cone

responses to natural images: implications for visual coding," *J. Opt. Soc. Am. A*, vol.15, no.8, pp.2036-2045, 1998.

- [45] A. R. Weeks, L. J. Sartor, and H. R. Myler, "Histogram specification of 24-bit color images in the color difference (C-Y) color space," *Journal of Electronic Imaging*, vol.8, no.3, pp.290-300, 1999.